RESEARCH SCHOOL O F CHEMISTRY

SYNTHESIS, STRUCTURAL CHARACTERISATION AND DIELECTRIC PROPERTIES OF SOME EARLY d° TRANSITION METAL OXIDE CERAMICS

A thesis submitted for the degree of Doctor of Philosophy at
The Australian National University
by

BINH HAI NGUYEN

December 2009


THE AUSTRALIAN
LIBRARY
NATIONAL UNIVERSITY

This thesis, except where specified otherwise in the text, is original work that has been carried out by the candidate.

Nguyen Hai Binh

ACKNOWLEGEMENTS

I would like to gratefully and sincerely thank the following people. You have made my time at ANU a wonderful and rewarding experience.

First and foremost, I must thank Professor Ray Withers for being such a wonderful supervisor, for all his encouragement, guidance, support, understanding, patience, supervision and for giving me the opportunity to obtain a Ph.D. I could not ask for a better supervisor to guide my graduate research.

I would also like to thank my supervisor Dr. Yun Liu for her assistance, guidance and much helpful advice in getting my PhD project correctly on track.

I also wish to thank Dr. Lasse Noren, for his comments and discussion on my thesis, to Professor Richard Welberry for his help during my research and Dr. John Barry for kindly providing HRTEM images.

I am also very grateful to Dr. Frank Brink and his staff at CAM, ANU for assisting me with microscopy related experiments.

Finally, I would like to thank my parents, my sister, Trang and my friends for your support and encouragement.

ABSTRACT

The aim of this thesis is to investigate the relationship between synthesis conditions, structure and dielectric properties of four inherently disordered, Bi-based, pyrochlore dielectric ceramic systems, an analogous non-Bi based pyrochlore ceramic and a perovskite related ceramic system.

Two 'misplaced displacive', Bi-based cubic pyrochlore phases found in the Bi_2O_3-$M^{II}O$-Nb_2O_5 (M = Mg^{2+} and Ni^{2+}) systems, namely $(Bi_{1.667}Mg_{0.22}\square_{0.11})(Mg_{0.48}Nb_{1.52})O_7$ (BMN) and $(Bi_{1.667}Ni_{0.25}\square_{0.08})(Ni_{0.50}Nb_{1.5})O_7$ (BNN), cubic pyrochlores have been synthesised and their average structures and promising dielectric properties determined. The O'A_2 tetrahedral sub-structures of both pyrochlores are heavily disordered with metal ion vacancies on the pyrochlore A site. A highly structured diffuse intensity distribution apparent in electron diffraction data is shown to arise from essentially independent β-cristobalite-like tetrahedral edge rotation and associated translation of the positively charged O'A_2 tetrahedral sub-structure relative to the B_2O_6 octahedral sub-structure thus giving rise to local 1-d polar nano-regions (PNRs). Both BMN and BNN exhibit characteristic low temperature dielectric relaxation behaviour.

In addition, two A site stoichiometric, Bi_2InNbO_7 (BIN) and Bi_2ScNbO_7 (BSN), cubic pyrochlores have also been synthesised. The β-cristobalite like displacive disorder and low temperature dielectric relaxation behaviour characteristic of BMN and BNN is also shown to be characteristic of BIN and BSN despite the absence of compositional disorder on the pyrochlore A site. The low temperature, frequency-dependent peak in the dielectric loss of BIN and BSN is shown not to be a conventional phase transition but rather a dynamic freezing or glass-like transition involving the slowing down of the 1-d dipolar dynamics of the PNR's.

An analogous non-Bi based, 'misplaced-displacive' $(Ca_{0.75}Ti_{0.25})_2(Ti_{0.50}Nb_{0.50})_2O_7$ (CNT) cubic pyrochlore has also been synthesised and its dielectric properties measured. It is thereby established that the characteristic low

temperature dielectric relaxation behaviour observed in Bi-based pyrochlores does not require the presence of Bi^{3+} on the pyrochlore *A* site.

Finally, a $Ca_{1-x}Sm_{2x/3}TiO_3$ (CST, $0 \leq x \leq \sim 0.6$) ceramic system has also been investigated. The measured dielectric properties were found to vary significantly with Sm content. CST samples sintered at 1450 °C for 3 hours in air and oxygen were all single phase and quite similar to those reported for the end-member compound, $CaTiO_3$. Powder XRD as well as electron diffraction patterns of the CST samples were entirely consistent with a *Pnma*, $\sqrt{2}a_p$ x $2a_p$ x $\sqrt{2}a_p$ (subscript p for parent perovskite sub-structure) average crystal structure. Electron diffraction and HRTEM image analysis suggests short range Ca and Sm ordering, on a scale considerably shorter than the scale associated with the essentially long range ordered *Pnma* average structure.

TABLE OF CONTENTS

LIST OF ABBREVIATIONS

ADP	Atomic Displacement Parameter
ANU	Australian National University
AV	Apparent Valence or Bond Valence Sum.
BBCPs	Bi-based Cubic Pyrochlores
BFN	Bi_2FeNbO_7
BIN	Bi_2InNbO_7
BMN	$Bi_{1.67}Mg_{0.75}Nb_{1.5}O_7$
BMT	$BaMg_{1/3}Ta_{1/3}O_3$
BNN	$Bi_{1.67}Ni_{0.75}Nb_{1.5}O_7$
BSE	Back Scattered Electrons
BZN	$Bi_{1.5}ZnNb_{1.5}O_7$
BZT	$BaZn_{1/3}Ta_{2/3}O_3$
CNT	$Ca_{1.5}Ti_{1.5}NbO_7$
CST	$Ca_{1-x}Sm_{2x/3}TiO_3$
DFT	Density Functional Theory
EDP	Electron diffraction pattern
EDS	Energy Dispersive X-Ray Spectroscopy (or EDX)
EMU	Electron Microscopy Unit (ANU)
EPMA	Electron Probe Micro Analysis
GPS	Global Positioning System
HIFAR	High Flux Australian Reactor
HRPD	High Resolution Powder Diffractometer
LAN	Local Area Network
LTCC	Low Temperature Co-fired Ceramic
MOD	Metalorganic Decomposition
RSC	Research School of Chemistry
PNR	Polar nano region
RUM	Rigid Unit Mode
SE	Secondary Electron
SEM	Scanning Electron Microscope
TEM	Transmission Electron Microscopy

Wt %	Weight percent
Vol %	Volume percent
XRD	X-ray Diffraction
XRPD	X-ray powder Diffraction
ZAF	Atomic number (Z), Absorption (A) and Fluorescence (F) correction procedure.

GLOSSARY OF TERMS

Calcination	Heating at an elevated temperature for an extended period. Used *e.g.* to thermally decompose hydrates and carbonates to oxides or to carry out chemical reactions.
Ceramic filter	A type of mechanical filter that uses a series of resonant ceramic disks to obtain a band-pass response.
Ceramic resonator	A dielectric resonator made of a ceramic material.
Dielectric loss	The proportion of energy that is dissipated within a dielectric material and lost as heat in an electrostatic field.
Dielectric loss factor	The product of the dielectric constant and the tangent of the dielectric loss angle. Also known as the dielectric loss index.
Topography	The surface features of an object or "how it looks", its texture.
Q factor (quality factor)	The quality factor, Q, of a dielectric material is the ratio of the energy stored in the dielectric resonator and in the shield to the losses in the resonator and the surrounding metallic walls.

LIST OF SYMBOLS

a, b, c	Real space lattice vectors
a*, b*, c*	Reciprocal space lattice vectors
a, b, c	unit cell dimensions
(h, k, l)	a specific lattice plane in real space
{h, k, l}	the family of symmetry equivalent (h, k, l) planes
*[h, k, l]**	a specific reflection in reciprocal space (≡ h**a*** + k**b*** + l**c***)
*<h, k, l>**	the family of symmetry equivalent [h, k, l]* reflections
$[h, k, l]_p$*	a specific reflection indexed with respect to the underlying parent perovskite sub-structure.
C	capacitance
E_a	activation energy
f_r	measuring frequency
f_o	the relaxation frequency at infinite temperature
G_p*	a parent perovskite Bragg reflection
k	the Boltzmann constant
σ_a	neutron absorption cross section
β	isotropic thermal parameter (= $8\pi^2\langle u^2\rangle$)
ε_0	vacuum permittivity
Δ	octahedral distortion
□	vacancy
ρ	density
Q	quality factor
T_{vf}	the non-zero freezing temperature of the relaxation
τ_ε	temperature coefficient of capacitance
τ_f	temperature coefficient of resonant frequency
χ_e	electric susceptibility

INDEX OF FIGURES

INDEX OF TABLES

Chapter 1: Introduction

This thesis describes the work performed in the search for a deeper understanding of the relationship between dielectric properties and structure (both average as well as local) of some dielectric ceramic material systems from both the fundamental materials chemistry, as well as materials engineering, points of view.

This introductory chapter explains the motives underlying the project and why the chosen materials for investigation are of interest. Relevant background information on the pyrochlore and $CaTiO_3$-based dielectric ceramic systems investigated is also presented.

1.1 Project Background

Increasingly, complex multi-functional applications such as global positioning systems (GPS's), wireless local area networks (LAN's) *etc.* need to be embedded into small mobile devices, requiring circuit boards with ever more component parts. To meet these commercial requirements, it is increasingly necessary to miniaturise these component parts so as to maintain or even decrease overall size and reduce the cost of such electronic devices [1-4]. To achieve miniaturisation, ceramic resonators and filters with high dielectric constants and low dielectric losses are typically embedded into printed circuit boards made mainly with low-cost epoxy resin. The global market for these types of ceramic materials was US $8.3 billion in 2008 [5] and is projected to continue to increase dramatically to reach $11.4 billion by 2015 [6].

The applications and usefulness of dielectric ceramics as resonators and filters for wireless communications comes from their relatively high permittivities (enabling miniaturisation), low dielectric losses *i.e.* high quality factors Q (enabling sharper signals, narrower bandwidths and lower insertion losses) and low temperature coefficients of resonant frequency (thereby minimising temperature-dependent frequency drift) [1-4]. The simultaneous optimisation of all three desirable parameters is quite a challenge. Indeed, some authors have declared that the three desirable properties described above are, in general, mutually exclusive [7]. Those materials with high dielectric permittivity, for example, often also have high temperature coefficients of resonant frequency (*e.g.* rutile, TiO_2) [2] such that a high permittivity and a zero τ_f are very rarely found together. Similarly, the dielectric loss of ceramic materials often increases dramatically as the permittivity increases, such that ceramic materials do not usually have both a high quality factor and a high permittivity [2]. Ferroelectric materials are an example with their typically very high dielectric constants but also high dielectric losses [3].

The dielectric ceramics that have to date been found to meet the above three requirements sufficiently well to be used commercially consist almost entirely of either octahedrally co-ordinated early d^0 transition metal ions such as Ti^{4+}, Ta^{5+}, Nb^{5+}, W^{6+} *etc.* and/or lone pair containing cations such as Pb^{2+}, Bi^{3+} *etc.* that are

susceptible to moving off-centre either statically or dynamically in a co-operative fashion and hence capable of giving rise to high permittivity. The materials currently dominating the commercial market for mobile phone base station dielectric ceramic resonators, for example, are the perovskite-related $BaZn_{1/3}Ta_{2/3}O_3$ (BaZT) and $BaMg_{1/3}Ta_{1/3}O_3$ (BaMT) compounds as a result of their outstanding dielectric properties (the highest known value of Q *i.e.* ~35,000 at 10 GHz, a low temperature coefficient of resonant frequency (τ_f ~5 ppm/°C) and a relatively large dielectric permittivity of ~25 [8]. The recent high demand for Ta, however, has led to a relative lack of availability and increasing expense (its cost has increased more than 10-fold over recent years [9]). In turn, this has sparked a search for possible replacement dielectric ceramic materials [9,10]. Analogous Nb-containing ceramic materials are a particular focus for such investigations. Likewise, the fact that Pb-containing electroceramic materials, are increasingly falling out of favour as a result of environmental concerns has led to a resurgence of interest in Bi-based dielectric ceramic materials.

An additional major disadvantage of BaZT and BaMT is the high sintering temperatures (> 1350 °C) required to produce suitably dense ceramic material. High densities are required because the dielectric permittivity of air is only 1. Too much porosity therefore severely degrades measured dielectric properties. Such high sintering temperatures (> 1350 °C) rule out the integration of these materials into monolithic microwave integrated circuits [1-3]. For passive integration into multilayer devices, dielectric materials are needed that can be co-fired under reducing conditions with internal Ag, Cu or other metal alloy electrodes (*i.e.* at temperatures < ~ 950°C) [2]. As a result of this latter requirement, many workers have focussed attention on the search for low-temperature, co-fired ceramic (LTCC) dielectric materials [11-14].

There are to date only a limited range of ceramic materials with sufficiently good dielectric properties that can be sintered at the latter relatively low temperatures including zinc titanate-based systems [12] but, in particular, Bi-containing dielectric ceramics such as $BiNbO_4$ as well as a range of chemically and displacively disordered cubic pyrochlore, or pyrochlore-related, phases within ternary systems such as the Bi_2O_3-NiO-Nb_2O_5 and Bi_2O_3-ZnO-Nb_2O_5 systems [13,14]. The relatively

low melting point of Bi_2O_3 (~ 825 °C) typically ensures the required relatively low sintering temperatures. In addition, the Bi^{3+} ion is often susceptible to moving off-center in a co-operative fashion and hence capable of giving rise to high permittivity.

By far the most attention to date has focussed on an ~ $Bi_{1.5}ZnNb_{1.5}O_{7-\delta}$ (BZN) cubic pyrochlore phase and a related monoclinic zirconolite phase of composition $Bi_2Zn_{2/3}Nb_{4/3}O_7$ found in the Bi_2O_3-$Zn^{II}O$-Nb_2O_5 ternary oxide system [15-20]. Both exhibit relatively high dielectric constants and low dielectric losses. The former has a large negative temperature coefficient of capacitance while the latter has a large positive coefficient. By forming appropriate mixtures of these phases it was found that the temperature coefficient of capacitance could thereby be tuned close to zero. The dielectric properties of these materials suggest that insulating Bi-based pyrochlore phases have considerable potential for applications and warrant careful investigation. There are a range of Bi-based pyrochlore systems of this type available [21,22] and the structural and dielectric properties investigation of some of these form an important component of this thesis.

In summary: the next generation of dielectric ceramic materials for device applications need significant improvements in their environmental friendliness (*e.g.* they need to be Pb-free), in the availability and hence cost effectiveness of the raw materials required for their synthesis (*e.g.* they need to contain *d*-transition metal ions other than Ta) and in their sintering temperatures. They should also maintain as high a performance as possible (*i.e.* a relatively high dielectric constant, as low a dielectric loss as possible as well as a close to zero temperature coefficient of capacitance) over as wide a range of environmental conditions as possible. It would also be desirable if their dielectric constants could be electric and/or magnetic field tuneable while maintaining good dielectric performance. In order to begin to approach these goals, there is a need to understand much more fully both the average structures as well as the inherent chemical and displacive disorder of many of these materials and how this structure relates to function in the form of their dielectric behaviour.

The overall aim of the research presented in this thesis is thus to synthesise, structurally characterise and investigate the relationship between chemical bonding, local crystal structure, longer range microstructure and dielectric properties (permittivity, dielectric loss, temperature coefficient of resonant frequency, electric field tunability *etc.*) in several important dielectric ceramic systems, in particular in several complex Bi-containing pyrochlore systems, one non-Bi-containing pyrochlore system and one perovskite related electroceramic system.

1.2 $A_2B_2O_7$ Oxide Pyrochlores

Oxide pyrochlores are a large and widely studied family of phases with ideal stoichiometry $A_2B_2O_7$ (A and B are cations) isostructural to the mineral pyrochlore, (Na,Ca)(Nb,Ta)O_6F/(OH) ([23,24]). The $A_2B_2O_7$, or B_2O_6•O'A_2, cubic $Fd\bar{3}m$ [25] ideal pyrochlore structure type can be described as being built out of two relatively weakly interacting, intergrown sub-structures, a B_2O_6 octahedral sub-structure (see Figure 1-1b) and an O'A_2 tetrahedral sub-structure built out of corner-connected, oxygen-centred tetrahedra, of ideal anti-β-cristobalite structure type (see Figure 1-1a). The intergrowth of these two component sub-structure types gives rise to the ideal pyrochlore structure type shown in Figure 1-2.

There are four crystallographically independent atom types per unit cell: the A, B, O and O' atom types located at the 16*d* or $^1/_2,^1/_2,^1/_2$; 16*c* or 000; 48*f* or x, $^1/_8,^1/_8$ and 8*b* or $^3/_8,^3/_8,^3/_8$ Wyckoff sites of $Fd\bar{3}m$, space group number 227 (origin choice 2) in the *International Tables for Crystallography, Vol. A* [25], respectively. The one unknown oxygen atom fractional co-ordinate, x, determines the extent to which the eight- and six-fold co-ordination polyhedra surrounding the A and B cations are distorted from ideal octahedral and cubic co-ordination respectively. For a regular octahedral oxygen environment around the B cations, x should be $^5/_{16}$ or 0.3125. For a regular cubic oxygen environment around the A ion, x should be $^3/_8$ or 0.375. In practice, x tends to take a lower value and to range from 0.31 to 0.34 depending on the particular oxide pyrochlore involved [23]. Lower x values distort the A cation co-ordination polyhedra away from cubic towards a scalenohedral or puckered hexagonal bipyramidal co-ordination with two rather short A-O' bonds and six rather longer A-O bonds (the A ions of the O'A_2 tetrahedral sub-structure are ideally situated

at the centres of puckered hexagonal rings of O ions in the B_2O_6 octahedral sub-structure). The latter rather longer *A*-O bonds represent the distance of closest approach between the two sub-structure network types. Although this distance of closest approach is usually significantly longer than any intra-network bond distance, the distance is still sufficiently short that the two sub-structures of Figure 1-2 can not be thought of as being truly independent.

As a family, oxide pyrochlores exhibit a wide variety of useful physical properties including dielectric, piezoelectric and ferroelectric behaviour, magnetic behaviour ranging from simple paramagnetism to ferro- or anti-ferromagnetism, fluoresescent and phosphorescent behaviour as well as solid electrolyte behaviour [23]. Their electrical properties range from insulating through semi-conducting to metallic behaviour dependent upon the relevant sizes and valence states of the *A* and *B* ions.

The most common oxide pyrochlores are the so-called (2+, 5+), $A^{II}{}_2B^{V}{}_2O_7$, and (3+, 4+), $A^{III}{}_2B^{IV}{}_2O_7$, oxide pyrochlores (see *e.g.* [23]). Bi-based pyrochlores of the latter type include $Bi^{III}{}_2B^{IV}{}_2O_7$ (*B* = Ti, Sn, Ru, Rh, Ir, Os and Pt) [26,27]. Oxide pyrochlores as a class also lend themselves to chemical substitution at the *A*, *B*, O and O' sites provided appropriate charge balance and other local crystal chemical and ionic size constraints are taken into account [23]. Golovshchikova *et al.* [22] in 1973, for example, first reported the existence of $Bi_2M^{III}Nb^{V}O_7$ (*M* = Fe and Sc) and $Bi_2M^{II}{}_{2/3}Nb^{V}{}_{4/3}O_7$ (*M* = Ni and Mg) oxide pyrochlores with rather good dielectric properties and intriguing low temperature dielectric relaxor behaviour. Subsequently Cann *et al.* [21] extended the number of pyrochlores of this type known and confirmed their intriguing temperature-dependent dielectric behaviour.

Note that much recent careful phase analysis work (particularly that of the NIST group [17,20,28] as well as some reported in this thesis) has shown that the true cubic pyrochlore phase in many such systems is often a solid solution, significantly Bi-deficient with respect to the above traditional stoichiometries and often requires the presence of nominally too small M^{2+} or M^{3+} cations on the *A* as well as the *B* sites of the ideal $A_2B_2O_7$ pyrochlore structure type (see e.g. [4,7,12-16]). They have thus recently been christened 'misplaced-displacive' cubic pyrochlores [28].

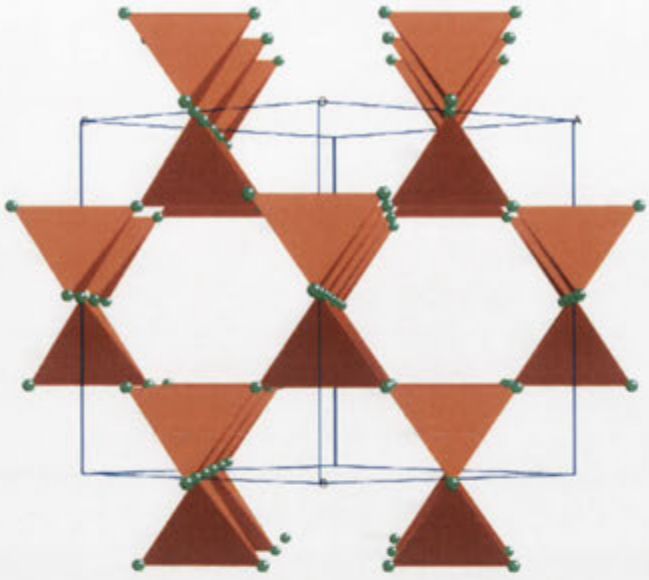

(a)

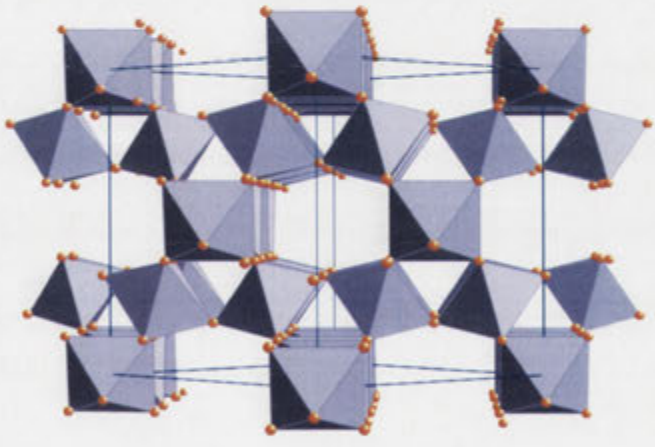

(b)

Figure 1-1 The two component sub-structures of the ideal pyrochlore $A_2B_2O_7$, or B_2O_6•O'A_2, structure type (a) the O'A_2 tetrahedral sub-structure and (b) the B_2O_6 octahedral substructure in projection close to a <110> direction. The constituent O'A_4 tetrahedra are shown in brown in (a) while the BO_6 octahedra are shown in blue in (b). The oxygen ions are represented by the small red balls in (b). The unit cell is outlined in both (a) and (b).

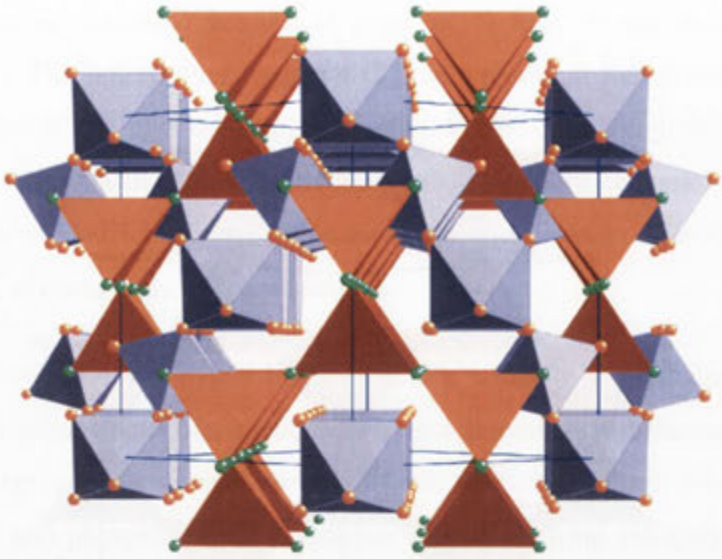

Figure 1-2 The ideal pyrochlore $A_2B_2O_7$, or $B_2O_6{\cdot}O'A_2$, structure type made up of its two constituent sub-structures.

Finally, 'defect' pyrochlores are also known where vacancies on the O' and *A* sites, in particular, readily occur.

1.2.1 Bi-based Oxide Pyrochlores

While apparently stoichiometrically simple (3+, 4+), Bi-based pyrochlores such as $Bi^{III}{}_2B^{IV}{}_2O_7$ (*B* = Ti, Sn, Ru, Rh, Ir, Os and Pt) [26] have been reported, all except the *B* = Ti and Sn pyrochlores are metallic and thus not of interest from the dielectric properties point of view [26,27]. The *B* = Sn pyrochlore is also polymorphic [29] which is again not ideal from the dielectric properties point of view. The focus of this thesis is therefore on the structural and dielectric properties characterisation of some insulating, inherently compositionally and/or displacively disordered 'misplaced-displacive' cubic pyrochlores of nominal stoichiometries $Bi_2M^{III}NbO_7$ (*M* = In and Sc) and $Bi_2M^{II}{}_{2/3}Nb_{4/3}O_7$ (*M* = Ni and Mg).

A non-Bi based, 'misplaced-displacive' cubic pyrochlore (of nominal stoichiometry $Ca_{1.5}NbTi_{1.5}O_7$) analogous to these Bi-based oxide pyrochlores has also been synthesised and its structural and dielectric properties systematically investigated for comparison purposes.

1.3 A $CaTiO_3$-based Dielectric Ceramic System

Current microwave (MW) electroceramics are typically divided into two classes differentiated by a figure of merit defined by the product of their quality factors, Q, with the applied frequency f (*i.e.* $Q \cdot f$) in accordance with the requirements of particular MW applications: (I) higher $Q \cdot f$ value (> 30,000 GHz) MW electroceramics with intermediate dielectric constants $\varepsilon_r \sim 25$~50 and (II) lower $Q \cdot f$ value (~10,000 GHz) MW electroceramics with higher dielectric constants in the range of 75 ~ 100. Class I MW electroceramics have already been commercialised [2]. Commercial products utilizing class II MW electroceramics, however, are yet to emerge [3].

Potential materials systems within which to search for class II dielectric ceramics are titanate perovskite systems based on $BaTiO_3$, $SrTiO_3$ and $CaTiO_3$. Whilst $BaTiO_3$ has a very high dielectric constant, it also has a low Q value and a rather large τ_f. Given the need for all three desirable dielectric characteristics to co-exist simultaneously, $CaTiO_3$ or $SrTiO_3$-based systems are better candidate materials systems from this point of view. $CaTiO_3$, for instance, has both a relatively high dielectric constant (~ 170) as well as a relatively high $Q \cdot f$ value (3,500 GHz). Its τ_f value (+850 ppm/K), however, is far too high. The high starting dielectric constant of $CaTiO_3$ (or $SrTiO_3$) provides the possibility to tune their $Q \cdot f$ and τ_f values at the expense of the dielectric constant whilst still maintaining a value over 75. Various authors to date have also attempted to tune the dielectric properties of $CaTiO_3$ by forming mixtures of it with other compounds such as $ReAlO_3$ (*Re*: rare earth element *e.g.* La^{3+}, Sm^{3+} and Nd^{3+}) [4,7] and $Re_2Ti_2O_7$ as well as further mixtures thereof *e.g.* $Ca_{1-x}Re_{2x/3}TiO_3$-$ReAlO_3$ [8]. In this thesis, a particular $CaTiO_3$-doped system which has been reported to exhibit promising dielectric properties [Kim et al, 30], namely the $Ca_{1-x}Sm_{2x/3}TiO_3$, $0 \leq x \leq \sim 0.6$, system, has been synthesised and its structural and dielectric properties systematically investigated.

The end-member $CaTiO_3$ structure is of *GdFeO*$_3$ perovskite-related structure type, as shown in Figure 1-3 below. This *GdFeO*$_3$ structure type has space group symmetry *Pnma*, $\sqrt{2}a_p \times 2a_p \times \sqrt{2}a_p$ (subscript p for the underlying parent perovskite

structure type) and differs from the ideal parent perovskite structure type in that there exist non-zero octahedral rotations around the *a* and *b* axes as are apparent in Figure 1-3 below.

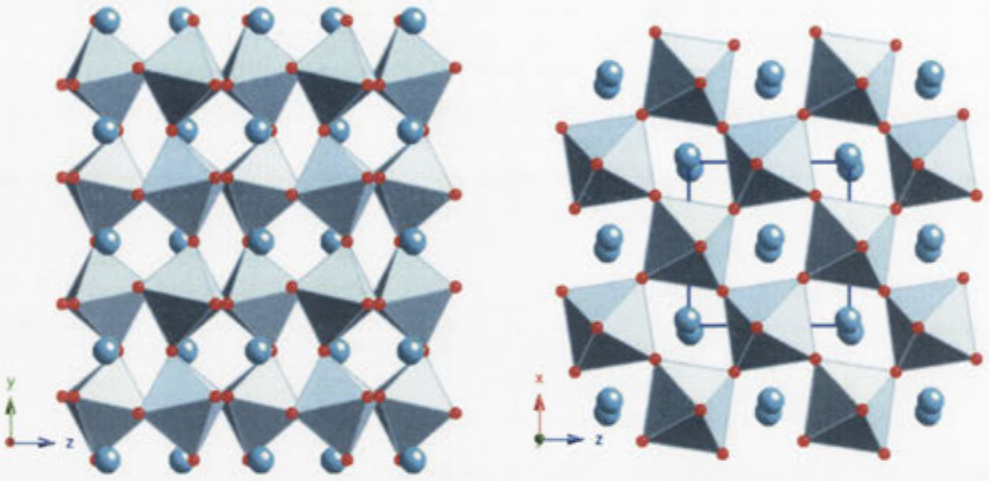

(a) (b)

Figure 1-3 The reported room temperature crystal structure of $CaTiO_3$ in projection along the (a) [100] and (b) [010] zone axis directions. The TiO_6 octahedra are shown in blue, the Ca ions are represented by the large blue balls while the oxygen ions are represented by the small red balls.

1.4 Outline of the Thesis

The aim of this thesis is to describe the work performed in the search for a deeper understanding of the relationship between dielectric properties and structure (both average as well as local) of the dielectric ceramic materials described above from both the fundamental materials chemistry, as well as materials engineering, points of view.

The thesis consists of 8 chapters. The second chapter describes background information on the experimental methods used in synthesis, structural characterisation and physical properties measurements of the ceramic samples produced.

Chapter 3 describes the measurement methods and procedures used to obtain both the reported dielectric properties. Descriptions of the home-made sample

holders and computer programs necessarily developed during the course of this thesis to enable the dielectric properties to be measured are also presented in this chapter.

In Chapter 4, the synthesis, dielectric properties and average structure determinations of two 'misplaced displacive', Bi-based cubic pyrochlore phases found in the Bi_2O_3-$M^{II}O$-Nb_2O_5 (M = Mg^{2+} and Ni^{2+}) systems are reported. In addition, the relationship between the local crystal chemistry and the inherent compositional and displacive disorder of these Bi-based cubic pyrochlore phases is investigated via electron diffraction and bond valence sum analysis.

In Chapter 5, two Bi-based niobate pyrochlore phases which have both previously been reported to occur at the nominally ideal $Bi_2(M^{III}Nb^{V})O_7$ stoichiometry without any compositional disorder on the pyrochlore A site, namely the Bi_2InNbO_7 (BIN) and Bi_2ScNbO_7 (BSN) pyrochlore systems, are synthesised and carefully examined in order to establish whether or not A site stoichiometric, Bi-based niobate pyrochlores can really exist and to investigate the nature of their dielectric relaxation properties. In addition, electron diffraction is again utilised to investigate the inherent displacive disorder of these A site stoichiometric, Bi-based niobate pyrochlores.

In Chapter 6, the results of a synthesis and dielectric properties investigation of a non-bismuth based pyrochlore system apparently analogous to the above Bi-based pyrochlore systems, namely $Ca_{1.5}NbTi_{1.5}O_7$ (CNT), are presented in order to establish whether or not the low temperature dielectric relaxation properties of the inherently disordered Bi-based pyrochlore systems necessarily require Bi occupancy of the pyrochlore A site. It is thereby established that the presence of Bi on the pyrochlore A site is not required.

In Chapter 7, the synthesis as well as the relationship between local crystal structure, microstructure and dielectric properties of the $(1\text{-}x)CaTiO_3$-$xSm_{2/3}TiO_3$ or $Ca_{1-x}Sm_{2x/3}TiO_3$ (CST, $0 \leq x \leq \sim 0.6$) system, are reported.

Finally, the conclusions drawn from this study are finally presented in Chapter 8.

Chapter 2: Experimental Methods

This chapter describes the experimental methods used in the synthesis, structural characterisation and physical properties measurements of the ceramic samples produced during the course of this thesis.

2.1 Introduction

This section introduces the experimental methods used in the results and discussion chapters that follow. It is divided into three parts: (a) methods used in sample synthesis, (b) methods employed in structural and compositional characterisation and (c) methods employed in dielectric properties characterisation.

2.2 Sample Synthesis

The major problem that needs to be overcome in conventional solid state synthesis relative to wet chemical synthesis is the typically slow diffusion rates in the solid state. These slow diffusion rates make it difficult to get the starting materials to mix properly and react uniformly. Two main routes are open in order to overcome this problem: (a) increasing the reaction temperature thereby increasing the diffusion rate or (b) decreasing the particle sizes of the starting solids thereby decreasing the diffusion distances required and increasing the surface energy. These two routes can often be combined. Reducing particle size is usually achieved via some form of grinding. Due to the reduction in particle size, however, a substantial amount of the starting material can sometimes be lost as dust if precautions are not taken. Grinding is thus normally carried out under a liquid to prevent fine particles from leaving. The liquid used should of course be easy to evaporate and not react with the sample.

The pyrochlore and perovskite type samples investigated in this thesis were prepared either via conventional solid-state reaction at relatively high temperatures and/or via lower temperature wet chemical synthesis, in particular via metalorganic decomposition routes. The former method is cheaper and more convenient in terms of the availability of the metal oxide and/or carbonate starting materials and was usually employed to prepare bulk samples. The latter, wet chemical synthesis route required the use of more expensive initial metalorganic reagents but could produce highly homogeneous samples and usually be carried out at significantly lower temperatures.

2.2.1 Synthesis via the Solid State Route

The starting materials used in the solid state synthesis route were the appropriate metal oxides or metal carbonates (see the list given in Table 2-1) of the metal elements in the target compounds. The initial syntheses assumed a particular composition for the target pyrochlore or perovskite phase. The oxides/carbonates appropriate for these compositions were first dried at 120 °C overnight to eliminate adsorbed moisture and any water of hydration. The dry starting materials were then homogeneously mixed in acetone for 30 minutes using an agate mortar, then calcined typically at 800-1000 °C for one day allowing decomposition of the metal carbonates and initial reaction to occur followed by regrinding in acetone for a further 30 minutes. Fine powders of the sample were then added to a stainless steel die of 12 mm diameter and uniaxially pressed using a hydraulic press into pellets at a pressure of ~ 500 MPa for 1 minute. The obtained pellets were then sintered at higher temperatures ranging from 1000 °C to 1500 °C for periods typically ranging from a minimum of 2 hours up to a maximum of 72 hours (see Table 2-2; further details on the short-hand labels for the phases listed in Table 2-2 are given in the list of abbreviations on page xiii and the synthesis procedures used to obtain them are given in the individual Chapters that follow).

After each period of thermal treatment, the samples were first checked for phase purity using powder XRD. Further annealing was then carried out until no changes in the XRPD pattern could be detected, at which point equilibrium was deemed to have been reached. If contamination phases were present in the final XRPD pattern, the initial composition was changed until the desired single phase product was obtained (see Figure 2-1 for the process involved and Figure 2-2 for the equipment used).

Table 2-1 Starting materials used in this study.

Elements	Starting oxides / carbonate	Manufacture	Purity (%)
Al	Al_2O_3	Alpha - Ventron Inorganics	99.99
Ba	$BaCO_3$	NOAH Chemical	99.9
Bi	Bi_2O_3	Koch-Light Laboratories	99.995
Ca	CaCO3	Hudson Laboratories	99.999
Cu	CuO	Univar	97.5
Fe	Fe_2O_3	Aldrich	99.99
In	In_2O_3	Aldrich	99.99
La	La_2O_3	MC- Michigan Chemical Corporation	99.9
Mg	MgO	AnalaR	98
Nb	Nb_2O_3	Alfa - Morton Thiokol, Inc.	99.9+
Ni	NiO	Sigma - Aldrich	99.99
Sb	Sb_2O_5	The British Drug Houses Ltd.	99.99
Sc	Sc_2O_3	Hudson Lab.	99.99
Sm	Sm_2O_3	Aldrich	99.9
Ti	TiO_2	Aldrich	99.9
Zn	ZnO	Univar	99.5

Table 2-2 Synthesis conditions used in the solid state route.

Phase Label	First calcining temperature (°C)	Sintering temperature (°C)	Sintering period (hours)
BIN	800	1050	48
BMN	800	1050 - 1150	3 - 72
BNN	800	1050 - 1150	3 - 72
BSN	800	1000	48
CNT	850	1000 - 1350	3 – 72
CST	1200	1350 - 1500	3 – 72

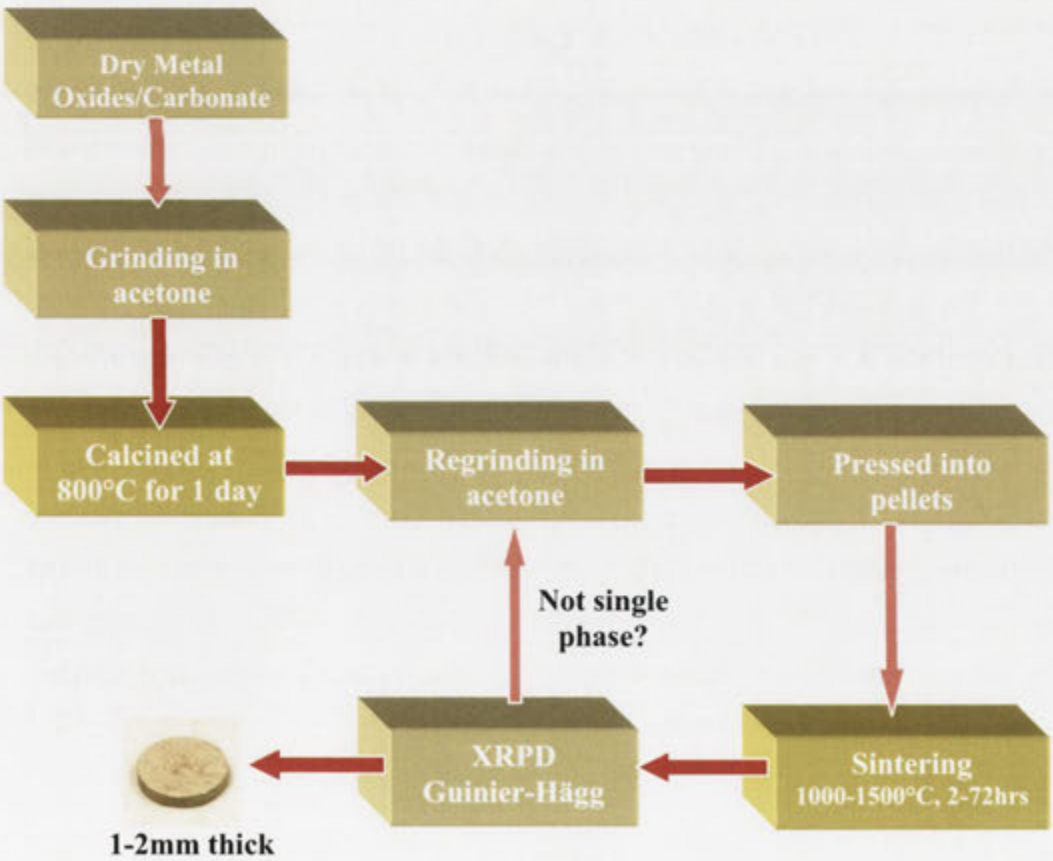

Figure 2-1 Procedures involved in the solid state synthesis route.

Figure 2-2 The equipment used in the solid state synthesis route a) agate mortar and pestle for grinding, b) alumina and platinum crucibles, c) die for pressing pellets and d) high temperature furnace.

2.2.2 Synthesis of Samples via the Metalorganic Decomposition Route

The $Ca_{\sim 1.5}Ti_{1.5}NbO_7$ (CNT) cubic pyrochlore sample was synthesised via a metalorganic decomposition route (the process used is shown in Figure 2-3 below) in order to lower the required sintering temperature and to obtain a fully dense sample suitable for dielectric properties measurements.

The starting reagents used (see Table 2-3) were titanium (IV) isopropoxide ($Ti[OCH(CH_3)_2]_4$), niobium (V) chloride ($NbCl_5$), and calcium nitrate ($Ca(NO_3)_2$). Highly pure ethanol (C_2H_5OH) was chosen as the solvent. Niobium (V) chloride and calcium nitrate were first dissolved in ethanol at room temperature. The resultant solution became clear and was then heated up to 80 °C for 30 minutes to drive off water. Titanium (IV) isopropoxide was then added to the solution. The resultant transparent solution was then stirred at this temperature until the solvent evaporated. The resultant powder was then heated at 250 °C for 2 hours to completely remove any water of crystallisation and residual solvent. This was followed by heating at 580 °C to remove inorganic groups such as NO_3^- ions. The resulting solid mixture was finally ground into a fine power in acetone using an agate mortar and pestle and then calcined at 850 °C for 12 hours. After re-grinding in acetone, the powder was then pressed into a 1 mm thick and 12 mm diameter pellet and sintered at a higher temperature of 1000 °C for a further 3 days.

Table 2-3 Starting materials used in metalorganic decomposition method.

Elements	Starting chemicals	Manufacture	Purity (%)
Ca	$Ca(NO_3)_2$	Aldrich	99.9
Nb	$NbCl_5$	Aldrich	99.995
Ti	$(Ti[OCH(CH_3)_2]_4)$	Aldrich	99.999%

As for the solid state route, the resultant samples were checked after each period of thermal treatment using powder XRD until no change in the XRPD patterns could be detected, at which point equilibrium was again deemed to have been reached.

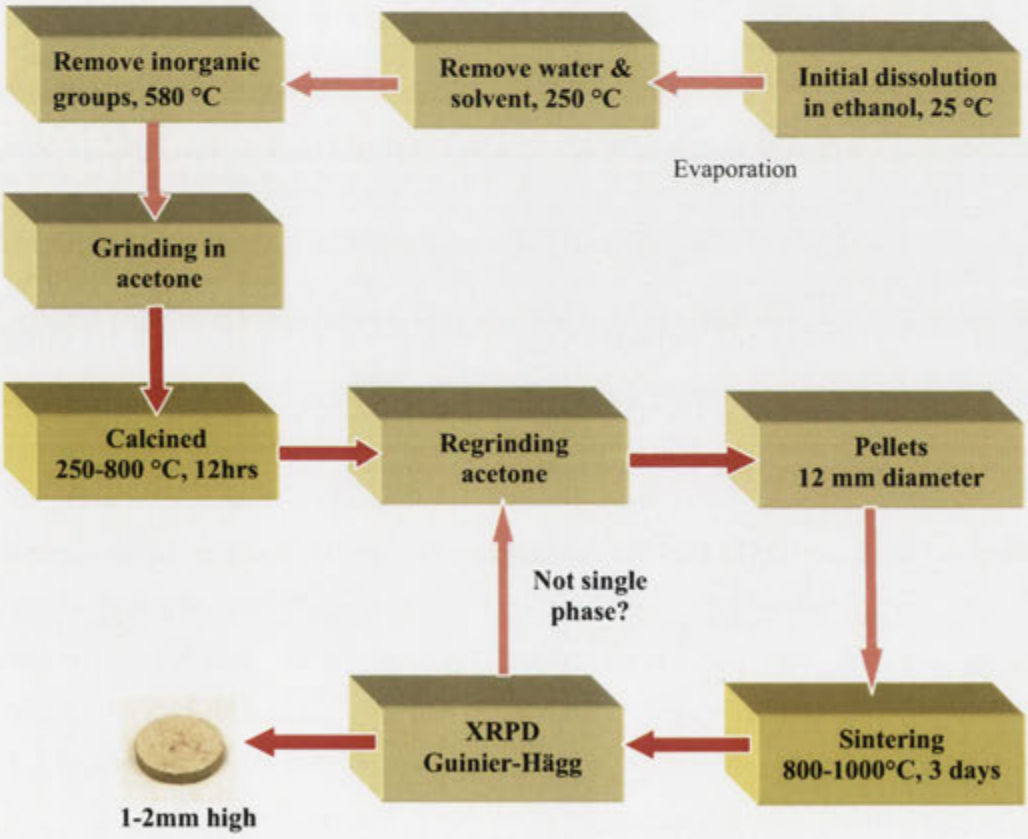

Figure 2-3 Procedures used in the metalorganic decomposition route.

2.3 Structural Characterisation Methods

A variety of analytical techniques were used for unit cell and space group determination, for compositional analysis of synthesised samples, for average structure determination and for detection of compositional and/or displacive disorder.

2.3.1 Laboratory based X-ray Powder Diffraction (XRPD)

Laboratory based X-ray powder diffraction was invariably the first analytical technique employed to study the samples synthesised. It was used initially to determine if the samples synthesised were, or were not, single phase, then to determine the single phase unit cell parameters and to investigate space group symmetries. In the case of the disordered cubic pyrochlores, special care had to be taken in the indexing of the XRD patterns to look for certain weak reflections, *e.g.* 442, 446 *etc.*, diagnostic of inherent compositional and/or displacive disorder [17,20,28,31,32,33]. Note that even, even, even reflections of the type $h + k + l \neq 4n$ (n an integer) such as 442, 446 *etc.* are forbidden for the ideal cubic pyrochlore structure type as a result of the fact that the *A* (16*d*), *B* (16*c*), O (48*f*) and O' (8*b*) atoms are each on special positions which all require this $h + k + l \neq 4n$ condition.

Powder X-ray diffraction was carried out using both a Siemens D-5000 diffractometer (see Figure 2-4a) and a Guinier–Hägg camera (see Figure 2-4b) using $Cu_{K\alpha 1}$ radiation (λ = 1.54059 Å). High purity Si (Lot GD#1 [34], a = 5.431195(9) Å at 22.5 °C or Sietronics Lot # GD1, a = 5.431115 Å) was added to the samples to act as an internal standard, while the sample unit cell dimensions were refined using the program "Unitcell" [35]. The focussing geometry of the Guinier–Hägg camera provides very narrow peak shapes enabling more accurate determination of the average structure unit cell dimensions of the samples (~ 0.01 %). A further advantage of the Guinier camera technique is the very small amounts of sample needed. However, the intensities of the lines in Guinier-Hägg films (see Figure 2-5 below) are often difficult to integrate or to be used in Rietveld analysis.

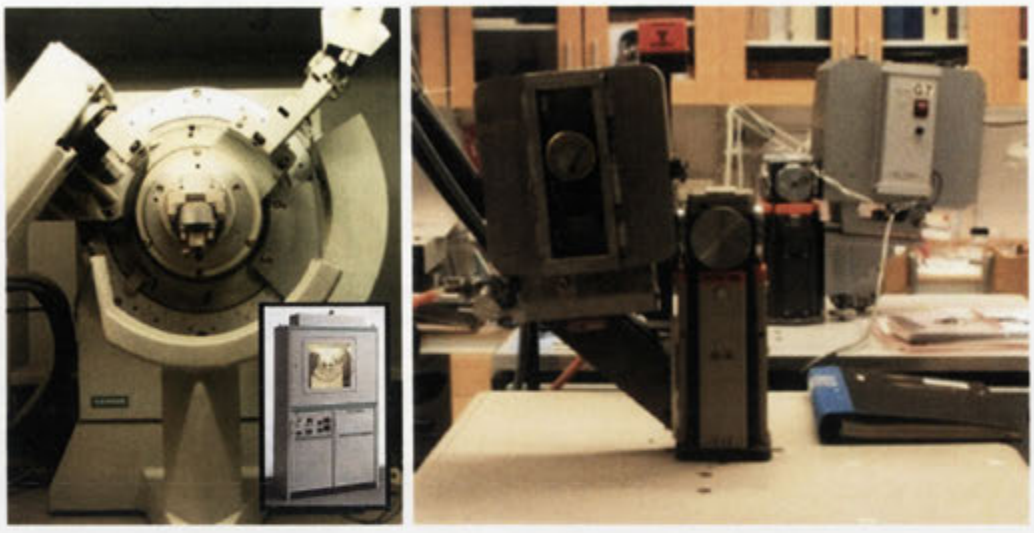

(a) (b)

Figure 2-4 Laboratory XRD diffractometers used for powder XRD analysis: (a) the Siemens D-5000 Diffractometer and (b) the Guinier–Hägg camera.

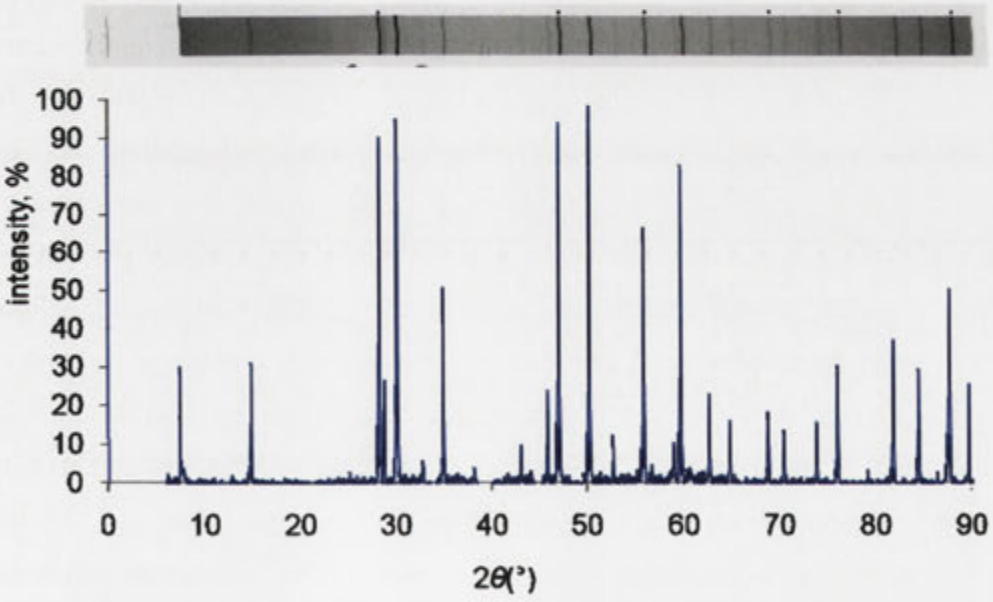

Figure 2-5 A typical Guinier–Hägg film (top) and the corresponding scanned profile (below).

2.3.2 Electron Probe Microanalysis (EPMA)

There are several situations where XRD alone may not provide sufficient information to characterise the synthesised product. For example when performing synthesis at elevated temperatures it is possible to partially volatilise reagents during synthesis. Although XRD may report a single phase and provides accurate unit cell parameters, the loss of reagent may remain unnoticed. In other cases it is possible that, upon quenching, a well defined crystalline phase forms but a second phase also quenches as an amorphous glass. In this case, the presence of a second (amorphous) phase gives rise to a weak characteristic undulating background. This, however, is often difficult to detect. An independent analysis is therefore useful to provide additional information. In this case electron probe microanalysis (EPMA) was used to check the final composition as well as confirm the homogeneity of the various synthesised samples.

EPMA involves bombarding the atoms in the sample with a beam of electrons, causing them to generate X-ray photons at energies (wavelengths) characteristic of the elements which are in the sample. These X-rays can then be collected using either energy dispersive (EDS) and/or wavelength dispersive (WDS) detectors [36] and are plotted as a spectrum of energy (or wavelength), versus intensity. The spectrum provides not only confirmation of the elements present in the sample but can also be used to provide quantitative information. A first approximation of the concentration of a given element in an unknown sample can be obtained by calculating the ratio of the intensity of its characteristic peak in the unknown sample to that of the same peak in the spectrum of a well defined calibration standard. Because of likely differences in atomic number, absorption of X-rays and secondary fluorescence, corrections need to be applied to arrive at a final concentration. Note that the typical accuracy of quantitative EPMA using carefully selected calibration standards can be better than ~ ±2 % relative (see *e.g.*[37]) and that regions <2-5 μm (depending on atomic number) can be selected for individual compositional analyses.

All quantitative analysis presented in this thesis were performed at 15 kV and 1 nA using a JEOL 6400 Scanning Electron Microscope (SEM) (equipped with an

Oxford Instruments light element EDS detector and Link ISIS SEMquant software) In order to minimise atomic number, absorption and fluorescence (ZAF) corrections [36], standards close in composition to the unknown were chosen wherever possible. The calibration standards used for the analyses presented in this thesis are shown in Table 2-4.

EPMA analysis was particularly important in the case of the Bi-based pyrochlore samples where Bi evaporation during high temperature annealing was always a possibility.

Table 2-4 Elemental standards used in EPMA analysis

Elements	Standards	Elements	Standards
Al	$NaAlSi_3O_8$	Mg	MgO
Ba	$BaSO_4$	Nb	$BiNbO_4$
Bi	$BiNbO_4$		or NbO_2F
Ca	$CaZrTi_2O_7$	Ni	Pure Ni
Fe	Fe_2O_3	Sb	$Sb_7Ge_{23}S_{70}$
La	$LaSb_2Sn_{0.6}$	Ti	TiO_2

Samples prepared for quantitative analysis were mounted in 25mm epoxy resin discs and polished to a < 0.5 μm finish using diamond paste. To enable imaging and analysis on the non-conductive samples synthesised, the polished samples were coated with a ~20 nm thick layer of carbon (see Figure 2-6 below). Since the sample is bombarded with electrons, the carbon coating is essential to dissipate any electric charge that would build up on the surface of what would otherwise be an insulating sample.

Figure 2-6 Carbon coated polished sample molds

2.3.3 Imaging in the SEM

In addition to the EDS detector, the JEOL-6400 SEM is also equipped with secondary electron (SE) and back-scattered electron (BSE) detectors to generate magnified detailed images of the surface. The SE signal generally provides high resolution topographical detail and is therefore particularly useful when examining rough surfaces and highlights any three-dimensional nature of the specimen. The intensity of BSE emission is proportional to the average atomic number of the area illuminated; the BSE signal is therefore useful in visualising potential variations in atomic number. This can be particularly useful in quickly assessing if a sample contains more than one phase. SE and BSE imaging were thus used to investigate the compositional homogeneity, texture and morphology of the samples produced as well as to look for any morphological transformations that may have occurred during the sintering process.

2.3.4 Electron Diffraction

Electron diffraction is ideally suited to the detection of weak features of reciprocal space such as structured diffuse scattering as a result of the strong interaction of electrons with matter (electrons scatter some 10^4-10^5 times more strongly than X-rays). Such structured diffuse scattering gives important information as it can be interpreted in terms of the local crystal chemistry of disordered materials *i.e.* the local distribution of available ions on the partially occupied sites and/or the associated or inherent displacive shifts responsible for the observed diffuse scattering. This is important in the case of the inherently compositionally and/or displacively disordered pyrochlore and perovskite phases which are the subject of this thesis. Figure 2-7, for example, shows (a) ~ <118> and (b) ~ <551> zone axis electron diffraction patterns (EDP's) typical of the 'misplaced-displacive' BZN cubic pyrochlore (courtesy of Prof. Ray Withers). The highly structured diffuse intensity distribution apparent in such EDP's gives important information as to the nature of the local compositional and associated displacive disorder occurring in this material [18,38,39]. The detection and interpretation of such structured diffuse scattering and its implications as regards dielectric properties is an important component of this thesis.

The electron diffraction patterns (EDPs) in this thesis were obtained using a Philips EM 430 TEM operating at 300 kV. Sample grids suitable for transmission electron microscopy were prepared by crushing the compounds in butanol and dispersing them onto lacey carbon coated TEM grids.

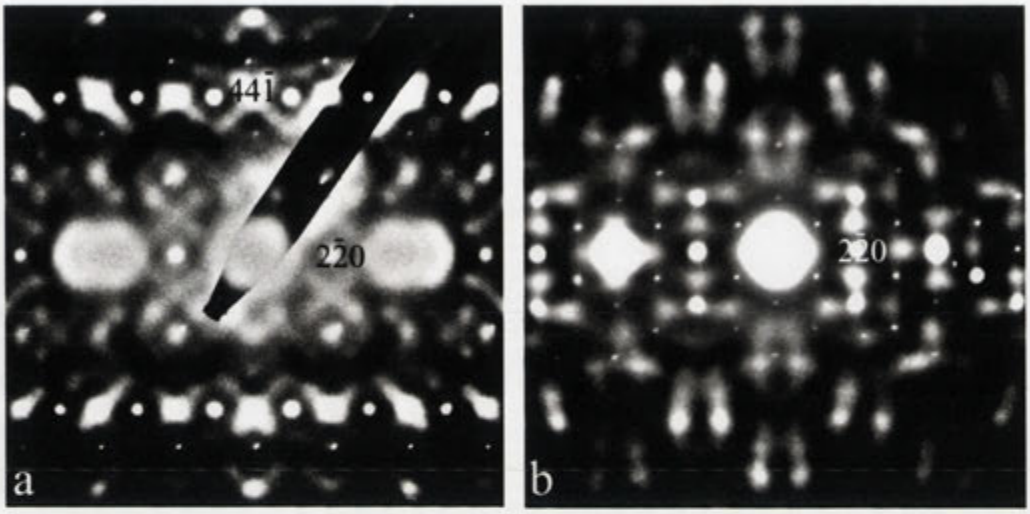

Figure 2-7 (a) ~ <118> and (b) close to <551> zone axis electron diffraction patterns (EDP's) typical of the 'misplaced-displacive' BZN cubic pyrochlore (courtesy of Prof. Ray Withers).

2.3.5 Neutron Diffraction

The X-ray and neutron diffraction experiments performed in this thesis were of both transmission and reflection geometry in the case of X-ray diffraction but only of transmission geometry for neutron diffraction. The main difference between the two techniques used however, is the interaction between the "probe" (the radiation type) and the scattering of that probe. X-ray diffraction is a very convenient tool for determining the positions of heavy elements (with many electrons) which dominate the scattering of X-rays. On the other hand, neutron powder diffraction is preferred when more detailed information regarding the positions of lighter atoms in a matrix of heavier atoms is needed, as for example when structural information on the oxygen positions in a typical oxide perovskite are required. This is because the atomic scattering power for neutrons (called the scattering length) depends primarily on the nuclei involved and their relative position and is largely independent of the number of electrons that surround the atom [40]. In addition, this scattering is often

strongly isotope dependent so the same element can have vastly different scattering lengths for its different isotopes. The scattering length also does not scale linearly with atomic number, like the scattering of X-rays does, so light atoms can scatter neutrons as strongly as or stronger than the heavier atoms in the structure (see *e.g.* Figure 2-8).

The sensitivity of neutrons to lighter atoms such as oxygen is thus fairly high, and often as good as the heavy atoms. Refinement of neutron diffraction data was thus used to model and refine oxygen positional parameters as well as those of the metal atoms in this thesis. The neutron powder diffraction data were collected at room temperature (298 K) using the High Resolution Powder Diffractometer (HRPD) at the High Flux Australian Reactor (HIFAR) with a wavelength of ~1.49 Å [41]. The samples were placed in a vanadium canister of 10 mm diameter and continuously rotated during data collection which was carried out in 0.05° steps between 0.027° and 150.027° in 2θ. This powder diffraction data was then refined using the Rietveld method.

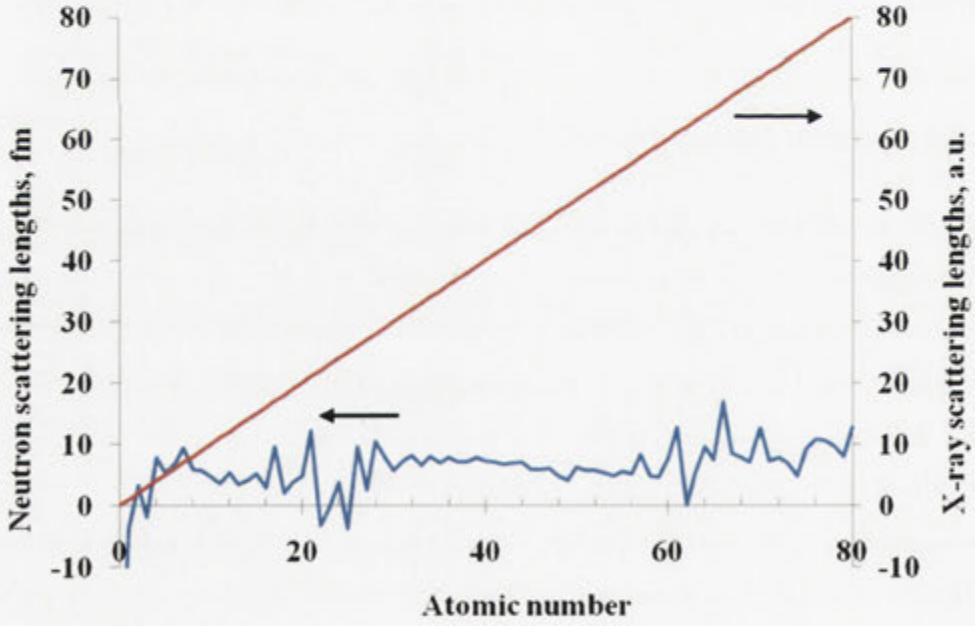

Figure 2-8 Comparison of atomic scattering lengths for X-rays and neutrons [42].

2.3.6 The Rietveld Analysis of Neutron Diffraction Data

The Rietveld method is a non-linear least squares refinement method, whereby the positions and intensities of the peaks in a calculated diffraction profile are compared to the diffraction peaks in an experimental data set (see the example given in Figure 2-9). By minimizing the difference between the calculated pattern generated by a certain structural model and the observed peaks, a probable model of the structure can thereby be obtained.

The Rietica for Windows software package [43] was used for Rietveld structural refinement of the obtained room temperature neutron powder diffraction profiles. Data below 8° and above 150° in 2θ were treated as excluded regions. The unit cell values obtained for the samples via X-ray powder diffraction were used as starting numbers to refine the neutron beam wavelength to $\lambda_{neutron}$ = 1.4913(2) Å (given as ~ 1.49 Å by the diffraction facility) which was then fixed.

The background was modelled using a 6th order Chebyshev-II–type polynomial. The peak shape was refined using a Pseudo-Voigt model, described using four refinable parameters. The structural parameters refined were atomic coordinates, site occupancies and atomic displacement parameters (ADP's), both isotropic and anisotropic. The fractional co-ordinates and ADP's for both ions located on the ideal pyrochlore *A*-sites as well as for those on the *B*-sites were always constrained to be equal.

The relevant refinement statistics used to describe the fit were $\mathbf{R_{Bragg}}$, $\mathbf{R_p}$, $\mathbf{R_{wp}}$, $\mathbf{R_{exp}}$ and $\boldsymbol{\chi}^2$. The fitting statistic most closely resembling the traditional single crystal R factor is $\mathbf{R_{Bragg}}$. This fitting parameter describes the quality of the fit of the model structure to the experimental data independent of the background and is based on the "observed" integrated *intensities* (*I*) obtained for each theoretical reflection (K) in the pattern.

$$R_{Bragg} = \frac{\sum \left| I_K^{obs} - I_{K_i}^{cal} \right|}{\sum I_K^{obs}} \qquad (2\text{-}1)$$

The $\mathbf{R_p}$ fit index also relates the structure model to the observed pattern. In this case, however, the fit is related to each *data point* (y) in the pattern where the calculated value for a data point is based on one or several theoretical reflections that (depending on peak profile) can contribute to that point including the calculated background.

$$R_w = \frac{\sum \left| y_i^{obs} - y_{i_i}^{cal} \right|}{\sum y_i^{obs}} \qquad (2\text{-}2)$$

The $\mathbf{R_{wp}}$ fitting parameter is also based on the intensities at each data point in the whole pattern but in addition a weighting scheme (w) is added, usually based on counting statistics.

$$R_{wp} = \sqrt{\left[\frac{\sum w_i (y_i^{obs} - y_{i_i}^{cal})^2}{\sum w_i (y_i^{obs})^2} \right]} \qquad (2\text{-}3)$$

Based on the number of refined parameters (P) and the number of "observations" (N) an 'expected R-value', R_{exp}, is calculated for the pattern

$$R_{Exp} = \sqrt{\frac{N-P}{\sum w_i (y_i^{obs})^2}} \qquad (2\text{-}4)$$

The final parameter χ^2 indicates the quality of the overall fit between the calculated and observed patterns (including the background) based on what can be expected in regards to the number of observations and the number of parameters used in the refinement.

$$\chi^2 = \frac{\sum w_i (y_i^{obs} - y_i^{cal})^2}{N-P} = \left[\frac{R_{wp}}{R_{Exp}} \right]^2 \qquad (2\text{-}5)$$

The various R values should generally be refining to values that are as low as possible whilst the "goodness of fit" parameter, χ^2, should be close to a value of 1. A value far below 1 for χ^2 is an indication that something is seriously wrong with the

refinement. Often it means that the model has more parameters than can be justified based on the data quality. For instance, the counting statistics are bad or the background is high *etc*. The best way to indicate the quality of the fit is to graphically show this in a plot. It is easier to visually verify the goodness of the model than to solely rely on refinement statistics. A graphical representation can also show that a model is good even though the statistics may initially look bad due to *e.g.* the presence of a contamination phase, magnetic scattering, strain effects *etc.*

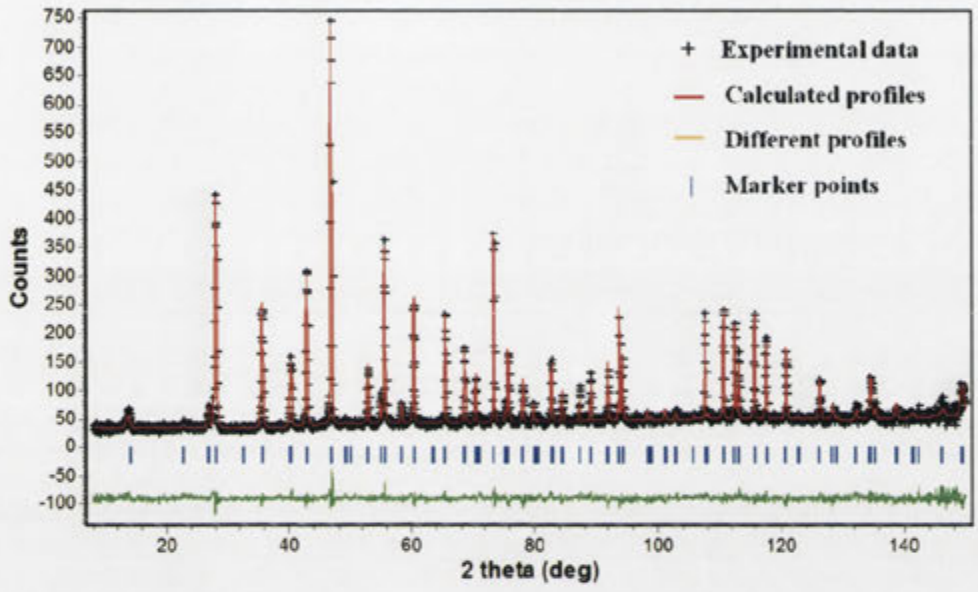

Figure 2-9 Neutron powder diffraction pattern of $Bi_{1.66}Mg_{0.70}Nb_{1.52}O_7$ refined using the Rietveld method (cross: experimental data point, line: the calculated profile fit, vertical bars on the bottom: the positions of allowed Bragg reflection, the bottom line: different profile).

2.4 Physical Characterisation Methods

2.4.1 Density Measurement

The density of ceramic samples can have a significant effect on their measured dielectric properties as the presence of air will hinder the flow of charge through the materials and thus degrade their intrinsic dielectric properties. It is thus crucial that the sample pellets produced should be sufficiently dense and non-porous for good dielectric properties measurements.

The density of the sintered samples produced was typically measured by the Archimedes water displacement method, widely used in the determination of the specific gravity of solids [44]. The ceramic pellets were first polished using a variety of grades of sand paper until a smooth surface was obtained. The weight of the samples was then recorded in both air and water on a bench-top scale balance (accuracy of ±0.0001 g at room temperature). The density of the sample was then estimated from the following formula:

$$\rho_{sample} = \frac{\rho_a}{\rho_w \times \rho_{water}} \qquad (2\text{-}1)$$

where:

ρ_a: density of dry sample in air.

ρ_w: density of the sample soaked in water

ρ_{water}: density of water at room temperature (25°C), and is $1.0 g.mL^{-1}$

The density of the sample was also calculated from the volume (V) and mass (m) of the pellet:

$$\rho_{sample} = \frac{m}{V} \qquad (2\text{-}2)$$

The measured density was then expressed in terms of a percentage of the theoretical density of the crystal (ρ_c) which was calculated from the unit cell volume (V_c):

$$\rho_c = \frac{Z \times M}{N_a \times V_c} \qquad (2\text{-}3)$$

where:

N_a is Avogadro's number,

Z is the number of formula units per unit cell,

M is the molecular weight of a formula unit

This relative density should ideally be greater than 95 % in order to give reliable measured dielectric properties [45].

The pellets with lower relative densities were typically re-sintered for longer times or/and at higher temperatures to achieve higher relative densities.

2.4.2 Raman Spectroscopy

Raman spectroscopy is a method that uses inelastic scattering of incident monochromatic photons from a laser source to study vibrational, rotational or other **k** = **0** symmetric modes of distortion in a crystalline material. It is a complementary technique to infrared spectroscopy and is used in this thesis to investigate temperature-dependent changes in local structure. In this study, Raman spectra of pellet samples were obtained using a Spectra Physics 164 Argon ion laser.

2.5 Dielectric Properties and Characterisation

The electronic properties of conductors and semi-conductors arise from electron and/or hole carrier transport. In an ideal insulator, however, there are no such free electrons. Nonetheless, such materials usually consist of positively and negatively charged particles. These charges balance each other macroscopically in the absence of an external electric field giving rise to overall charge neutrality of the material [46]. Once an electric field is applied, this charge balance is perturbed as a result of a limited spatial rearrangement resulting in the formation of a macroscopic dipole moment. These types of insulating materials are known as dielectric materials. All insulators are dielectric materials but do not have to be good dielectric materials.

Dielectric properties are strongly structure related according to the following microscopic polarisation mechanisms [47] (see also Figure 2-10 below):

electronic polarisation (α_e) arises as the result of a small displacement of the electrons in an atom relative to the nucleus and is active up to ~ 10^{15} Hz. Its contribution can lead to dielectric constants or permittivities (k) up to ~ 5.

ionic polarisation (α_i) involves relative displacements of the cation and anion sublattices from their equilibrium positions and give rise to ionic dipoles. This

mechanism is correlated with lattice vibrations and can respond to applied frequencies up to ~ 10^{13} Hz. Normally, its contribution to the dielectric constant falls between 10 and 60.

dipolar polarisation (α_d) arises from the re-orientation and alignment of permanent dipoles due to an external applied electric field. It can respond to applied fields for frequencies up to 10^8 to 10^{11} Hz, and can make contributions to the dielectric constant ranging from 10^2 to 10^4.

space charge polarisation (α_s) involves a limited transport of charge carriers until they are stopped at a potential barrier, typically a grain boundary or a phase boundary. This results in a spatial distribution of charge centres over the microstructure. Depending on the conductivity (mobility) and barrier separation distances, space charge dipoles can respond to applied fields for frequencies typically up to 10^3 Hz. Space charge dipoles can contribute ~10^5 to measured dielectric constants.

Depending on the frequency of the applied electric field, real dielectric materials have a dielectric response arising from one or more of these polarisation mechanisms (Figure 2-11). Polarisation is therefore expressed as:

$$P = \alpha_{total} E = \varepsilon_0 (1 - \varepsilon_r) E \qquad (2\text{-}4)$$

where ε_0 is the dielectric constant of a vacuum, equal to 8.854 x 10^{-12} C^2 $J^{-1}m^{-1}$, ε_r is the relative dielectric constant of the dielectric material and E is the external electric field. This equation links the observed macroscopic polarisation to the various possible microscopic polarisation mechanisms. From the equation, it can be noted that upon application of an electric field, the charges in the material will respond in such a way as to reduce the field experienced within the material. That is, if a capacitor of value C_0 under vacuum is filed with a dielectric material, its charge storage capacity (capacitance) increases to a value C [48]. In this way, the dielectric constant of a material can be measured using a simple parallel plate capacitor device, in which $C = \varepsilon_0 \varepsilon_r A / d$, where C is the capacitance of the dielectric material, A is the area of the capacitor and d is the thickness of the dielectric layer.

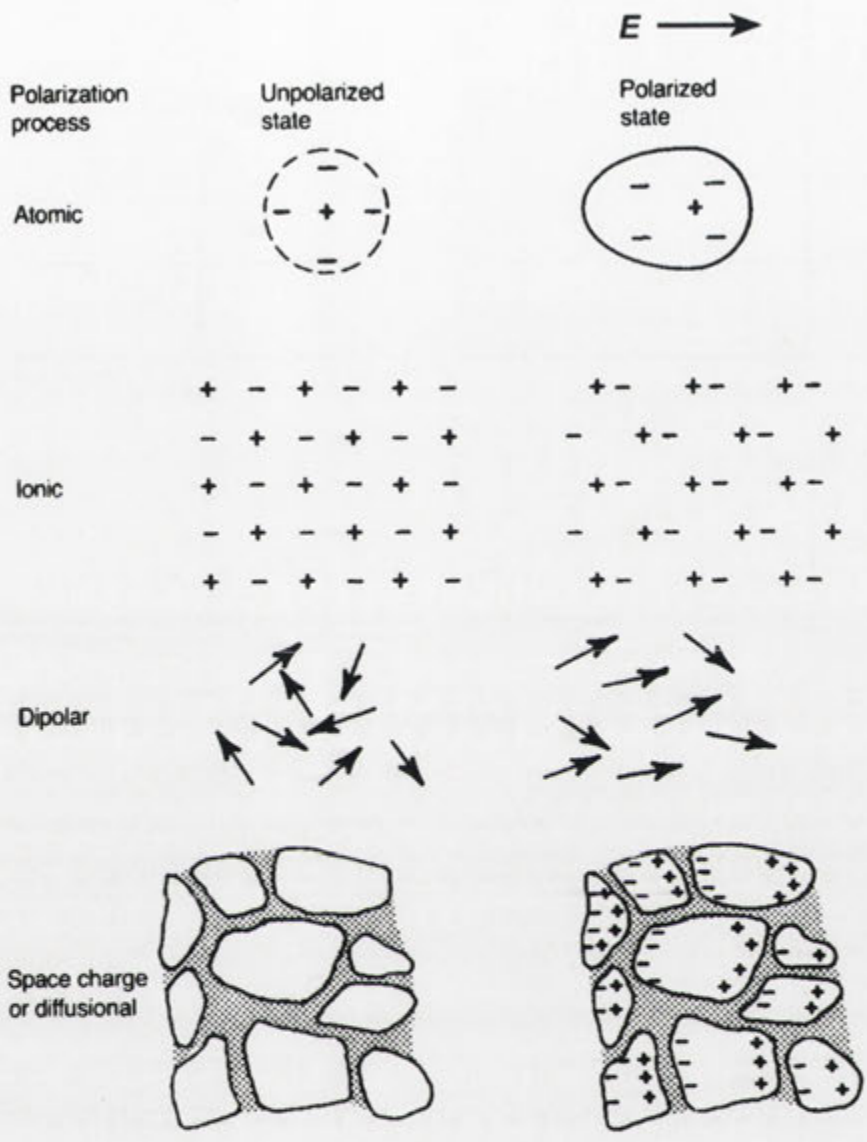

Figure 2-10 The four main polarisation mechanisms in dielectric materials. Unpolarised and polarised states are presented for the atomic, ionic, dipolar, and space charge polarisation [47].

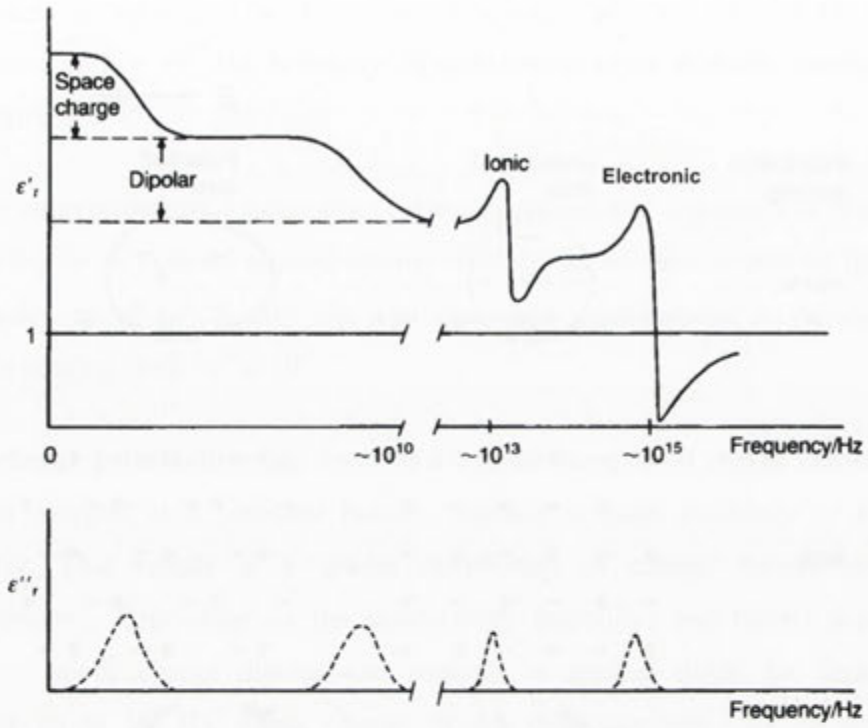

Figure 2-11 Frequency variation of the dielectric permittivity (real and imaginary parts) indicating the contribution from each of the polarisation mechanisms. The peaks in their imaginary part corresponding to the space charge–dipolar and dipolar–ionic transitions are relaxations. The other two are resonant transitions [47].

Dielectric polarisation can be classified into two classes: static and dynamic. Static polarisation remains unchanged under an applied electric field while dynamic polarisation varies with the applied electric field. In the latter case, the local dipole moments, or the chains (or clusters) responsible for the local dipole moments, need different times and energies to be rotated or switched. The dielectric properties therefore exhibit a strong frequency-dependent character. This phenomenon is known as dielectric relaxation. When the relaxation time required is much faster than the frequency of the applied electric field, polarisation occurs instantaneously. When the relaxation time required is much slower than the frequency of the applied electric field, no polarisation (of that type) occurs. However, when the relaxation time required and the frequency of the applied field are similar, a phase lag occurs and energy is absorbed. This introduces dielectric loss (or a dissipation factor). It is normally quantified by the relationship, $\tan\delta = \frac{\varepsilon''}{\varepsilon'}$ where ε′ is the real portion of the

dielectric constant and ε″ is the imaginary portion of the dielectric constant. It reflects the ratio of the energy dissipated to the energy stored in the material. Typically, the energy dissipated is turned into heat from conduction of electrons flowing through the material or through the anharmonicity of the lattice vibrations [49]. Loss has also been attributed to defects and grain boundaries in polycrystalline materials [50]. Loss increases with porosity (P), which is defined as

$$P = 1 - D \tag{2-5}$$

where D is the ratio of the material's experimental to theoretical density [51]. A lower dissipation factor is optimal in order to retain the maximum signal and to prevent excessive heat generation in devices. Microwave engineers also define the quality factor (Q), which is in fact simply the inverse of the dielectric loss.

In addition to the dielectric constant and the dielectric loss, another important parameter is the temperature coefficient of the dielectric constant that measures the thermal stability of the dielectric properties of a dielectric material to fluctuations in temperature.

The temperature coefficient of the dielectric constant can be evaluated from measurements taken at two different temperatures T_1 and T_2 as follows [52]:

$$\tau_{\varepsilon} = \frac{\varepsilon_{(T_2)} - \varepsilon_{(T_1)}}{\varepsilon_{(T_1)}(T_2 - T_1)} \tag{2-6}$$

The temperature coefficient of the dielectric constant can be positive or negative, depending on the nature of the dielectric material. Changes in temperature can lead to changes in dielectric constant and consequently capacitance. Achieving a material with a close to zero temperature coefficient is one of the most difficult parts in the development of practical dielectric ceramic materials [53]. A material with a small τ_ε variation can often be combined with a material with an opposite sign of τ_ε (e.g. the combination of a material with positive τ_ε and a material with negative τ_ε) to make the overall device temperature stable [54].

In the case of microwave dielectric measurements, the temperature coefficient of resonant frequency, τ_f, is used to assess the temperature stability of

microwave dielectric materials. The temperature coefficient of resonant frequency (τ_f) depends on both the temperature coefficient of the dielectric constant (τ_ε) but also on the thermal expansion of the material (α_L) [55].

$$\tau_f = -\left(\frac{\tau_\varepsilon}{2} + \alpha_L\right) \tag{2-7}$$

In general, the thermal expansion of solid materials is about 10 – 20 ppm/K, therefore, to tune τ_f to near zero, the temperature coefficient of the dielectric constant should be approximately of the same magnitude if both τ_ε and α_L are positive.

In order for materials to be used as resonators and filters, it is important that the resonant frequency not shift significantly between -20°C and +80°C. The temperature coefficient of resonant frequency is often required to be less than 15 ppm/°C in the temperature range of -55°C to 125°C [56].

Chapter 3: Dielectric Measurement System

This chapter describes the measurement methods and procedures used to obtain dielectric properties. Descriptions of the home-made sample holders and computer programs developed during the course of this thesis to enable the dielectric properties measurement process are also presented in this chapter.

3.1 Introduction

The two most important properties of a dielectric material are its dielectric constant (or dielectric permittivity) and its dielectric loss (or dielectric loss tangent). Both parameters, in general, vary as a function of frequency, temperature and electric field. To be able to rapidly and accurately characterise these functional dependences is crucial for insight into the underlying polarisation mechanism/s and, ultimately, for the optimisation of the performance of promising dielectric materials for practical applications.

The conventional method for making low frequency (up to ~1 MHz) measurements of the dielectric properties of solids is to place a dense sample between closely spaced parallel conducting plates (see Figure 3-1) so as to form a so-called parallel plate capacitor. This parallel plate capacitor device is then subjected to an AC voltage and the voltage over, current through and capacitance of the device measured using, in our case, an Agilent 4284A precision LCR meter. These measured electrical properties are then modelled using appropriate AC equivalent circuits (see Figure 3-2) and the associated capacitance, C, and dissipation factor, D, of the resulting capacitor thereby extracted.

The capacitor device was constructed as follows: pellets (diameter ~12 mm and thickness ~1 mm) with greater than 95% relative density were polished and coated carefully with silver paste on both sides, followed by a heat treatment at 550 °C to ensure good electrical contact. The edge of these pellets was then polished to remove any silver coating which may otherwise lead to an electrical short circuit between the two sides of the coated pellet.

The properties of the dielectric material under test in the parallel plate configuration (Figure 3-1) are then modelled as a frequency-dependent capacitance C(ω) in parallel with a frequency-independent resistor R_0 (Figure 3-2a). The DC resistance R_0 takes into account processes such as thermally activated hopping and ionic conduction. The measured capacitance C(ω) is then proportional to the complex dielectric function of the sample material under test as follows:

$$C(\omega) = \varepsilon(\omega)\varepsilon_0 \frac{A}{d} \qquad (3\text{-}1)$$

where:

A is the cross sectional area of the capacitor,

d is the separation between the plates (in general, A >> d) and

$\varepsilon_0 = 8.854 \times 10\text{-}12\ C^2J^{-1}m^{-1}$, is the permittivity in vacuum.

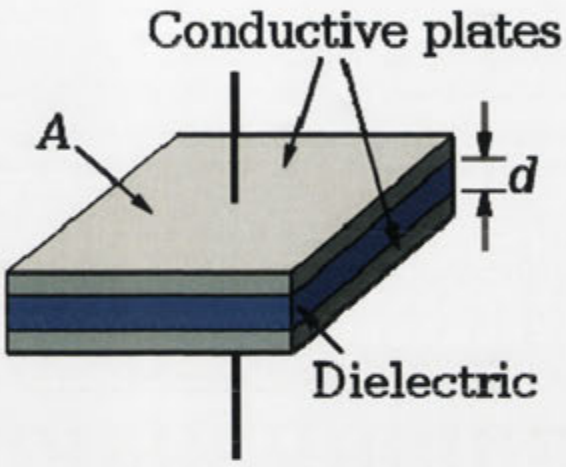

Figure 3-1 Parallel plate electrode

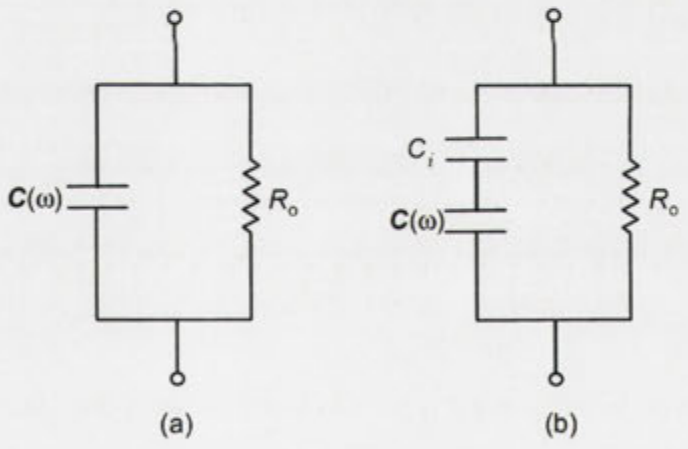

Figure 3-2 Equivalent circuits used for the material under test in Figure 3-1 without (a), or with (b) taking interfacial capacitance into account

The capacitance C measured by a typical capacitance bridge is equal to the real part of

$$C(\omega) = \varepsilon'(\omega)\varepsilon_0 \frac{A}{d} \qquad (3\text{-}2)$$

and so it can be used to extract the frequency dependent, real part of the dielectric function $\varepsilon'(\omega)$ *i.e.* the relative dielectric permittivity (or dielectric constant).

The other measured quantity, the loss tangent (or dissipation factor), $D(\omega)$, given by

$$D(\omega) = \frac{\varepsilon''(\omega)}{\varepsilon'(\omega)} \tag{3-3}$$

can then be used to extract the imaginary part of the dielectric function $\varepsilon''(\omega)$.

The rest of this chapter describes the development of an automated system for measuring dielectric properties including the design of both high temperature (room temperature to 500 °C) and low temperature (room temperature down to liquid nitrogen temperature) sample holders as well as programs to enable automated impedance, dielectric properties versus temperature and non-linear dielectric characterisation measurements.

3.2 Dielectric Measurement

3.2.1 Room Temperature Dielectric Measurement

Room temperature dielectric measurements were performed using a high precision LCR meter (Agilent 4284A) where the frequencies of the applied electric field ranged from 20 Hz - 1 MHz (Figure 3-3). An in-house program was written to enable automatic measurement at multiple frequencies. The program was designed to automatically measure dielectric properties such as dielectric constant, dielectric loss, impedance, and tunability as a function of frequency with or without a bias voltage (see section 3.3 below). The data obtained from the program was then imported to an MS excel spreadsheet program for further analysis.

3.2.2 High Temperature Dielectric Measurement

Temperature-dependent dielectric constant and dielectric loss spectra of samples from room temperature, 298 K, up to 598 K were measured using an in-house high temperature dielectric measurement system. This system consists of a high-precision LCR meter (Agilent 4284A), a temperature-controlled muffle furnace,

a high temperature sample holder, a thermocouple, a temperature reader, and a Windows server 2000 PC (see Figure 3-4).

Figure 3-3: Measurement of dielectric material at room temperature

As part of this system, a special sample holder was designed and constructed specifically for high temperature measurement (see Figure 3-5 below). The top right side of the ceramic pad was coated with silver to act as the bottom electrode. The clip on the left hand side was used to hold down the pellet samples and act as the top electrode. The clip was employed in a mechanism to accommodate samples of differing thicknesses, sizes and position of electrodes depending on the type of sample to be measured.

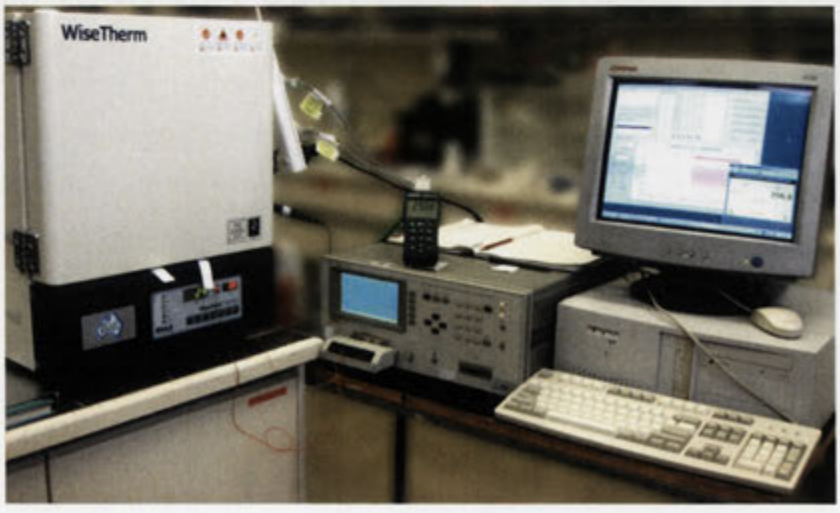

Figure 3-4: Measurement of dielectric material at high temperature

The electrodes used are required to have very low resistivity, an ability to maintain good electrical contact and must be stable over the measurement temperature range. A Beryllium copper alloy was chosen for the clip as it has high tensile yield strength. To ensure that a high quality electrical signal was maintained, gold wires were used to connect the two electrodes from the sample holder to the LCR meter. Gold wires were used as it is inert to oxidation over the temperature range investigated in this study.

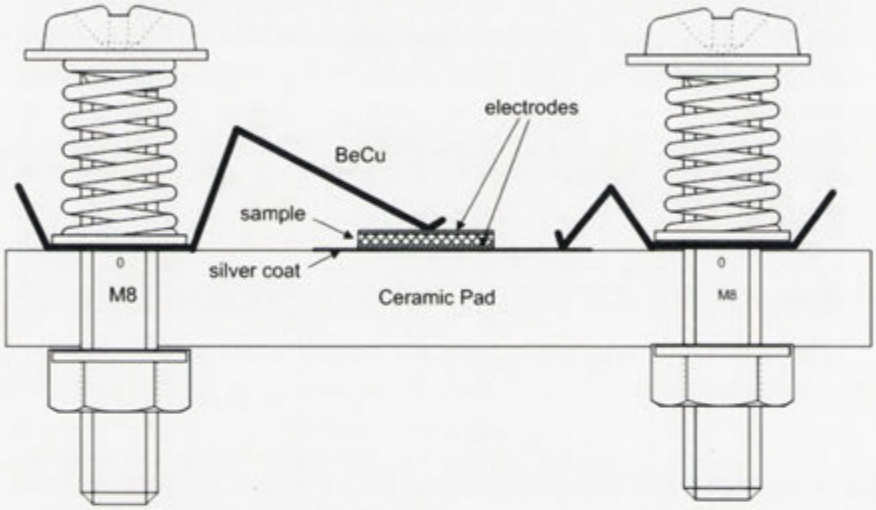

Figure 3-5 Sample holder for high temperature measurement

For these high temperature measurements, a K-type thermocouple was used as it gives good accuracy over the temperature range 123K to 1473K [57].

The sample holder shown in Figure 3-5 as well as the thermocouple probe were then inserted into the muffle furnace (Figure 3-4) which was programmed to give a slow and linear temperature rise. The gold wires from the sample holder were connected to the LCR meter. The thermocouple probe line was attached to a temperature reader. This data was sent to a temperature logger program in the PC via a serial port. The LCR meter was then connected to a PC by means of a GPIB cable. An in-house computer program was also written to support the measurement. This program recorded the dielectric properties of the sample automatically over a pre-set time interval. The program also draws the capacitance and dielectric loss as a function of temperature in real-time to allow close monitoring of the measurement (see section 3.3 below). The system takes 4 hours to reach 300 °C whereupon the sample in the furnace was allowed to cool slowly without any heating. Upon

completion of the measurement, the recorded temperature and dielectric properties were transferred to a Microsoft Excel spreadsheet for analysis.

3.2.3 Low Temperature Dielectric Measurement

Temperature-dependent dielectric constant and dielectric loss spectra of samples from the liquid nitrogen temperature of 77 K up to room temperature were collected using an in-house low temperature dielectric measurement system. This system consists of a high-precision LCR (Agilent 4284A) meter, a thermocouple, temperature reader, Windows server 2000 PC and a low temperature environmental box (Figure 3-6).

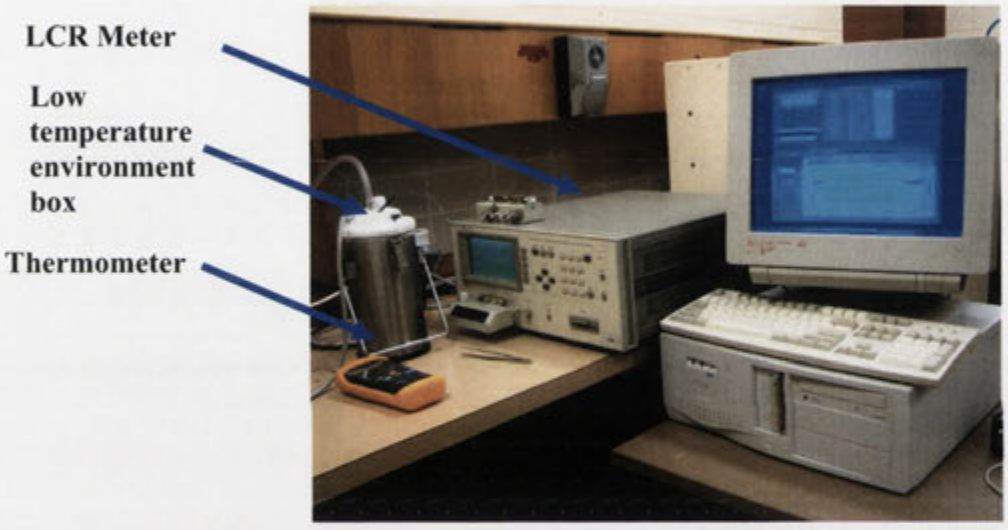

Figure 3-6 Low temperature dielectric measurement system

The most important part of the system is the low temperature environmental box. It was designed and constructed around the following requirements:

- It should be safe operating at temperatures as low as liquid nitrogen, 77K
- It should be a flexible design to hold samples with different type and shape
- It should be able to hold the sample at the same temperature long enough for the dielectric properties to be recorded. This is approximately 20 seconds
- The temperature rise should be linear and controllable
- To measure dielectric properties with high accuracy, ± 5 %
- To measure temperature to within ±1 %

- To minimise thermal contraction and expansion of the materials used
- It should be a sealed unit to prevent moisture affecting the measured dielectric properties
- There should be no background electromagnetic interference from heating
- The samples should be held in place with excellent electrical contact

The final design of the low temperature environmental box consists of a thermos flask as shown in Figure 3-6 that is filled with liquid nitrogen. A sample holding arm is attached to the lid such that when the lid is closed the sample is cooled to the liquid nitrogen temperature of 77K. A temperature probe is placed near the sample and connected to a thermometer. A type T probe was selected as it gives good accuracy over the temperature range from 73K to 623K [57].

The cores of the environmental box are the low temperature sample chamber and holder which are shown in Figure 3-7.

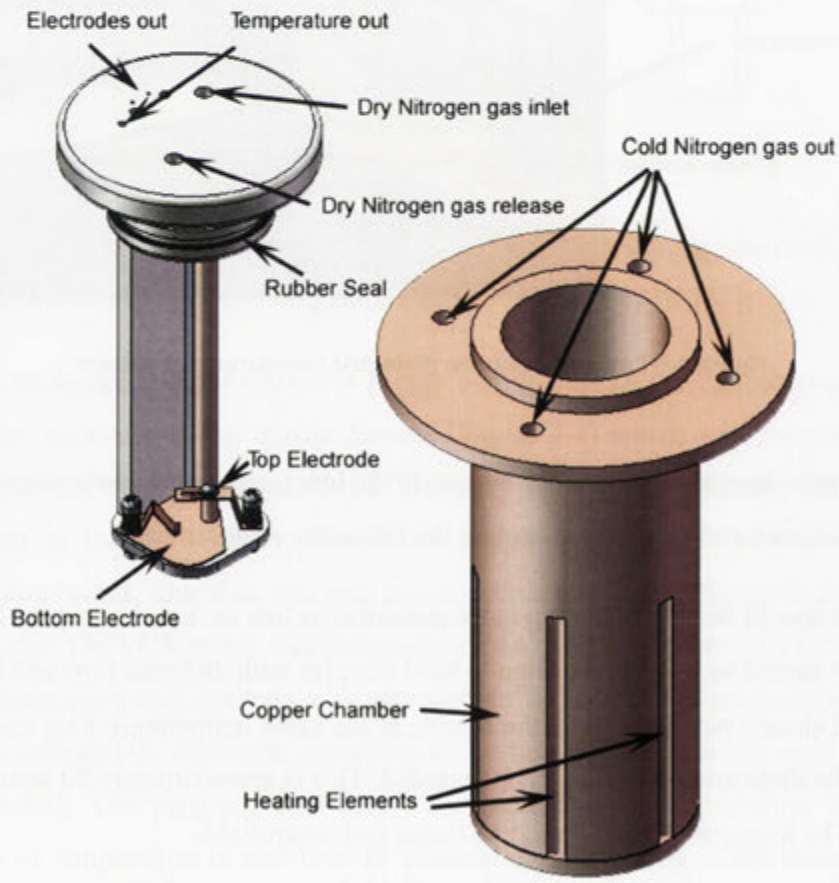

Figure 3-7 Low temperature sample holder and chamber

The sample holder component of the environmental box was designed similarly to the high temperature sample holder shown in Figure 3-5. This allows measurement of both bulk pellet as well as thin film samples.

Materials selection is a crucial part in the design of this low temperature environmental box. The material used to construct the core was copper due to its ready availability and high thermal conductivity. The chamber lid was made from Delrin (Polyoxymethylene, POM), a highly electrically resistant material with low thermal expansion. There are several different types of probes available with different metal compositions, enabling measurements over different temperature ranges.

The low temperature holder with an installed sample was first inserted into the sealed copper chamber. The chamber was then place into the thermos flask. Dry argon gas flow was then fed into the chamber to draw out moisture from the sample and chamber. Liquid nitrogen was slowly poured into the apparatus until the system reached a temperature near 77K, the boiling temperature of nitrogen. Once the system had cooled to liquid nitrogen temperature (which often took about 30 minutes), the measurement started and the temperature of the system was allowed to slowly increase. An in-house computer program (see section 3.3.2) was written to assist the measurement. The thermocouple and the PC were synchronised such that the temperature and dielectric properties measurements were logged simultaneously. It took the system around 10 hours to reach room temperature. Upon completion of the measurement, the recorded temperature and dielectric properties were transferred to a Microsoft Excel spreadsheet to analyse.

3.3 Dielectric Measurement Program

During the study, a computer program was developed to enable the dielectric measurement process. The communication with the LCR meter and the numerical calculation components of the program were written in C++, the graphical user interface (GUI) was built using Microsoft Visual Studio 2005. The program includes two parts: the room temperature dielectric measurement and the automated dielectric properties versus temperature measurement. Flowcharts describing the operation of the program are shown in Figure 3-8 and Figure 3-10 respectively.

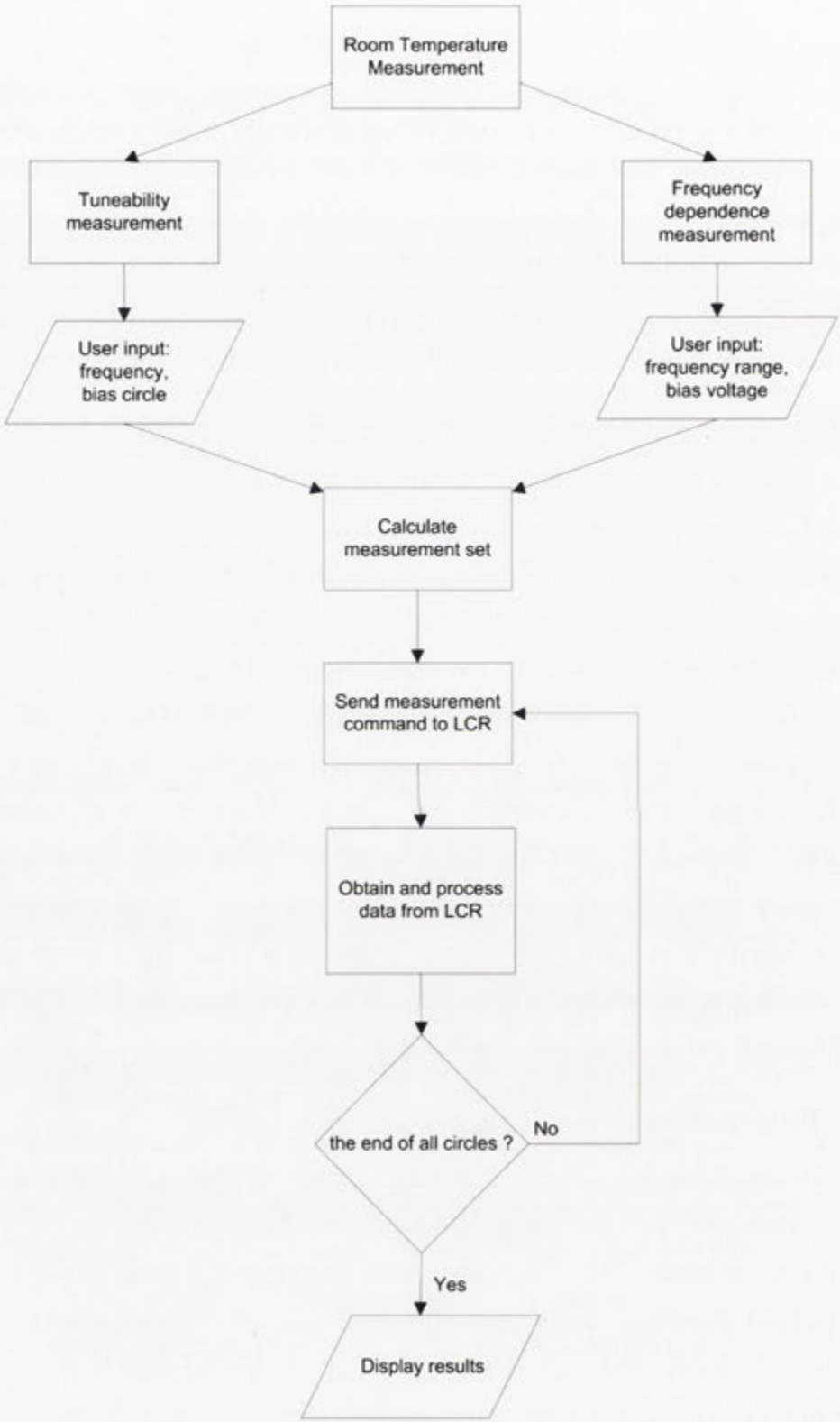

Figure 3-8 The operation of the dielectric measurement program for room temperature.

3.3.1 Program for Room Temperature Measurement

This part of the program helps the user to easily measure the dielectric properties of the samples including: capacitance, dielectric loss, impedance (in degrees or radians). A typical user interface with the program is shown in Figure 3-9.

The user can select either a specific frequency ("Choose a Frequency" module) or a pre-defined frequency range ("Which Frequency Range to Use" module). It is also possible to define a specific range and a certain number of points for measurement ("Define a Frequency Range" module). In this case, the program will automatically calculate a set of suitable intervals for each sub-range, so the obtained data curve is smooth.

The program also has a function to enable the user to measure the bias dependence of the dielectric properties *i.e.* to examine the tunability of the materials. In this case, the measurement can be performed with either bias variation direction, from negative to positive or reverse. The number of bias cycles is also changeable.

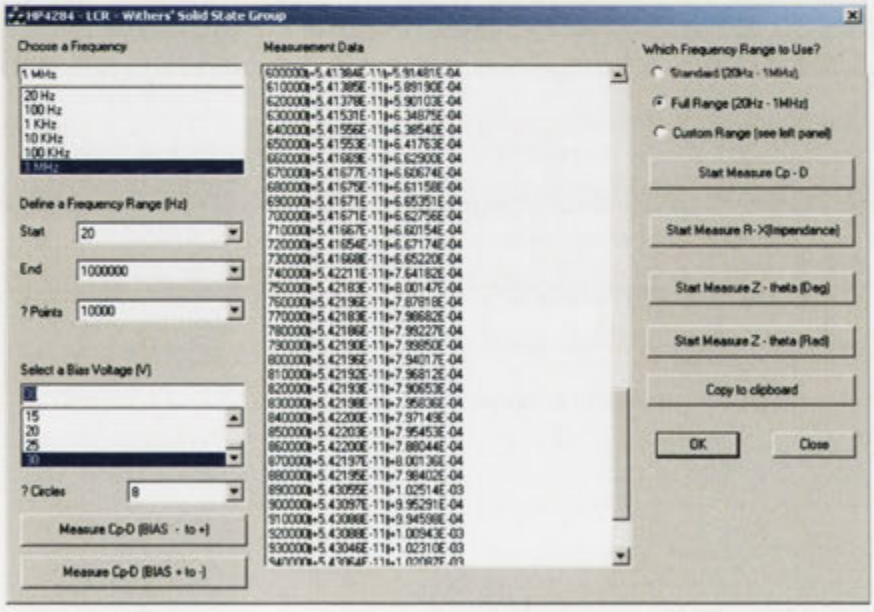

Figure 3-9 Interface of program for room temperature dielectric measurement

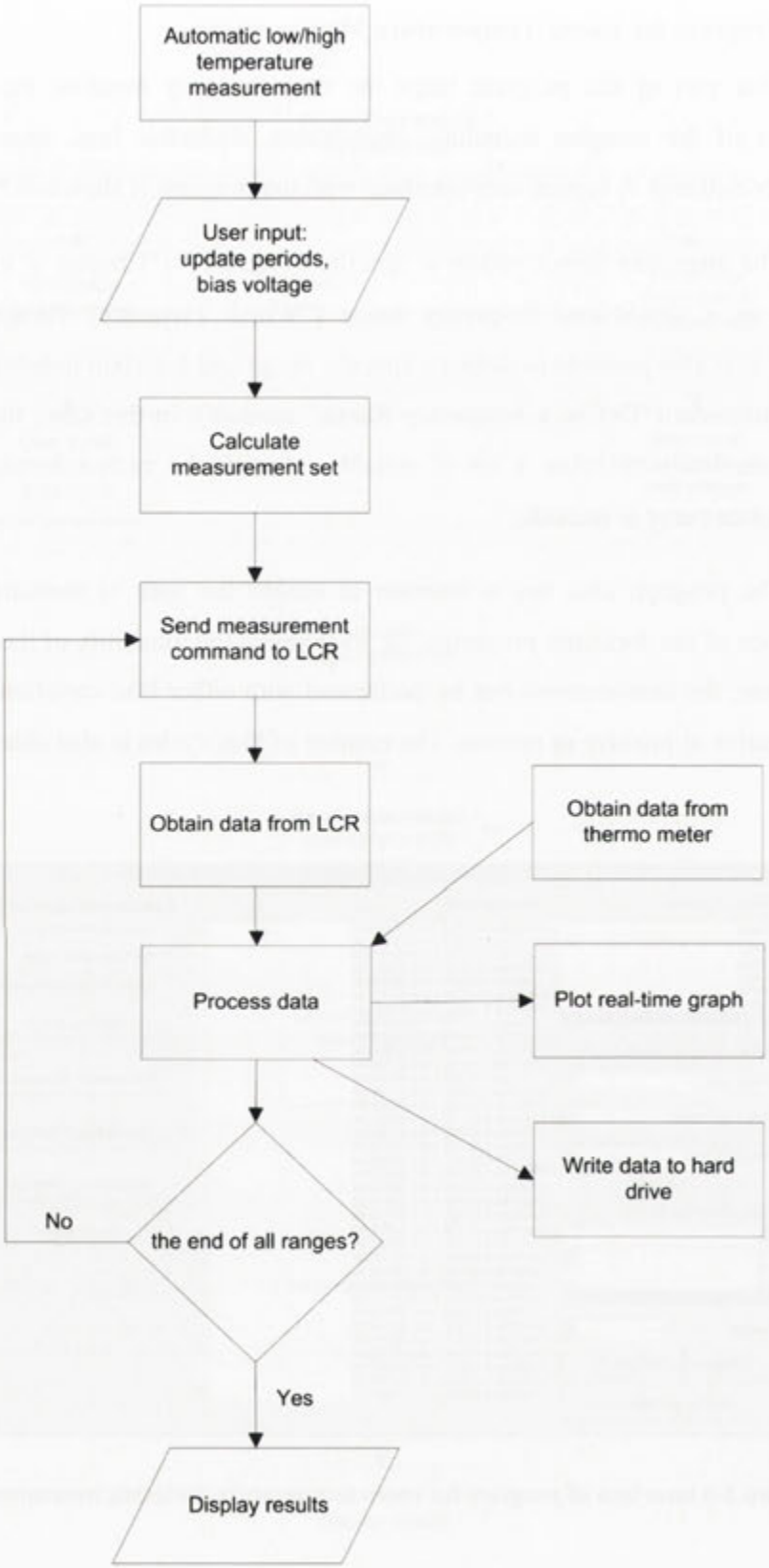

Figure 3-10 The operation of the dielectric measurement program for automatic low/high temperature measurement.

3.3.2 Program for Automatic Low – High Temperature Dielectric Measurement

This part of the program allows the user to automatically measure and record the dielectric properties of the samples over a preset time interval. This is particularly useful for both the low and high temperature dielectric measurement process as they often take a very long time. The program also draws the capacitance and dielectric loss in real-time to allow close monitoring of the progress of the measurement. Figure 3-11 shows a typical screenshot of the program in operation.

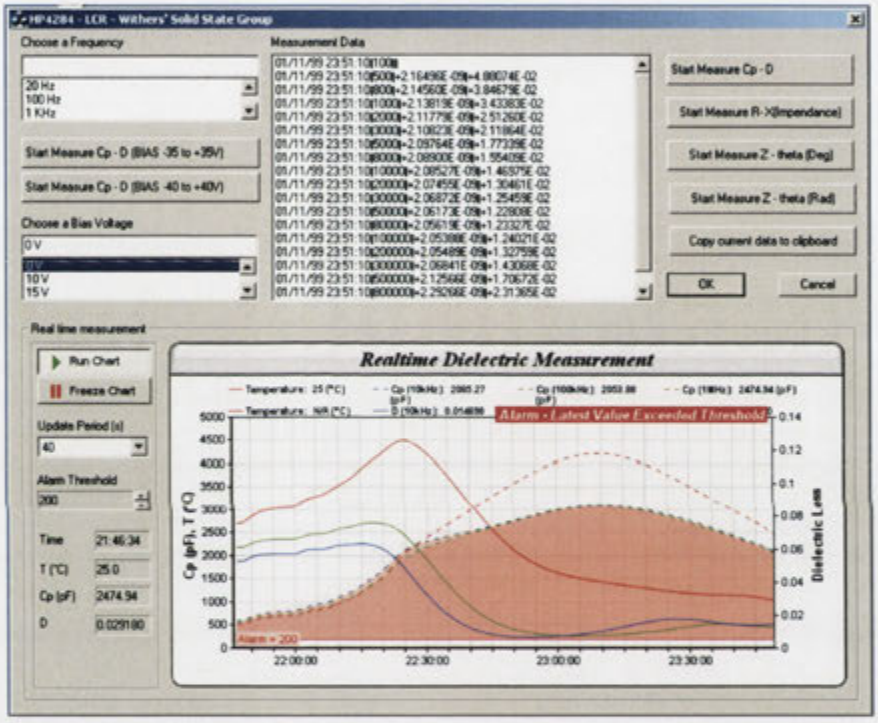

Figure 3-11 Interface of the program for automatic dielectric measurement

3.3.3 Remote Measurement Function

The automatic low/high temperature measurement process or the room temperature measurement process with more than a thousand points usually takes several hours to complete. It is therefore necessary to remotely monitor and control the measurement process.

To achieve this, a password protected, VNC based remote control server was setup on the measuring PC. The PC was then connected to the RSC network via an Ethernet cable such that a user with a VNC client *e.g.* Tight-VNC can access the measurement system remotely from their office or anywhere in the world. This also

allows transferral of the current measurement data from the measurement system to the user's PC remotely.

Chapter 4: The Non-stoichiometric Bismuth Based Pyrochlores, BMN and BNN

In this chapter, the synthesis, dielectric properties and average structure determinations of two 'misplaced displacive', Bi-based cubic pyrochlore phases found in the Bi_2O_3-$M^{II}O$-Nb_2O_5 ($M = Mg^{2+}$ and Ni^{2+}) systems is reported. In addition, the relationship between the local crystal chemistry and the inherent compositional and displacive disorder of these Bi-based cubic pyrochlore phases is investigated via electron diffraction and bond valence sum analysis.

4.1 Introduction

As discussed in the first chapter of this thesis, there has recently been much interest in the heavily disordered, Bi-based cubic pyrochlore phases found in a range of ternary Bi_2O_3-$M^{II}O$-Nb_2O_5 systems [16-21,58-60] due to their excellent dielectric properties (including electric field tuneability) and relatively low sintering temperatures [15,16,21,59-62]. The composition of these cubic pyrochlore phases was initially assumed to be fixed and of apparently ideal/'sensible' stoichiometry $Bi_2(M^{II}_{2/3}Nb^{V}_{4/3})O_7$ [21]. Recent careful phase analysis studies, however, have shown that the cubic pyrochlore phase in such systems is always a solid solution, almost invariably significantly Bi-deficient with respect to the above nominally ideal stoichiometries and requires the presence of nominally too small M^{2+} on the A sites as well as the B sites of the ideal $A_2B_2O_7$ (or $B_2O_6{\bullet}O'A_2$) pyrochlore structure type (see Figure 1-1) [20,28,63]. This has led to their designation as so-called "misplaced-displacive" cubic pyrochlores [20].

The most commonly studied bismuth-based cubic pyrochlore phase of this type is $(Bi_{1.5}Zn_{0.5-\delta})(Zn_{0.5}Nb_{1.5})O_{7-\delta}$ (BZN) [15-18,20,58,59,62]. Its relatively high dielectric constant, low dielectric loss as well as compositionally tuneable temperature coefficient of capacitance (when used in conjunction with a nearby monoclinic zirconolite like $Bi_2(Zn^{II}_{2/3}Nb^{V}_{4/3})O_7$ ternary phase within the Bi_2O_3-$Zn^{II}O$-Nb_2O_5 system [17,20,59,62,63]) makes this material very attractive for low temperature firing, high frequency multi-layer device applications [15,16,21,59,62]. Average structure refinements of BZN [17-19] and a few other related $(Bi_{1.5}M^{II}_{0.5-\delta})(M^{II}_{0.5}Nb_{1.5})O_{7-\delta}$ Bi-based pyrochlore phases [28,68,80] to date have all reported considerable displacive disorder, particularly associated with the $O'A_2$ sub-structure. Despite considerable recent efforts, however, the local crystal chemistry underlying such behaviour still remains far from well understood nor its relationship to the dielectric properties of these phases [17,18,39,64]. The apparently inherent displacive disorder of these Bi-based pyrochlore phases is important to understand both from the fundamental crystal chemical point of view but also because it has been linked to anomalous low temperature, glass-like dielectric relaxation behaviour in these systems which has the potential to rule out their use in the commercially important RF/microwave frequency range [21,60,65,66].

Golovshchikova *et al.* [22] were the first to report the existence of cubic pyrochlore phases in the Bi_2O_3-$M^{II}O$-Nb_2O_5 (M = Ni and Mg) systems (labelled the BNN and BMN phases in what follows) of apparent stoichiometry $Bi_2(M^{II}_{2/3}Nb^{V}_{4/3})O_7$, ($M$ = Ni and Mg). More recently, Cann *et al.* [21] reported the synthesis and dielectric properties of further $Bi_2(M^{II}_{2/3}Nb^{V}_{4/3})O_7$ cubic pyrochlore phases, including the BNN and BMN cubic pyrochlore phases. Later still, Sirotinkin and Bush [58] reported the existence and dielectric properties of cubic pyrochlore phases in the Bi_2O_3-$M^{II}O$-Nb_2O_5 (M = Zn, Ni, Mg, Cu and Mn) systems, but this time of stoichiometry $(Bi_{1.5}M^{II}_{0.5-\delta})(M^{II}_{0.5}Nb_{1.5})O_{7-\delta}$, a composition rather closer to that of the BZN cubic pyrochlore. Finally, Valant and Suvorov [67] carried out a phase analysis investigation of the ternary Bi_2O_3-NiO-Nb_2O_5 system. They report the existence of a quite compact field of non-stoichiometric cubic pyrochlore solid solution with a composition centred around $Bi_{1.5}Ni_{0.67}Nb_{1.33}O_{6.25}$ (or $Bi_{1.68}Ni_{0.75}Nb_{1.49}O_7$ if normalised to seven oxygens) rather than the $Bi_2(Ni_{2/3}Nb_{4/3})O_7$ composition assumed by Cann *et al.* [21] or the $(Bi_{1.5}M^{II}_{0.5-\delta})(M^{II}_{0.5}Nb_{1.5})O_{7-\delta}$ composition reported by Sirotinkin and Bush [58]. The above results are clearly not in agreement as regards either the stoichiometry or the dielectric properties for both the M = Ni and Mg compounds. In the case of the M = Ni phase, for example, Cann *et al.* [21] report a room temperature dielectric constant for $Bi_2(Ni^{II}_{2/3}Nb^{V}_{4/3})O_7$ of 122 (at 1 MHz) while Sirotinkin and Bush report a dielectric constant for $(Bi_{1.5}M^{II}_{0.5-\delta})(M^{II}_{0.5}Nb_{1.5})O_{7-\delta}$ of only ~ 27 (at 10 kHz) [58].

The aim of this chapter therefore was to re-investigate the synthesis, composition and dielectric properties characteristic of the BNN and BMN, Bi-based cubic pyrochlore phases found in the Bi_2O_3-$M^{II}O$-Nb_2O_5 (M = Mg^{2+} and Ni^{2+}) systems with a view to resolving the above contradictions. In addition, the relationship between the local crystal chemistry of these cubic pyrochlore phases and inherent displacive disorder is also investigated as is the low temperature dielectric relaxation behaviour of BNN and BMN.

4.2 Sample Preparation

Samples were prepared via the solid state route using high purity Bi_2O_3 (99.995 %, Koch-Light), Nb_2O_5 (99.9+ %, Alfa), MgO (98%, AnalaR), NiO (99.99 %, Sigma - Aldrich) as starting materials. The initial syntheses assumed a nominal ideal composition for the cubic pyrochlore phase of $(Bi_{1.5}M^{2+}_{0.5})(M^{2+}_{0.5}Nb^{5+}_{1.5})O_7$ (M = Mg and Ni), as assumed by Sirotinkin and Bush [58]. Pelleted samples were prepared as described in Section 2.2.1 above. They were typically sintered at a highest temperature of 1050 °C for 1 to 3 days. The resultant pellets were smooth with no sign of additional phases on the surfaces. In agreement with the recently reported phase diagram of Valant and Suvorov [67], it was found that the nominally '$Bi_{1.5}MNb_{1.5}O_7$' specimens thereby obtained, whilst containing a dominant cubic pyrochlore phase, were nonetheless clearly not single phase samples. In the case of the M = Ni system, the other phases identified were $NiNb_2O_6$ and NiO, again in agreement with the phase diagram of Valant and Suvorov [67].

New samples were therefore synthesised at a nominal composition of $Bi_{1.67}M_{0.75}Nb_{1.5}O_7$, corresponding to the centre of the cubic pyrochlore solid solution field reported for the Bi_2O_3-NiO-Nb_2O_5 system by Valant and Suvorov [67] when normalised to seven oxygens. A final annealing temperature of 1150 °C for 7 days was used in the case of the M = Mg, nominally $Bi_{1.67}Mg_{0.75}Nb_{1.5}O_7$ (BMN) sample and 1100 °C for 3 days in the case of the M = Ni, $Bi_{1.67}Ni_{0.75}Nb_{1.5}O_7$ (BNN) sample.

4.3 Results and Discussion

4.3.1 X-ray Powder Diffraction Results

The purity of the BMN and BNN samples were first investigated by X-ray powder diffraction using a Guinier-Hägg camera and Cu $K_{\alpha 1}$ radiation. Both resultant samples appeared single phase using standard two hour Guinier XRD film exposures. Careful examination of obtained XRD films exposed for a rather longer period (4 hours) confirmed that the BNN sample was indeed single phase while the BMN sample was found to contain a (barely detectable) trace amount of an unknown second phase. In this latter case, four very weak additional lines were observed which could not be indexed to the BMN cubic pyrochlore phase (see the peaks

labelled with * in Figure 4-1). These additional lines were not visible on the XRD film when using a standard exposure length of 2 hours.

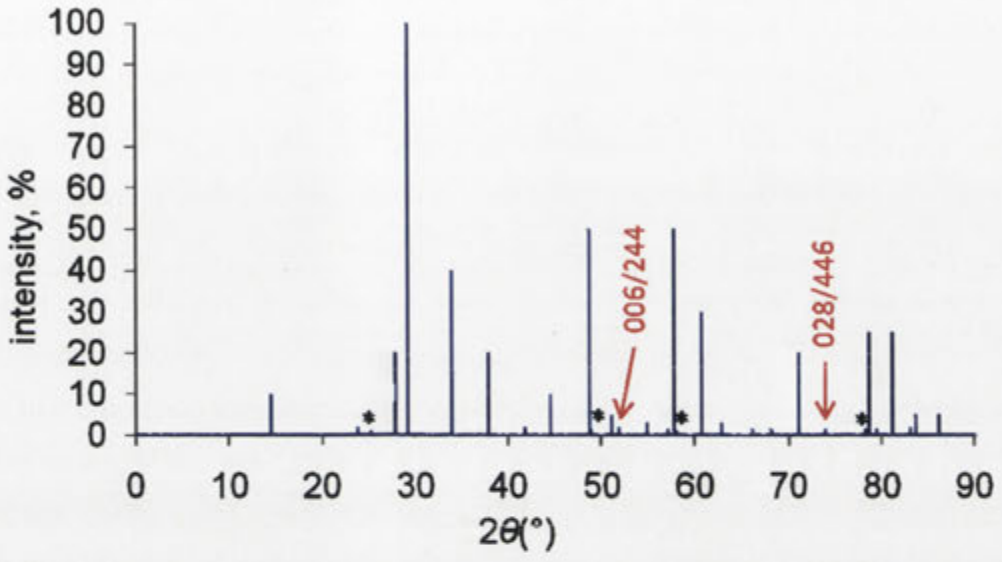

Figure 4-1 X-ray diffraction pattern of the BMN sample drawn from measured Guinier films and estimated intensities taken from Table 4-1.

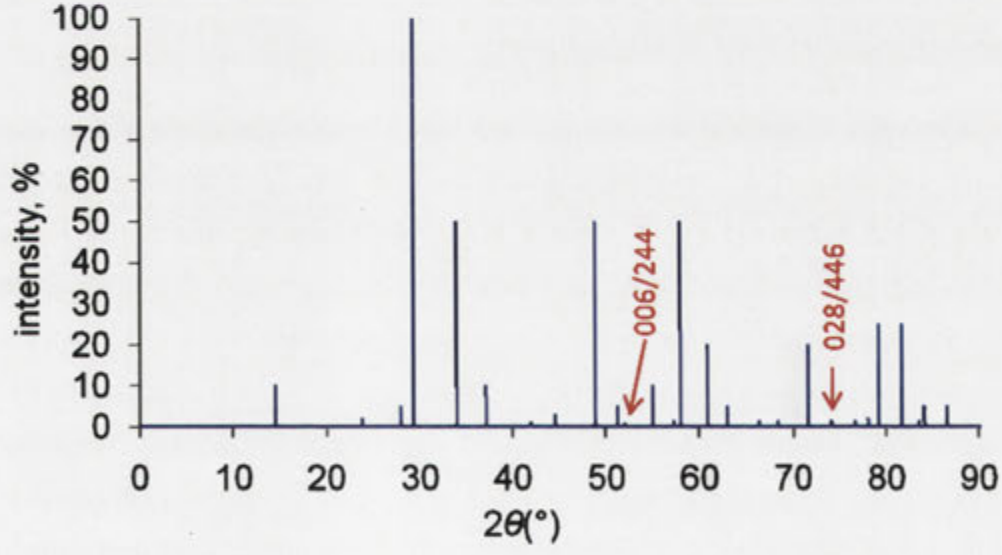

Figure 4-2 X-ray diffraction pattern of the BNN sample drawn from measured Guinier films and estimated intensities taken from Table 4-1.

The average structures of these BMN and BNN cubic pyrochlore phases were indexed using an *F*-centered cubic unit cell. High purity Si powder (Lot GD#1, [34]) was added as an internal standard for accurate determination of the unit cell parameters, refined using the program "Unitcell" [20]. The cubic unit cell parameters were thereby refined to values of a = 10.5607(5) Å and a = 10.5354(2) Å for BMN and BNN respectively. Two very weak lines (442/006 and 446/028), forbidden for the ideal $Fd\bar{3}m$ cubic pyrochlore structure type and indicative of inherent, large amplitude, displacive disorder in the O'A_2 sub-structure (as first pointed out by Birchall and Sleight [31] and subsequently by other authors [17,20,28,32,33]), were observed in both cases (see Figure 4-1, Figure 4-2 and Table 4-1. Note that Figure 4-1 and Figure 4-2 are drawn from measured Guinier films and estimated intensities taken from Table 4-1). While the quantitative EPMA determined composition of the BNN sample (see below) is very similar to that reported by Valant and Suvorov [67], the refined lattice parameter for our BNN cubic pyrochlore phase differs slightly from the value of 10.5459(4) Å reported for the same composition in [67]. In the case of the BMN cubic pyrochlore phase, the refined lattice parameter of 10.5607(4) Å is quite close to that reported by Sirotinkin and Bush [58] for their nominally $Bi_{1.5}MgNb_{1.5}O_7$, BMN phase of a = 10.570(2) Å.

4.3.2 Electron Probe Microanalysis

In order to confirm the nominal $Bi_{1.67}M_{0.75}Nb_{1.5}O_7$ composition and to check for homogeneity of the samples, the samples were also investigated via electron probe micro analysis (EPMA), using a JEOL 6400 scanning electron microscope (SEM) equipped with an Oxford Instruments light element EDS detector and Link ISIS SEMquant software. Multiple spot analyses were carried out at 15 kV and 1 nA using $BiNbO_4$ and either MgO (for BMN) or NiO (for BNN) as standards. The BNN sample was found to be homogeneous and single phase of average composition $Bi_{1.65(2)}Ni_{0.75(3)}Nb_{1.50(1)}O_7$ (arbitrarily normalised to seven oxygens) *i.e.* in agreement with the nominal starting stoichiometry within error. The quoted error bars represent the standard deviation of the 40 separate spot analyses used to obtain the quoted average composition.

Table 4-1: X-ray powder diffraction data for $Bi_{1.67}Mg_{0.70}Nb_{1.52}O_7$ (BMN, space group $Fd\bar{3}m$, #227, a = 10.5653(4) Å) and $Bi_{1.67}Ni_{0.75}Nb_{1.5}O_7$ (BNN) (space group $Fd\bar{3}m$, #227, a = 10.5354(5) Å).

hkl	BMN				BNN				Note
	Visible	$\Delta 2\theta$	d_{obs}	I_{obs}	Visible	$\Delta 2\theta$	d_{obs}	I_{obs}	
111	x	0.071	6.068	10	x	0.026	6.072	10	
022	x	0.011	3.732	3	x	-0.006	3.726	<1	
113	x	-0.002	3.184	20	x	0.011	3.175	5	
222	x	-0.009	3.050	100	x	0.004	3.041	100	
004	x	-0.004	2.641	40	x	0.012	2.633	50	
133	x	-0.003	2.423	20	x	0.008	2.417	10	
224	x	-0.006	2.156	1	x	0.007	2.150	<1	
115, 333	x	-0.009	2.033	10	x	-0.002	2.028	3	
044	x	-0.002	1.867	50	x	-0.001	1.863	50	
135	x	-0.003	1.785	5	x	0.009	1.781	5	
006, 244	x	0.002	1.760	1	x	-0.01	1.756	1	*
026	x	0.006	1.670	3	x	0.005	1.666	10	
335	x	0.006	1.610	<1	x	0.009	1.606	<1	
226	x	-0.006	1.592	50	x	-0.001	1.588	50	
444	x	0.012	1.524	30	x	0.002	1.521	20	
117, 155	x	0.007	1.479	3	x	0.004	1.475	5	
246	x	0.001	1.411	<1	x	-0.004	1.408	<1	
137, 355	x	0.003	1.375	<1	x	-0.007	1.372	1	
008	x	0.000	1.320	20	x	0.004	1.317	20	
028, 446	x	0.005	1.281	<1	x	-0.004	1.278	<1	*
066, 228					x	-0.002	1.242	1	
157, 555	x	0.002	1.219	1	x	0	1.217	<1	
266	x	0.000	1.211	25	x	-0.004	1.209	25	
048	x	-0.009	1.181	25	x	0.003	1.178	25	
119, 357	x	-0.007	1.159	1	x	-0.003	1.156	<1	
248	x	-0.001	1.152	5	x	-0.011	1.150	5	
466	x	-0.006	1.126	5	x	-0.002	1.123	5	

Note: * Denotes lines forbidden for the ideal $Fd\bar{3}m$ cubic pyrochlore structure type and diagnostic of inherent displacive disorder.

In the case of the initial BMN sample, the trace amount of the second phase which caused the weak additional lines in the highly exposed Guinier XRD films was not observed in the SEM or via EPMA. The composition of the cubic pyrochlore phase as determined by quantitative EPMA was $Bi_{1.67(3)}Mg_{0.64(2)}Nb_{1.53(1)}O_7$ (arbitrarily normalised to seven oxygens) *i.e.* somewhat Mg-deficient relative to the as-synthesised composition. Later, this Mg-deficiency was found to be due to insufficient initial drying of the MgO starting powder prior to weighing. The MgO after drying at 120 °C overnight still contained hydrated water (around 16 %). This hydrated water content was only eliminated after heating MgO at a temperature higher than 800 °C. Re-synthesis at a slightly more Mg-rich composition than the above was subsequently found to give a pure single phase cubic BMN sample of average composition $Bi_{1.66(1)}Mg_{0.70(3)}Nb_{1.52(1)}O_7$. The refined cubic unit cell parameter for this BMN sample was a = 10.5653(4) Å (see Table 4-1 above).

4.3.3 Average Structure Refinements

The presence of the nominally forbidden diagnostic 006/442 and 028/446 reflections in laboratory XRD data (see Table 4-1 above) [18,28,63] suggests significant displacive disorder in the O'A_2 sub-structure, as mentioned above. Room temperature (298 K) neutron powder diffraction data of both the BMN and BNN samples were therefore collected on the High Resolution Powder Diffractometer (HRPD) at the High Flux Australian Reactor (HIFAR) at a wavelength of ~1.49 Å [41] and the average structures refined. The Rietica for Windows software package [43] was used for Rietveld structure analysis. Data below 8° and above 150° in 2θ were treated as excluded regions. The unit cell values obtained for the BMN and BNN samples via XRD were used as "standards" to refine the neutron beam wavelength to $\lambda_{neutron}$ = 1.4913(2) Å (given as ~ 1.49 Å) which was then fixed.

The structural parameters refined were atomic coordinates and atomic displacement parameters (ADP's), both isotropic and anisotropic. The site occupancies for the heavy metal atoms were constrained to be consistent with the results of the EPMA analyses given above. The EPMA investigation, however, does not allow the oxygen content of the samples to be determined. We thus attempted to use the neutron refinement to get an estimate of any vacancies in the oxygen positions. Only the O' position gave a value which differed from unity, thus this was

the only position that was allowed to vary in the final refinement. As can be seen in Table 4-4 and Table 4-5, the differences between the expected O' occupancy values (left) and the refined ones (right) are the same to within one standard deviation. The fractional co-ordinates and ADP's for both ions located on the ideal pyrochlore *A*-sites (Bi^{3+} and Mg^{2+} or Ni^{2+}) as well as for those on the *B*-sites (Mg^{2+} or Ni^{2+} and Nb^{5+}) were always constrained to be equal. The obtained refinement results are detailed in Table 4-4 for BMN and Table 4-5 for BNN respectively.

The $A_2B_2O_7$, or $B_2O_6{\bullet}O'A_2$, ideal pyrochlore structure type (see Figure 1-1 and Figure 1-2) has the *A* cations on 16*d* at $^1/_2,^1/_2,^1/_2$, the *B* cations on 16*c* at 000, the O oxygen on 48*f* at $x,^1/_8,^1/_8$ and the O' oxygens on 8*b* at $^3/_8,^3/_8,^3/_8$ (origin setting 2, $Fd\bar{3}m$). An initial test refinement of the BNN sample assuming a re-normalised $Bi_{1.667}Ni_{0.75}Nb_{1.5}O_7$ stoichiometry similar to that reported in [67] of $Bi_{1.48}(Ni_{2/3}Nb_{4/3})O_{6.22}$ or $O'_{0.22}Bi_{1.48}{\bullet}(Ni_{2/3}Nb_{4/3}O_6)$ (with Ni only on the pyrochlore *B* sites and the O' site occupied at a very low level) quickly blew up with strongly negative ADP's on the O' site *etc.* It was clear that Ni must occupy both the pyrochlore *A* and *B* sites while the occupancy of the O' site must be close to one. The same was true for the BMN sample. Subsequent refinements thus assumed $(Bi_{0.833}Mg_{0.11}\square_{0.06})_2(Mg_{0.24}Nb_{0.76})_2O_7$ and $(Bi_{0.833}Ni_{0.125}\square 0.04)_2(Ni_{0.25}Nb_{0.75})_2O_7$ (□ denotes a vacancy) starting compositions *i.e.* no oxygen vacancies and full occupancy of the metal ion *B* sites.

The initial refinements (model 1; see the first lines of Table 4-4 for BMN and Table 4-5 for BNN and Table 4-2 for the associated refinement statistics) assumed the ideal pyrochlore structure type and isotropic ADPs. The one unknown fractional co-ordinate, the *x* fractional co-ordinate of the 48*f* oxygen ions, then refined to the same value of 0.3194(2) for both BMN and BNN. The relative magnitudes of the refined isotropic U_{iso}'s for this model 1 were quite comparable with those refined using the same model for the other Bi-based pyrochlores whose structures have been refined to date (*cf. e.g.* with Table 1 of [17] and [18] and the Model 1 columns of Table 3 of [28] and [68]). In particular, the refined U_{iso}'s for the *B* cation and the O oxygen making up the B_2O_6 sub-structure are relatively normal while those for the *A* cation and the O' oxygen constituting the $O'A_2$ sub-structure are ~ 5-10 times larger

and clearly abnormal, requiring substantial displacive disorder associated with the O'A_2 sub-structure.

Table 4-2 The refinement statistics of model 1.

	R_p	R_{wp}	χ^2	D-W
BMN	0.0728	0.0925	2.878	0.578, 0.785
BNN	0.0708	0.0910	2.868	0.527, 0.768

The introduction of anisotropic ADPs (Model 2, the second lines in Table 4-4 and Table 4-5), in particular on the Bi/M^{2+}, or A, site, lead to a significant improvement in the associated refinement statistics (see Table 4-3). The principal components of the mean square displacement ellipsoid of the A site ions along and perpendicular to the local O'-A-O' direction refined to values given by $U_{11} + 2U_{12}$ = 0.0127 Å^2 / 0.0139 Å^2 and $U_{11} - U_{12}$ = 0.1483 Å^2 / 0.1636 Å^2 for BMN/BNN respectively *i.e.* to a very flat, or pancake-shaped, ellipsoid (see Figure 4-3 below). Clearly, as has also been found for BZN [17,18,19] and the other Bi-pyrochlores whose structures have been refined to date [19,20,28,68], the disordered A cation displacements are constrained to displace in {111} planes perpendicular to the local O'-A-O' axis (by ~ 0.385 Å/ ~ 0.405 Å in this case).

Table 4-3 The refinement statistics of model 2.

	R_p	R_{wp}	χ^2	D-W
BMN	0.0598	0.0728	1.805	1.027, 1.209
BNN	0.0578	0.0702	1.709	0.971, 1.243

Table 4-4 Structural parameters for BMN refined using the four models as described in the text. The first line for each atom is Model 1, the second line is for Model 2, the third line is for Model 3 and the fourth line is the final Model 4 (in bold). The cubic unit cell parameter was a = 10.5662(2) Å and the space group $Fd\bar{3}m$ (origin choice 2). The anisotropic ADPs are given below the atom coordinates, the refinement statistics are in the text.

Atom	Site	x	y	z	U_{iso}*100	Occ. (%)
Bi/Mg2	16*d*	1/2	1/2	1/2	0.1004(15)	83.3(3)/11.0(2)
	16*d*	1/2	1/2	1/2	*a	83.3(3)/11.0(2)
	96*g*	1/2	0.4722(2)	0.5278(2)	0.0180(11)	83.3(3)/11.0(2)
	96*g*	**1/2**	**0.4727(9)**	**0.5273(9)**	***b**	83.3(3)/11.0(2)
Nb/Mg1	16*c*	0	0	0	0.0118(4)	76.0(1)/24.0(2)
	16*c*	0	0	0	*c	76.0(1)/24.0(2)
	16*c*	0	0	0	0.0116(4)	76.0(1)/24.0(2)
	16*c*	**0**	**0**	**0**	***d**	**76.0(1)/24.0(2)**
O	48*f*	0.3194(2)	1/8	1/8	0.0223(4)	100
	48*f*	0.3201(1)	1/8	1/8	*e	100
	48*f*	0.3193(1)	1/8	1/8	0.0192(3)	100
	48*f*	**0.3198(1)**	**1/8**	**1/8**	***f**	**100**
O'	8*b*	3/8	3/8	3/8	0.095(3)	100
	8*b*	3/8	3/8	3/8	*g	100
	32*e*	0.3548(6)	0.3548(6)	0.3548(6)	0.041(4)	100
	32*e*	**0.3559(11)**	**0.3559(11)**	**0.3559(11)**	***h**	**99/97(2)**
Atom	**U_{11}**	**U_{22}**	**U_{33}**	**U_{12}**	**U_{13}**	**U_{23}**
*a	0.1031(14)	0.1031(14)	0.1031(14)	-0.0452(14)	-0.0452(14)	-0.0452(14)
***b**	**0.025(9)**	**0.025(9)**	**0.018(6)**	**-0.012(11)**	**0.0039(23)**	**0.0039(23)**
*c	0.0168(4)	0.0168(4)	0.0168(4)	-0.00037(5)	-0.00037(5)	-0.00037(5)
***d**	**0.0124(4)**	**0.0124(4)**	**0.0124(4)**	**-0.0031(5)**	**-0.0031(5)**	**-0.0031(5)**
*e	0.0316(8)	0.0165(4)	0.0165(4)	0	0	0.0119(6)
***f**	**0.0281(8)**	**0.0166(4)**	**0.0166(4)**	**0**	**0**	**0.0090(6)**
*g	0.1143(30)	0.1143(30)	0.1143(30)	0	0	0
***h**	**0.062(7)**	**0.062(7)**	**0.062(7)**	**-0.004(3)**	**-0.004(3)**	**-0.004(3)**

Table 4-5 Structural parameters from BNN refined with four models given in the text. First line is Model 1, second Model 2, third Model 3 and fourth the final Model 4 (in bold). The unit cell parameter was a = 10.5427(2) Å and the space group $Fd\bar{3}m$ (origin choice 2). The anisotropic ADPs are given below the atom coordinates, the refinement statistics are in the text.

Atom	Site	x	y	z	U_{iso}*100	Occ. (%)
Bi/Ni2	16*d*	1/2	1/2	1/2	0.1086(15)	83.3(1)/12.5(3)
	16*d*	1/2	1/2	1/2	*a	83.3(1)/12.5(3)
	96*g*	1/2	0.4713(2)	0.5287(2)	0.0232(11)	83.3(1)/12.5(3)
	96*g*	**1/2**	**0.4716(9)**	**0.5284(9)**	***b**	83.3(1)/12.5(3)
Nb/Ni1	16*c*	0	0	0	0.0114(4)	75.0(1)/25.0(3)
	16*c*	0	0	0	*c	75.0(1)/25.0(3)
	16*c*	0	0	0	0.0096(3)	75.0(1)/25.0(3)
	16*c*	**0**	**0**	**0**	***d**	75.0(1)/25.0(3)
O	48*f*	0.3194(2)	1/8	1/8	0.0212(4)	100
	48*f*	0.3202(1)	1/8	1/8	*e	100
	48*f*	0.3194(1)	1/8	1/8	0.0178(3)	100
	48*f*	**0.3199(1)**	**1/8**	**1/8**	***f**	**100**
O'	8*b*	3/8	3/8	3/8	0.1030(31)	100
	8*b*	3/8	3/8	3/8	*g	100
	32*e*	0.3535(5)	0.3535(5)	0.3535(5)	0.0421(36)	100
	32*e*	**0.3548(11)**	**0.3548(11)**	**0.3548(11)**	***h**	**0.975/0.99(2)**
Atom	**U_{11}**	**U_{22}**	**U_{33}**	**U_{12}**	**U_{13}**	**U_{23}**
*a	0.1137(15)	0.1137(15)	0.1137(15)	-0.0499(11)	-0.0499(11)	-0.0499(11)
***b**	**0.024(8)**	**0.024(8)**	**0.024(8)**	**-0.015(11)**	**0.001(2)**	**0.001(2)**
*c	0.0143(3)	0.0143(3)	0.0143(3)	-0.0021(4)	-0.0021(4)	-0.0021(4)
***d**	**0.0109(3)**	**0.0109(3)**	**0.0109(3)**	**-0.0021(4)**	**-0.0021(4)**	**-0.0021(4)**
*e	0.0299(8)	0.0147(4)	0.0147(4)	0	0	0.0111(5)
***f**	**0.0263(8)**	**0.0151(4)**	**0.0151(4)**	**0**	**0**	**0.0084(6)**
*g	0.1225(32)	0.1225(32)	0.1225(32)	0	0	0
***h**	**0.067(7)**	**0.067(7)**	**0.067(7)**	**-0.004(3)**	**-0.004(3)**	**-0.004(3)**

The next stage of the refinement was to introduce displacive disorder on both the *A* and O' sites in order to significantly reduce the isotropic ADP's of the model 1 refinement and in line with earlier structural studies of other Bi-pyrochlores [18,20, 80]. The *A*-site ions were thus displaced from Wyckoff position 16*d* ($^1/_2$, $^1/_2$, $^1/_2$) to 96*h* ($^1/_2$, $^1/_2$-ε_A, $^1/_2$+ε_A) while the O' ion was shifted from position 8*b* ($^3/_8$,$^3/_8$, $^3/_8$) to Wyckoff position 32*e* ($^3/_8$+ε_O', $^3/_8$+ε_O', $^3/_8$+ε_O'). The refined displacement magnitudes off the 16*d* and 8*b* sites for the *A* and O' sites were then 0.415 Å/0.428 Å and 0.370 Å/0.393 Å for BMN/BNN respectively. This model (Model 3, the third lines in Table 4-4 and Table 4-5 significantly reduced the originally refined isotropic ADP's on both the *A* and O' sites (although that on the O' site still remains rather too high suggesting that the disorder on the O' site is not particularly well-modelled by the splitting employed) while the refinement statistics again improved significantly (see Table 4-6). (It is worth noting that the refinement statistics remain virtually identical if the sign of ε_O' is reversed).

Table 4-6 The refinement statistics of model 3.

	R_p	R_{wp}	χ^2	D-W
BMN	0.0606	0.0726	1.775	1.098, 1.231
BNN	0.0578	0.0697	1.683	1.052, 1.262

The final refinements (Model 4, line 4 of Table 4-4 and Table 4-5), see also Figure 4-3(a) and (b) kept the displacive disorder on both the A and O' sites outlined in Model 3 but allowed anisotropic ADPs for all atoms. This introduced an additional seven parameters but lead to a significant further final improvement in refinement statistics (see Table 4-7) compared to Model 3. Note that the refined anisotropic displacement ellipsoid for the already displaced *A* site ions again takes a flat pancake shape so that the six 96*h* *A* site ions virtually overlap to form a donut shape perpendicular to the local O'-*A*-O' axis (see Figure 4-3).

At this last stage of the refinement, the initial assumption that there were no oxygen vacancies and that the metal ion vacancies would be located exclusively on the *A* site positions were tested by allowing the oxygen occupancies to vary without constraints and by refining the relative occupancies of the Mg/Ni ions on the *A* and *B*

sites. The oxygen occupancies were refined first. The occupancy of the O site refined to 1.000(4) while that on the O' site refined to 0.97(2) for BMN and to 1.000(3) and 0.99(2) respectively for BNN *i.e.* to within error there is no evidence for oxygen vacancies on either the O or O' sites. The relative *M* occupancies on the *A* and *B* sites were refined next but again changed very little (and in the unphysical direction of having more than 1 metal ion on the pyrochlore *B* site) as did the refinement statistics *e.g.* for BMN, the Mg occupancy on the *A* site refined to 0.10(1) (equivalent within error to the initially assumed 0.11(2)) while the Mg occupancy on the *B* site refined to 0.25(2) (again equivalent to within error to the initially assumed 0.24(1)). Clearly the vacancies on the metal atom sites are overwhelmingly if not entirely located on the *A* sites. There was thus no evidence for any need to change the assumptions underlying Model 4 which was therefore taken as the final structure model.

Table 4-7 The refinement statistics of model 4.

	R_p	R_{wp}	χ^2	D-W
BMN	0.0538	0.0665	1.508	1.409, 1.437
BNN	0.0534	0.0648	1.458	1.301, 1.447

The final refinement results using model 4 are given in Table 4-4 and Table 4-5. The final difference profiles are shown in Figure 4-4, while the final displacively disordered average structure for BMN is shown in Figure 4-3. There are clearly strong qualitative similarities with the recently reported average structures of other Bi-pyrochlores [65] *c.f.*, for example, Figure 2 with Figure 4 and 5 of [58]. Nonetheless, subtle differences, in particular the relative magnitudes of the refined displacement magnitudes off the 16*d* and 8*b* sites for the *A* and O' sites exist.

Though the refined disordered average structures given in Table 4-4 and Table 4-5 for $Bi_{1.667}Mg_{0.70}Nb_{1.52}O_7$ (BMN) and $Bi_{1.667}Ni_{0.75}Nb_{1.5}O_7$ (BNN) are by no means sufficient to define the different local configurations and associated displacive relaxations possible, they are nonetheless important as they define the broad structural parameters within which any modelling of the local structure must necessarily operate. For instance, the displacive shifts of the local *A* site cations

away from the ideal pyrochlore *A* site positions should be of magnitude ~ 0.41 Å for both BMN and BNN and directed perpendicular to the local O'-*A*-O' axis. Likewise, any proposed local ordering of the Bi^{3+}, Mg^{2+}/Ni^{2+} and □'s on the *A* sites as well as of the Mg^{2+}/Ni^{2+} and Nb^{5+} on the neighbouring *B* site positions must explain why the *A* ion shifts induced by the local chemistry are necessarily perpendicular to the local O'-*A*-O' axis.

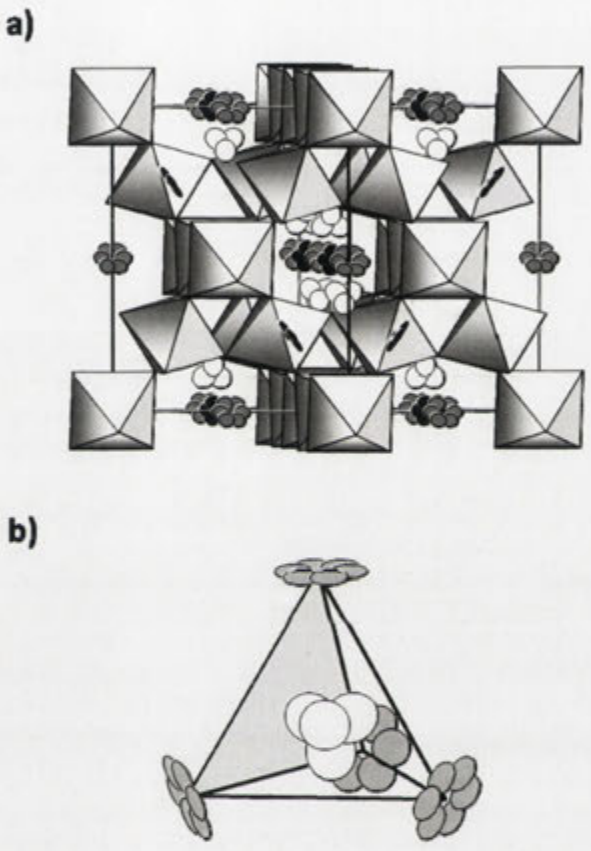

Figure 4-3 (a) The final displacively disordered average structure (Model 4, Table 4-4) for $Bi_{1.667}Mg_{0.70}Nb_{1.52}O_7$ (BMN) projected along a close to <110> direction. The corner-connected octahedral array represents the $(Mg_{0.24}Nb_{0.76})_2O_6$ sub-structure. The toroids of flat ellipsoids represent the six equivalent 96*h* *A*-site positions of the $O'(Bi_{0.833}Mg_{0.11})_2$ sub-structure. The tetrahedral clusters of ellipsoids represent the four equivalent 32e site positions for the displaced O' oxygens. (b) Shows an expanded view of one particular $O'(Bi_{0.833}Mg_{0.11})_4$ tetrahedron.

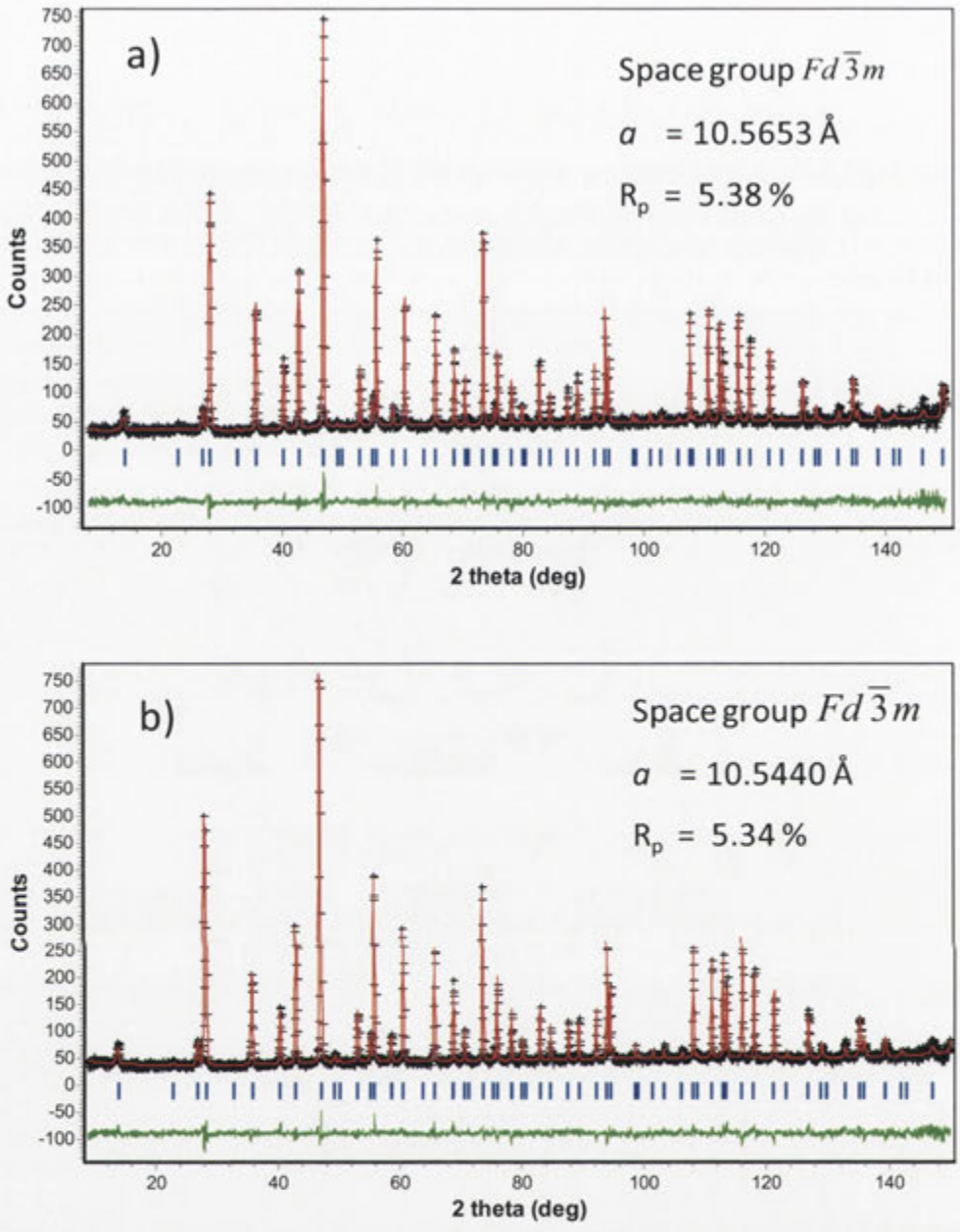

Figure 4-4 The final resultant neutron powder profile fits for (a) BMN and (b) BNN. Both plots show the experimental data points (black crosses), the calculated profile fits (red line), the difference profiles for the refinements (green line) and the positions of allowed Bragg reflection (vertical blue bars on the bottom).

4.3.4 Electron Diffraction Analyses

The O'A_2 sub-structure of the BMN and BNN cubic pyrochlores is clearly heavily displacively disordered as is apparent from Figure 4-3 above. Direct evidence as to the nature/origin of this displacive disorder is present in the form of characteristic structured diffuse intensity distributions most easily apparent in electron diffraction data. Figure 4-5, for example, shows (a) close to <1,1,-2>, (b) close to <6,-3,-1>, (c) close to <-3,3,2> and (d) close to <-1,3,0> zone axis EDP's typical of the $Bi_{1.66(1)}Mg_{0.70(3)}Nb_{1.52(1)}O_7$, BMN, cubic pyrochlore phase while Figure 4-6 shows (a) <-3,5,0>, (b) close to <2,2,-3> (c) close to <-1,5,0> and (d) close to <1,1,1> zone axis EDP's of the $Bi_{1.65(2)}Ni_{0.75(3)}Nb_{1.50(1)}O_7$, BNN phase. The first thing to note is that the observed highly structured diffuse distributions in both cases have distinct similarities to the structured diffuse distribution we have recently shown to be characteristic of a closely related $Bi_{1.89}Fe_{1.16}Nb_{0.95}O_{6.95}$ cubic pyrochlore phase [69] (*c.f.*, for example, Figure 4-5(a) with Figure 3(a) of [69] and Figure 4-6(b) and (d) with Figure 3(b) and (d) of [69]). Clearly the structural disorder characteristic of the latter $Bi_{1.89}Fe_{1.16}Nb_{0.95}O_{6.95}$ cubic pyrochlore phase is closely related to that characteristic of the BMN and BNN cubic pyrochlore phases (and, coincidentally, quite dissimilar to that characteristic of BZN and BZN-related cubic pyrochlore phases - *c.f. e.g.* Figure 4-5 and Figure 4-6 with Figure 3 and 4 of [38]; see also Figure 2-7 above).

In the case of the $Bi_{1.89}Fe_{1.16}Nb_{0.95}O_{6.95}$ cubic pyrochlore phase, the observed structured diffuse distribution took the form of {110}* sheets of diffuse intensity perpendicular to each of the six <110> directions of real space giving rise to diffuse streaking along all $\mathbf{G} \pm \varepsilon\langle h,-h,l\rangle^*$, **G** an average structure Bragg reflection and ε continuous, directions of reciprocal space. Very similar $\mathbf{G} \pm \varepsilon\langle h,-h,l\rangle^*$ diffuse streaking is also apparent in Figure 4-5 and Figure 4-6 *e.g.* along the $\mathbf{G} \pm \varepsilon\langle 3,-1,1\rangle^*$, $\mathbf{G} \pm \varepsilon\langle 1,-3,-1\rangle^*$ and $\mathbf{G} \pm \varepsilon\langle 668\rangle^*$ directions of reciprocal space in Figure 4-5(a) or along the $\mathbf{G} \pm \varepsilon\langle 10,-4,4\rangle^*$, $\mathbf{G} \pm \varepsilon\langle -4,10,4\rangle^*$ and $\mathbf{G} \pm \varepsilon\langle 668\rangle^*$ lines of reciprocal space in Figure 4-6 (b) *etc.* There are characteristic 'extinction conditions' associated with this diffuse streaking *e.g.* the $\mathbf{G} \pm \varepsilon\langle 668\rangle^*$ diffuse streaking in Figure 4-6 (b) runs through the $[hkl]^*$, $h - k = 4J$, J an integer, parent Bragg reflections such as *e.g.* [6,-6,0]* but not through Bragg reflections such as [424]* *etc.* Such 'extinction

conditions' along with the {110}* sheet form of the diffuse distribution are characteristic of essentially independent β-cristobalite like tetrahedral edge rotation of the O'A_2 sub-structure of the ideal pyrochlore structure type (as shown in Figure 4-7(b)). Displacive disorder of this type is correlated in one-dimensional chains along one or other of the six possible <110> directions but not correlated from one such chain to the next in the transverse direction and thus gives rise to {110}* sheets of diffuse intensity as is observed experimentally. Clearly similar displacive modulations of the O'A_2 sub-structure must also be taking place on the local scale in both BMN and BNN.

While the EDP's shown in Figure 4-5 and Figure 4-6 are quite similar to those shown in [69], however, there are nonetheless also some noticeable differences - in particular, the linear $\mathbf{G} \pm \varepsilon\langle h,-h,l\rangle^*$ streaking that exists at the orientations discussed above seem to break up into curved arcs at other orientations (see, for example, Figure 4-5(d) in the case of BMN and Figure 4-6 (a) and (c) in the case of BNN). In the case of the $\mathbf{G} \pm \varepsilon\langle 535\rangle^*$ 'streak' (labelled with a white line) which should run through the $\mathbf{G}$ = [0,0,-8]* Bragg reflection in Figure 4-6(a), for example, it is clear that this is no longer a continuous streak but has rather broken up into curved segments that almost look like they are part of an essentially continuous diffuse circle centred on [0,0,-4]* (see the white circle in Figure 4-6(a)).

There is no clear explanation for the above observations. However, one possibility is that the presence of significant numbers of vacancies on the A site (implied by the stoichiometry of these BNN and BMN phases) may mean that the initially independent β-cristobalite like tetrahedral edge rotations of the O'A_2 sub-structure shown in Figure 4-7(a) are now somehow coupled together leading to a related but rather more complex diffuse scattering distribution than {110}* sheets of diffuse intensity perpendicular to each of the six <110> directions of real space.

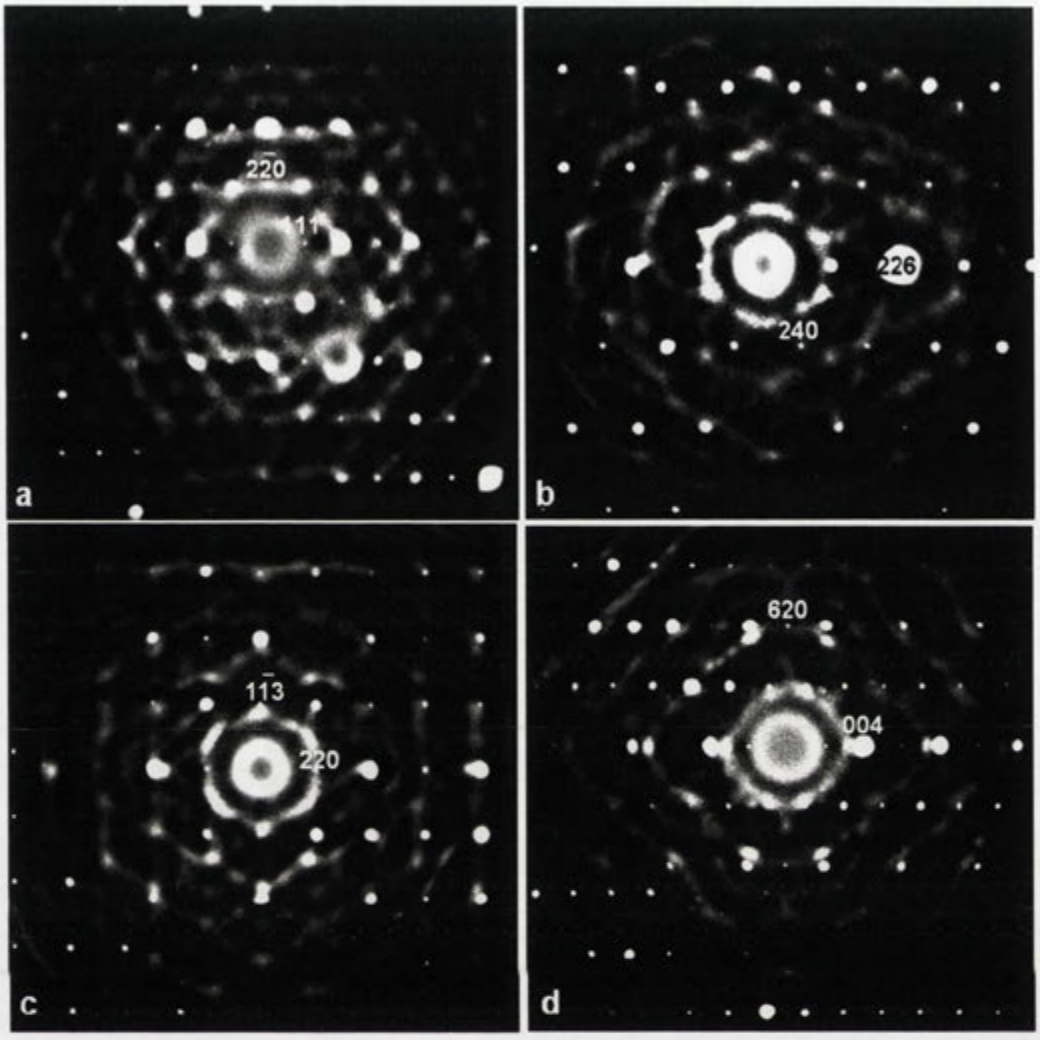

Figure 4-5 (a) Close to <1,1,−2>; (b) close to <6,−3,−1>; (c) close to <−3,3,2>; and (d) close to <−1,3,0> zone axis EDPs of the $Bi_{1.66(1)}Mg_{0.70(3)}Nb_{1.52(1)}O_7$, BMN, cubic pyrochlore.

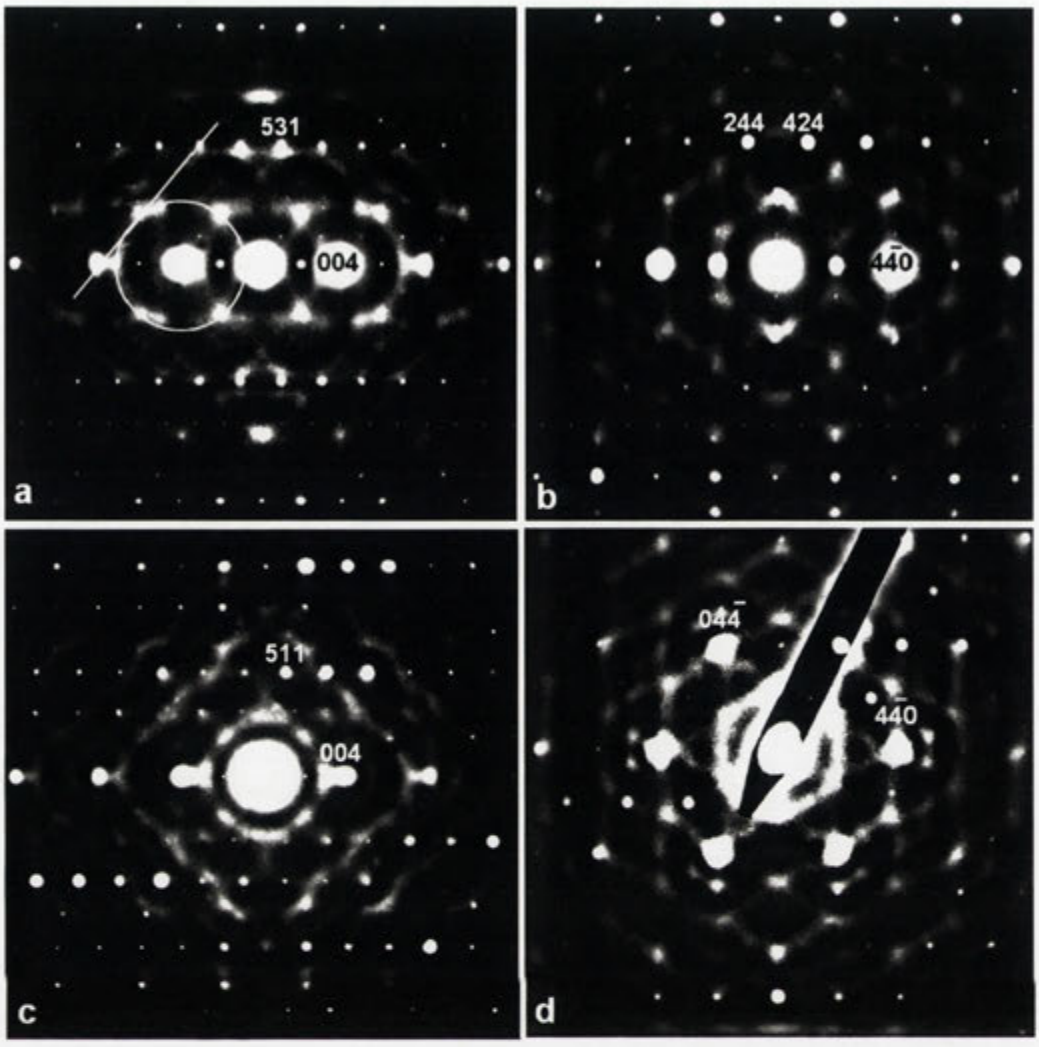

Figure 4-6 (a)<−3,5,0>, (b) close to <2,2,−3> (c) close to <−1,5,0> and (d) close to <111> zone axis EDPs of the $Bi_{1.65(2)}Ni_{0.75(3)}Nb_{1.50(1)}O_7$, BNN, cubic pyrochlore. Note the highly structured, characteristic diffuse intensity distribution accompanying the Bragg reflections of the underlying pyrochlore type average structure.

4.3.5 Local Crystal Chemistry

In order to obtain insight into the local forces responsible for the structured diffuse scattering shown in Figure 4-5 and Figure 4-6 along with the implied displacive disorder shown in Figure 4-7, an understanding of the local crystal chemistry of the underlying $Fd\bar{3}m$ average structures of the $Bi_{1.66}Mg_{0.70}Nb_{1.52}O_7$, BMN and $Bi_{1.65}Ni_{0.75}Nb_{1.50}O_7$, BNN, cubic pyrochlore phases is an indispensible first step. For this purpose, bond valence sum analysis [18,38,69] has been used. Given the average structure refinement results, the stoichiometry of the BMN cubic

pyrochlore is written in the form $(Bi_{0.830}Mg_{0.110}\square_{0.060})_2(Mg_{0.240}Nb_{0.760})_2O_7$ while that of the BNN cubic pyrochlore is written in the form $(Bi_{0.825}Ni_{0.125}\square_{0.050})_2(Ni_{0.250}Nb_{0.750})_2O_7$, where the symbol □ represents a vacancy on the ideal pyrochlore *A*-site.

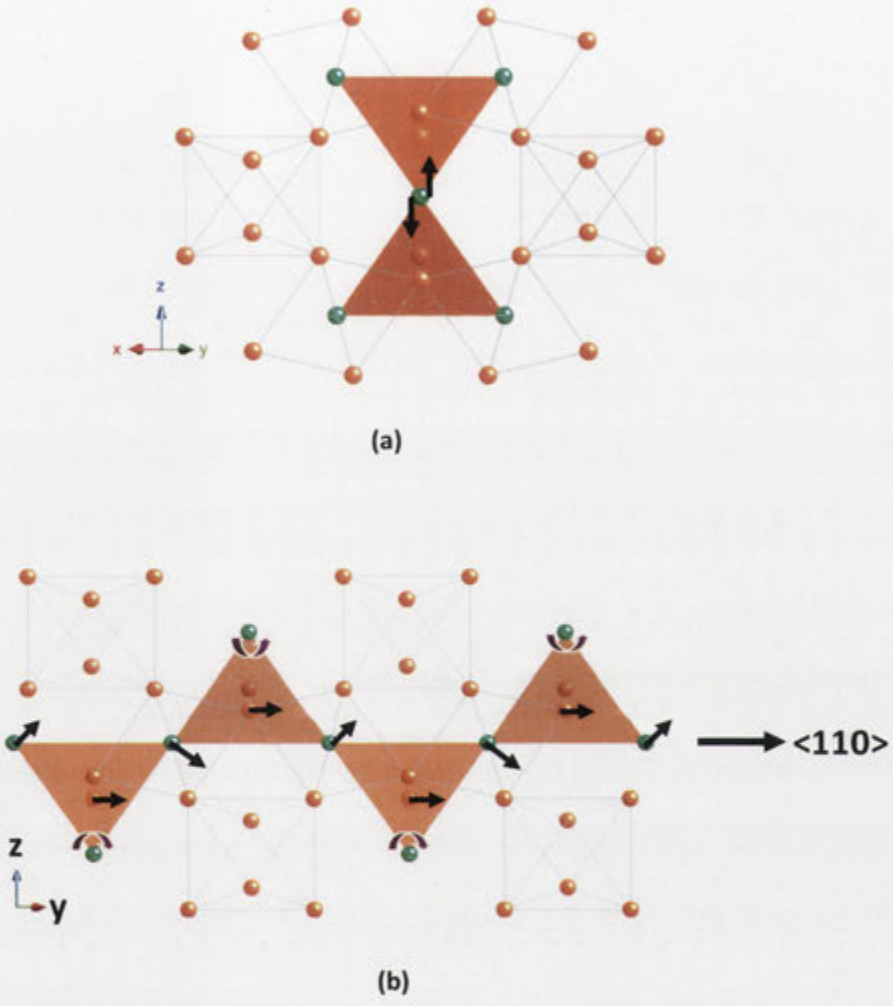

Figure 4-7 The characteristic 1-d, β-cristobalite type displacive disorder of the O'A_2 sub-structure (in brown) drawn relative to the surrounding B_2O_6 octahedral framework (outlined) sub-structure. The tetrahedral edge rotation axes run along the <1,-1,0> projection direction (a) shows a projection along <110> and (b) along <1,-1,0>.

The one unknown fractional co-ordinate in the ideal pyrochlore structure type, the *x* fractional co-ordinate of O, can be readily estimated using the bond valence sum approach [18,38,69] and the R_0 parameters listed in [70]. The bond valence sum, or apparent valence AV, of an ion is determined by the distances to neighbouring ions of the opposite formal valence and can be readily calculated using

the R_0 parameters listed in [70]. Given the average occupancies of the B sites, the expected average B–O bond length, $R(B\text{-O})$ should be such that

$$\begin{aligned} AV(B) &= 6 \times 0.240 \times \exp\{^{(1.693-R)}/_{0.37}\} + 6 \times 0.760 \times \exp\{^{(1.911-R)}/_{0.37}\} \\ &= 0.240 \times 2 + 0.760 \times 5 \\ &= 4.280 \end{aligned} \quad (4\text{-}1)$$

where $AV(B)$ is Apparent Valence (AV) [70]

and

$$\begin{aligned} AV(B) &= 6 \times 0.25 \times \exp\{^{(1.654-R)}/_{0.37}\} + 6 \times 0.75 \times \exp\{^{(1.911-R)}/_{0.37}\} \\ &= {}^{1}/_{4} \times 2 + {}^{3}/_{4} \times 5 \\ &= 4.250 \end{aligned} \quad (4\text{-}2)$$

in the cases of BMN and BNN respectively. This occurs for 1.9942 Å in the case of BMN and R = 1.9891 Å in the case of BNN.

An average $R(B\text{-O})$ bond length of 1.9942 Å for BMN occurs for x = 0.3163 given the relation between R(B-O) and x

$$R(B\text{-O}) = \sqrt{\{(x - {}^{1}/_{4})^2 + 2\,({}^{1}/_{8})^2\}} \times 10.5653 \text{ Å}. \quad (4\text{-}3)$$

Likewise, an average $R(B\text{-O})$ bond length of 1.9891Å occurs for x = 0.3163 given a = 10.5354 Å for BNN. The bond valence sum prediction for the value of x is thus ~ 0.3163 for both BMN and BNN. This particular value of x is in rather good agreement with the experimentally refined values for x (of 0.3198(1), in the case of BMN, and 0.3199(1) in the case of BNN) and is used in what follows.

With this choice of x, the 'average' B cations are reasonably well bonded in the average pyrochlore structure (see Table 4-8 and Table 4-9), particularly given that additional small amplitude relaxations of the O array (away from the Mg^{2+}/Ni^{2+} ions and towards the Nb^{5+} ions) associated with the local distribution of Nb^{5+} and

Mg^{2+}/Ni^{2+} on the *B* sites can be expected to simultaneously reduce the initial overbonding of the Mg^{2+}/Ni^{2+} ions and underbonding of the Nb^{5+} ions.

For Nb^{5+} in the *B* site, the ideal *B*-O distance *R*(Nb-O) is given by that distance which corresponds to an apparent valence [70] of $^5/_6$. From [70], this distance is given by

$$R(\text{Nb-O}) = 1.911 - 0.37 \ln (^5/_6) = 1.9785 \text{ Å}. \quad (4\text{-}4)$$

For Mg^{2+}/Ni^{2+} in the same *B* site, the equivalent ideal *B*-O distances are

$$R(\text{Mg–O}) = 1.654/1.693 - 0.37 \ln (^2/_6) = 2.0995 \quad (4\text{-}5)$$

$$R(\text{Ni–O}) = 1.654/1.693 - 0.37 \ln (^2/_6) = 2.0605 \quad (4\text{-}6)$$

Note, however, that both the Bi^{3+} and Mg^{2+}/Ni^{2+} ions are significantly under-bonded in the ideal pyrochlore *A*-site, particularly the latter Mg^{2+}/Ni^{2+} ions which are under-bonded by a massive 59.75%/63.2% respectively. This massive under-bonding of the Mg^{2+}/Ni^{2+} ions is the reason why the latter Mg^{2+}/Ni^{2+} ions are conventionally considered to be too small to occupy the pyrochlore *A*-sites.

Table 4-8 Bond Valence Sums (AV's) for the cubic pyrochlore average structure of BMN

A	*B*	AV(*A*)	AV(*B*)	AV(O)	AV(O')
Bi	Nb	2.354	4.796	1.991	2.352
Bi	Mg	2.354	2.661	1.280	2.352
Mg	Nb	0.805	4.796	1.733	0.804
Mg	Mg	0.805	2.661	1.021	0.804

Now consider the second O'A_2 tetrahedral corner-connected substructure of anti-cristobalite structure type (see Figure 1-1). The O' anion in this sub-structure is

tetrahedrally co-ordinated by 4 *A* cations at an average distance $R(O'\text{-}A) = (\sqrt{3}/8)a$ = 2.2875/2.2810 Å determined solely by the cubic lattice parameter *a*. The introduction of □'s onto the *A* sites to accompany the majority Bi^{3+} and minority Mg^{2+}/Ni^{2+} cations considerably complicates the local crystal chemistry, not only because it creates a much wider range of potential local [A_4] stoichiometries but also because their presence or otherwise significantly affects the AV of the O' anions which it neighbours and hence the driving forces for local displacive disorder of the Bi^{3+} and minority Mg^{2+}/Ni^{2+} cations.

Table 4-9 Bond Valence Sums (AV's) for the cubic pyrochlore average structure of BNN

A	B	AV(A)	AV(B)	AV(O)	AV(O')
Bi	Nb	2.392	4.858	2.019	2.387
Bi	Ni	2.392	2.426	1.208	2.387
Ni	Nb	0.736	4.858	1.742	0.735
Ni	Ni	0.736	2.426	0.932	0.735

Table 4-10 and Table 4-11 list the calculated AV of a centreing O' anion depending upon the local [A_4] stoichiometry of the tetrahedron of cations surrounding it. The probability of that particular configuration occurring (under the unlikely assumption of random ordering of the Bi^{3+}, Mg^{2+}/Ni^{2+} and □'s on the ideal pyrochlore *A* site) is also given. While not all theoretically possible local [A_4] stoichiometries are listed (only those with two Bi ions or more are listed), those that are listed account for over 98 % of those theoretically possible. For the most likely [Bi_4] or [Bi_3M] configurations (~ 70 % of the time) it can be seen that the centreing O' anion is either happily bonded or over-bonded implying that the under-bonded Bi^{3+} and Mg^{2+}/Ni^{2+} cations cannot improve their significant under-bonding by moving closer to the O' anions but must instead move off-centre perpendicular to the local O'-Bi-O' axis, as is ensured by the *β*-cristobalite type displacive distortion

shown in Figure 4-7 and implied by the structured diffuse scattering apparent in Figure 4-5(a), Figure 4-6(b) and (d).

Table 4-10 AV's for O' dependent upon local [A_4] stoichiometry for BMN

	[Bi_4]	[Bi_3Mg]	[$Bi_3\square$]	[Bi_2Mg_2]	[$Bi_2Mg_1\square_1$]	[$Bi_2\square_2$]
AV{O'}[A_4]	2.352	1.965	1.764	1.578	1.377	1.176
Prob. P	0.486	0.198	0.186	0.030	0.057	0.027

Table 4-11 AV's for O' dependent upon local [A_4] stoichiometry for BNN

	[Bi_4]	[Bi_3Ni]	[$Bi_3\square$]	[Bi_2Ni_2]	[$Bi_2Ni_1\square_1$]	[$Bi_2\square_2$]
AV{O'}[A_4]	2.387	2.071	1.790	1.559	1.376	1.194
Prob. P	0.463	0.281	0.112	0.064	0.051	0.010

When either a single □ or more than one non-Bi ion is present in the local [A_4] configuration, however, the O' anion becomes significantly under-bonded allowing it to move directly towards the also under-bonded *A* cations thus improving the under-bonding of all ions involved. The presence of a significant concentration of □'s on the *A* sites of these "... misplaced-displacive cubic pyrochlore ..." phases [20] thus seems to play a crucial role as far as the displacive disorder of the materials is concerned.

Now consider the [A_2B_2] co-ordination environment of the O ions. Table 4-12 and Table 4-13 list the calculated AV of a centreing O anion depending upon the local [A_2B_2] stoichiometry of the tetrahedron of cations surrounding it. The probability of that particular configuration occurring (under the unlikely assumption of random ordering) is also given. While again not all theoretically possible local [A_2B_2] stoichiometries are listed (only those with at least one Bi occupying an *A* site are listed), those that are listed account for over 90 % of those theoretically possible.

It can be seen that the AV of an O ion depends most significantly on the identity of the two *B* site cations to which it is bonded, being significantly under-bonded if one or other of these two *B* sites is occupied by a Mg^{2+}/Ni^{2+} cation and essentially happily bonded if both are occupied by a Nb^{5+} cation.

Table 4-12 AV's for O dependent upon local $[A_2B_2]$ stoichiometry for BMN

	$[Bi_2Nb_2]$	$[Bi_2NbMg]$	$[BiMgNb_2]$	[BiMgNbMg]	$[Bi\square Nb_2]$	[Bi□NbMg]
AV{O}$[A_2B_2]$	1.991	1.635	1.862	1.506	1.795	1.439
Prob. P	0.408	0.251	0.083	0.051	0.078	0.048

Table 4-13 AV's for O dependent upon local $[A_2B_2]$ stoichiometry for BNN

	$[Bi_2Nb_2]$	$[Bi_2NbNi]$	$[BiNiNb_2]$	[BiNiNbNi]	$[Bi\square Nb_2]$	[Bi□NbNi]
AV{O}$[A_2B_2]$	2.019	1.614	1.881	1.475	1.819	1.414
Prob. P	0.383	0.255	0.116	0.077	0.046	0.031

Given that the under-bonded *A* site cations, in the majority of cases, must move off-centre away from the local O'-*A*-O' axis towards some (but simultaneously away from other) O ions, it would seem to make most crystal chemical sense for them to move away from the O ions that are bonded to 2 Nb *B*-site cations and towards those that are bonded to 1 Nb and one Mg^{2+}/Ni^{2+} cation. Bond valence sum considerations show that a transverse shift of the *A* cation of ~ 0.65 Å in the case of $Bi_{1.65}Ni_{0.75}Nb_{1.50}O_7$ can increase the AV of the initially under-bonded Bi ion from 2.39 to 3.05. The equivalent effect in the case where *A* = Ni is, however, much more modest with the Ni AV only increasing from 0.74 to 0.94. It seems that such a large amplitude transverse displacement of the *A* cation is not the way to significantly improve the drastic under-bonding of the Mg^{2+}/Ni^{2+} cations in these structures. Following [38], it is suggested that the only way to significantly improve the drastic

under-bonding of the Mg^{2+}/Ni^{2+} cations in these materials is for the two O' anions bonded to it to both significantly contract in towards the Mg^{2+}/Ni^{2+} cation.

In the case of BZN and BZN-related Bi-pyrochlores, where the concentration of the small, heavily under-bonded M^{II} = Zn ions on the pyrochlore *A* site approaches 25 % and where the concentration of □'s on the *A* sites is sufficiently small, Liu et al [38] recently suggested a crystal chemically reasonable explanation in terms of $^1/_4$<112> inter-tetrahedral Zn-Zn separation distances from one $O'Bi_3Zn$ tetrahedra to the next (see Figure 6 of [38]). In the cases of BMN and BNN, however, where the concentration of the small, heavily under-bonded *M* = Mg or Ni ions on the pyrochlore *A* site is much more like 11-12 % rather than 25 % and where the concentration of □'s on the *A* sites is ~ 5 %, the explanation for the observed highly anisotropic displacive disorder on the *A* site is not so obvious. The structured diffuse scattering of BMN and BNN in section 4.3.3 shows that β-cristobalite-like $O'A_2$ tetrahedral edge rotation modes play an important role.

The severe underbonding (~ 60 %) of the small Mg/Ni ions on the pyrochlore *A* site of BMN or BNN (see bond valence calculation in section 4.3.5), regardless of whether or not they are presumed to displace perpendicular to the local O'-*A*-O' axis, can clearly only be remedied by O' displacements directed towards the Mg/Ni ions. Crystal chemical considerations in section 4.3.5 suggest that the magnitude of these shifts need to be substantial, ~ 0.5 Å in the case of BMN and BNN. The refined O' shift from Table 4-4 and Table 4-5 are a bit smaller at ~0.35 Å/ ~ 0.37 Å. Note, however, that these latter shifts represent the centres of rather large displacement ellipsoids (see Figure 4-3(b)). The presence of ~ 5 % □'s on the *A* sites, however, complicates matters considerably. When an O' ion is surrounded by either 4 Bi's of 3 Bi's and one Mg or Ni ion (the most likely local configurations), the centreing O' ion is either happily bonded or over-bonded implying that the significantly under-bonded Bi and heavily under-bonded Mg or Ni ions cannot improve their under-bonding by moving closer to the O' ions but must instead move perpendicular to the local O'-*A*-O' axis. When an O' ion is surrounded by 3 Bi's and one □ (a reasonably common likelihood), however, the centreing O' ion will be under-bonded (see Table 4-10 and Table 4-11) and hence will move away from the □ and towards the remaining three Bi ions.

Finally, it is important to point out that the β-cristobalite-like O'A_2 tetrahedral edge rotation modes implied by the observed structured diffuse scattering and shown in Figure 4-7 involve both tetrahedral rotation as well as rigid body translation of the O'A_2 tetrahedral sub-structure relative to the B_2O_6 octahedral sub-structure. Given that the O'$(Bi^{3+}_{0.83}Mg^{2+}_{0.11})_2$ tetrahedral sub-structure of BMN has a formal charge of +3.42 while the O'$(Bi_{0.83}Ni_{0.125})_2$ tetrahedral sub-structure of BNN has a formal charge of +3.48, it is clear that these large amplitude displacive modes of distortion are inherently polar and thus capable of responding to an applied external electric field. The dielectric properties of BMN and BNN were thus investigated.

4.3.6 Dielectric Properties

Pressed pellets of the BMN and BNN samples (diameter 12 mm, thickness 1 mm, and relative density > 95%) were polished on both sides and coated with silver paste for dielectric measurement using the high precision LCR meter (HP4284A) and environmental box described in Chapter 3 above over the temperature range from 325 K down to liquid nitrogen temperature, ~ 90 K.

The measured dielectric permittivities as well as dielectric loss tangents of the BMN and BNN samples as a function of applied frequency up to 1 MHz at room temperature (a for BMN, b for BNN) are shown in Figure 4-8. The largely frequency independent, measured permittivities of BMN and BNN of 151 and 116 respectively at room temperature are quite respectable and both ~ 3-4 times higher than those reported for $Bi_{1.5}MgNb_{1.5}O_7$ and $Bi_{1.5}NiNb_{1.5}O_7$ by Sirotinkin and Bush [58]. (Cann *et al.* [21] reported rather more similar dielectric permittivities (at 1 MHz) of 210 and 122 for $Bi_2(Mg_{2/3}Nb_{4/3})O_7$ and $Bi_2(Ni_{2/3}Nb_{4/3})O_7$ respectively). The measured dielectric loss tangents are also desirably low (*e.g.* 0.00065 and 0.00042 respectively at 100 kHz - see Figure 4-8 (a) and (b).

Figure 4-9 shows the measured dielectric permittivities and dielectric loss tangents of the BMN and BNN samples at 1 kHz, 10 kHz, 100 kHz and 1 MHz as a function of temperature from ~ 325 K down to liquid nitrogen temperature *i.e.* ~ 90 K. The low temperature frequency dispersive behaviour characteristic of Bi-pyrochlores is clearly apparent [21] with the maximum in both the dielectric permittivity and the dielectric loss tangent moving to higher temperature with

increased measurement frequency. Note that the peak in the dielectric loss curve at 1 MHz occurs at $T_m \sim 112$ °K in the case of BMN and at ~ 130 °K in the case of BNN. At 1 MHz, the maximum in the dielectric permittivity is ~ 172 at ~ 190 K in the case of BMN and ~ 118 at ~ 220 K in the case of BNN. In the case of BNN, there is some indication that that the dielectric loss versus temperature curve below T_m does not simply reduce towards zero on further lowering of temperature but rather may be entering a plateau region in the vicinity of the lowest temperature obtainable.

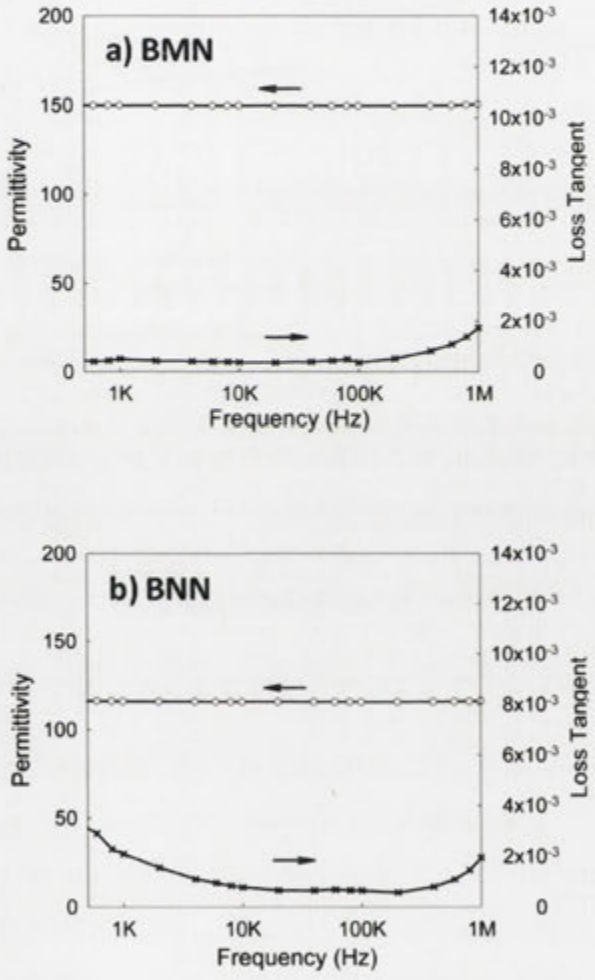

Figure 4-8 The measured dielectric permittivities as well as dielectric loss tangents of the BMN and BNN samples as a function of applied frequency up to 1 MHz at room temperature (a for BMN, b for BNN).

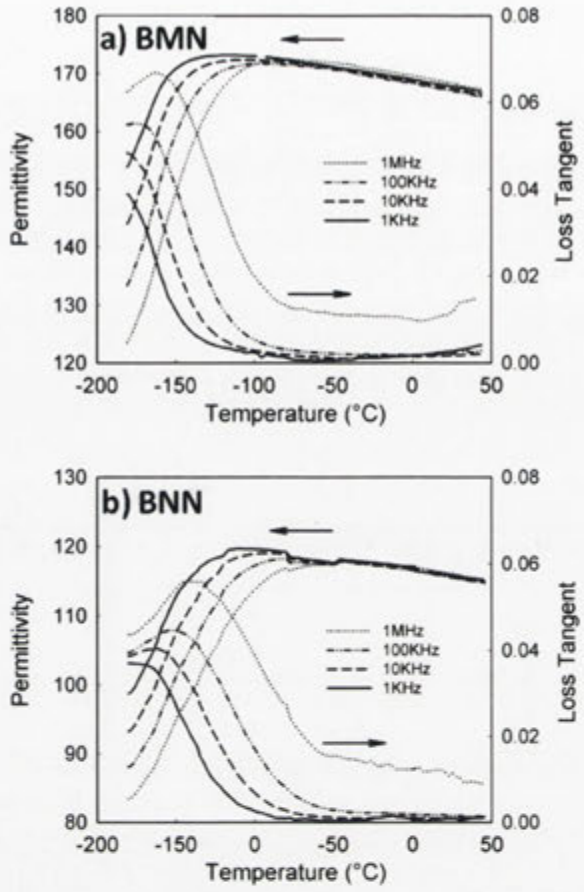

Figure 4-9 The measured dielectric permittivities as well as dielectric loss tangents of the BMN and BNN samples as a function of applied frequency at 1, 10, 100 kHz and 1 MHz as a function of temperature from ~ 325 K down to liquid nitrogen temperature, i.e. ~ 90 K ((a) for BMN, (b) for BNN).

4.4 Summary

In summary, single phase BMN and BNN, Bi-based, cubic pyrochlores have been synthesised and their compositions confirmed by quantitative EPMA in conjunction with Rietveld analysis of their underlying average structures. The $(Bi_{0.833}Mg_{0.11}\square_{0.06})_2(Mg_{0.24}Nb_{0.76})_2O_7$ and $(Bi_{0.833}Ni_{0.125}\square 0.04)_2(Ni_{0.25}Nb_{0.75})_2O_7$ ($\square$ a vacancy) compositions found are not compatible with either the $Bi_2(M^{II}_{2/3}Nb^{V}_{4/3})O_7$, ($M$ = Ni and Mg) composition proposed by Golovshchikova *et al.* [22] and Cann *et al.* [21] or the $(Bi_{1.5}M^{II}_{0.5-\delta})(M^{II}_{0.5}Nb_{1.5})O_{7-\delta}$ composition proposed by Sirotinkin and Bush [58]. The composition of the BNN phase, however, is in agreement with the phase analysis investigation of the ternary Bi_2O_3-NiO-Nb_2O_5 system recently

reported by Valant and Suvorov [67] provided the composition they reported for the BNN phase is re-normalised to seven oxygens.

Average structure refinements show that the O'A_2 tetrahedral sub-structure is heavily displacively disordered. Electron diffraction shows that this displacive disorder arises from essentially independent β-cristobalite like tetrahedral edge rotation and (inherently polar) rigid body translation of the O'A_2 sub-structure of the ideal pyrochlore structure type. Displacive disorder of this type is correlated in one-dimensional chains along one or other of the six possible <110> directions but not correlated from one such chain to the next in the transverse direction and thus gives rise to {110}* sheets of diffuse intensity as observed experimentally. Bond valence sum analysis is used to attempt to rationalise the observed behaviour in terms of the local crystal chemistry. Finally the dielectric behaviour of both the BMN and BNN phases are reported. Low temperature dielectric relaxation behaviour is found in both cases.

Chapter 5: The Stoichiometric Bismuth based Pyrochlores $Bi_2M^{III}NbO_7$, M = In and Sc.

In this chapter, two Bi-based niobate pyrochlore phases which have both previously been reported to occur at the ideal $Bi_2(M^{III}Nb^{V})O_7$ stoichiometry without any compositional disorder on the pyrochlore A site, namely the Bi_2InNbO_7 (BIN) and Bi_2ScNbO_7 (BSN) pyrochlore systems, are examined in order to establish whether or not A site stoichiometric, Bi-based niobate pyrochlores can really exist, to study the inherent displacive disorder therein and to investigate the nature of their dielectric relaxation properties.

5.1 Introduction

As mentioned in Chapter 1, the composition of the Bismuth-based niobate pyrochlores that are the subject matter of this Chapter have traditionally been assumed to be fixed and of ideal stoichiometry $Bi_2M^{III}NbO_7$, or $M^{III}NbO_6{\bullet}O'Bi_2$ [21,22]. As also mentioned above, however, the true cubic pyrochlore phase in many such systems has recently been shown to often be a solid solution, significantly Bi-deficient with respect to the above traditional stoichiometries and to require the presence of nominally too small M^{3+} cations on the *A* as well as the *B* sites of the ideal $A_2B_2O_7$ pyrochlore structure type (see *e.g.* [17,20,28,62,68]). They have thus recently been christened 'misplaced-displacive' cubic pyrochlores [20].

On cooling to low temperatures (~ 70-250 K), they typically exhibit an anomalous, frequency dispersive, step-like decrease in the real part of the dielectric permittivity along with a correlated, broad, frequency-dependent peak in the imaginary part of the dielectric permittivity [21,22,65,66,68,71,72]. Similar behaviour has recently also been reported for a non-Bi containing, ~ $Ca_{1.47}Ti_{1.47}Nb_{1.04}O_7$ 'misplaced-displacive' cubic pyrochlore (investigated in Chapter 6). Such low temperature dielectric relaxation behaviour is strongly reminiscent of the behaviour of relaxor ferroelectrics [21,65,66,71,72] as well as of electric dipolar and quadrupolar glasses (such as *e.g.* $Rb_{1-x}(NH_4)_xH_2PO_4$ [21,26,73]). The low temperature peak in the imaginary part of the dielectric permittivity (at T_m) in the MHz region typically moves systematically to higher temperature upon increasing frequency. Indeed, its positioning (at room temperature) practically rules out the room temperature use of many of these Bi-based pyrochlores in the commercially important RF/MW frequency range [21]. It is therefore of some considerable importance, from both the fundamental as well as applied points of view, to be able to identify and understand the structural origin of the dipole moments as well as the glassy dielectric relaxation behaviour of these dipoles.

While the dipolar origin of the anomalous relaxation behaviour has yet to be clearly identified, it is apparent that the displacive disorder associated with the tetrahedral $O'A_2$ sub-structure (see *e.g.* Figure 4-3 above), and not simply the presence of a polarisable lone pair cation such as Bi^{3+} on the pyrochlore *A*-site (see Chapter 4 and [74], is intimately involved [65,66,71,72]. The current prevailing view seems to be that the "... relaxation stem(s) from the (random) hopping of

dynamically disordered *A* and O' ions among (discrete but) closely spaced possible positions ..." [65] (see *e.g.* Figure 4-7 above). In this context, the recent density functional theory (DFT) calculations on the displacively disordered $Bi_2Ti_2O_7$ pyrochlore suggesting the presence of multiple possible displacement sites and that the hopping is far from random [26] are interesting.

Whether this displacive disorder (hopping) is inherent or induced by chemical disorder, in particular on the pyrochlore *A* site, however, is far from clear *e.g.* in the case of the BZN pyrochlore it has been stated that "... the partial substitution of Zn ions for Bi ions leads to more than one equivalent potential minima at the *A* sites and ... to the dielectric relaxation ..." [72]. By contrast, the inherent displacive disorder in the pure Bi on *A* site, $Bi_2Ti_2O_7$ pyrochlore [26,75] shows that displacive disorder can certainly exist without chemical disorder on the O'A_2 sub-structure. Unfortunately, the method of synthesis of this $Bi_2Ti_2O_7$ pyrochlore rules out the preparation of a sufficiently dense sample to measure whether a low temperature dielectric relaxation also exists in $Bi_2Ti_2O_7$ [75] as a result of this inherent displacive disorder.

Given the recent discovery [76] that many, if not most, Bi-based niobate pyrochlores do not in fact form at the nominally ideal $Bi_2(M^{II}_{2/3}Nb^{V}_{4/3})O_7$ or $Bi_2(M^{III}Nb^{V})O_7$ pyrochlore type compositions [21] but rather form so-called 'misplaced-displacive' pyrochlore solid solutions with up to ~ 25% of the *A* site positions being occupied by nominally too small, typically *B* site cations [17,18,20,68,69], it might seem that the displacive disorder induced by the misplacement of the traditional *B* site cations onto the *A* sites (*i.e.* by chemical disorder) might be causally connected with the low temperature dielectric relaxation behaviour. If this were the case, however, the large amplitude displacive disorder and associated low temperature dielectric relaxation behaviour should not occur unless compositional disorder is present on the pyrochlore *A* site *i.e.* unless a cation other than Bi occupies the *A* site. It therefore becomes important to investigate the role of chemical disorder in the O'A_2 sub-structure on the displacive disorder and dielectric behaviour of these systems.

The object of this chapter, therefore is to investigate the composition, inherent structural disorder and low temperature dielectric properties of two particular Bi-based niobate pyrochlore systems which have both previously been reported to occur at the ideal $Bi_2(M^{III}Nb^{V})O_7$ stoichiometry without any compositional disorder on the

pyrochlore *A* site, namely the Bi_2InNbO_7 (BIN) and Bi_2ScNbO_7 (BSN) pyrochlore systems [21]. The purpose is, firstly, to establish whether or not *A* site stoichiometric, Bi-based niobate pyrochlores can really exist; secondly, to use electron diffraction to investigate the nature of the displacive disorder therein and, thirdly, to re-investigate the dielectric relaxation properties of these *A* site stoichiometric, Bi-based niobate pyrochlores.

5.2 Sample Preparation

Bi_2InNbO_7 (BIN) and Bi_2ScNbO_7 (BSN) samples at the ideal nominal compositions were both synthesised via solid state reaction. The starting materials used were high purity Bi_2O_3 (99.995 %, Koch-Light), In_2O_3 (99.99 %, Aldrich), Sc_2O_3 (99.99 %, Hudson Lab.) and Nb_2O_5 (99.9+ %, Alfa) respectively. The sintering temperature was 1050 °C and 1000 °C for the BIN and BSN samples respectively with a sintering time of 2 days.

5.3 Results

5.3.1 X-ray Powder Diffraction Results

Figure 5-1 and Figure 5-2 shows XRD patterns of both the BIN and BSN samples collected on a SIEMENS D-5000 diffractometer using Cu K_α radiation, respectively. No trace of an impurity phase could be found in either pattern. Rather, both samples were found to be single phase cubic pyrochlore to XRD, implying the nominal $Bi_2M^{III}NbO_7$ stoichiometry. The average structure of the BIN and BSN samples were indexed to the usual $Fd\bar{3}m$, fcc cubic pyrochlore unit cell giving a = 10.792(2) Å in the case of BIN and a = 10.660(9) Å in the case of BSN. Similar to the BMN and BNN samples (see section 4.3.1), the presence of weak reflections forbidden for the ideal pyrochlore structure type, such as the 248 reflection, in both cases is indicative of inherent displacive disorder in the O'A_2 sub-structure (as pointed out by Birchal and others [17,20,28,31,32,33]).

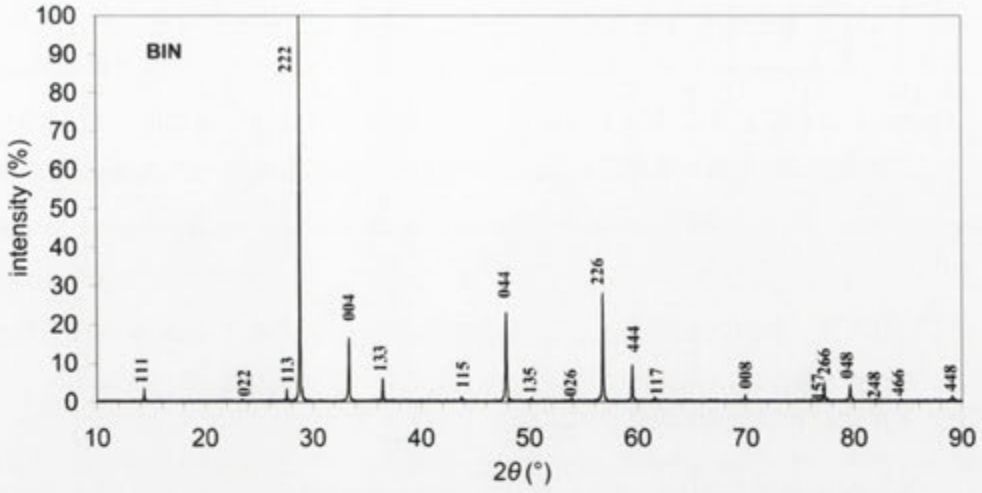

Figure 5-1 XRD patterns of the BIN samples collected on a SIEMENS D-5000 diffractometer using Cu K_α radiation.

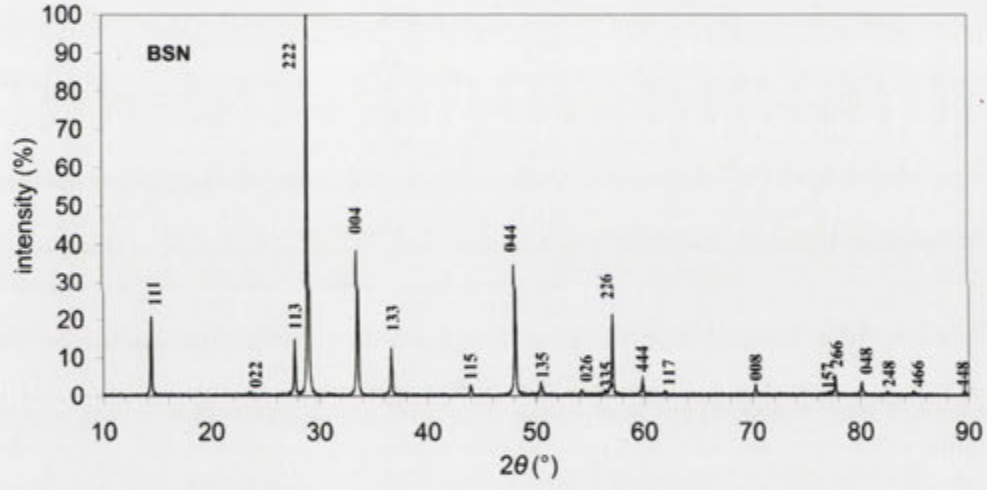

Figure 5-2 XRD patterns of the BSN samples collected on a SIEMENS D-5000 diffractometer using Cu K_α radiation.

5.3.2 Electron Probe Microanalysis

In order to confirm the nominal Bi_2MNbO_7 stoichiometry, the as-synthesised samples were further investigated by quantitative EPMA to check for homogeneity and composition, using $BiNbO_4$, Sc_2O_3 and $InNbO_4$ as calibration standards. Note that the typical accuracy of quantitative EPMA using appropriate calibration standards is accepted to be ~ ±2 % relative (see *e.g.* [37]). In the case of BIN, the sample was found to be homogeneous and single phase of average composition

$Bi_{1.98(2)}In_{0.99(2)}Nb_{1.01(2)}O_7$ (normalised to seven oxygens). In the case of BSN, the sample was again found to be homogeneous and single phase of average composition $Bi_{1.99(1)}Sc_{0.96(1)}Nb_{1.03(1)}O_7$. Both EPMA determined compositions are thus in agreement (within error) to the nominal starting stoichiometries. The quoted error bars represent the standard deviation from 20 separate spot analyses used to obtain the quoted average compositions. Thus the possibility of *A* site stoichiometric, $Bi_2M^{III}NbO_7$ niobate pyrochlores, with Bi only occupying the *A* sites, is established.

5.3.3 Electron Diffraction Analyses

In order to investigate inherent displacive disorder in these samples, electron diffraction was carried out both at room temperature as well as at close to liquid nitrogen temperature (well below the peak in the imaginary permittivity at T_m, see Figure 5-5 below) searching for evidence of structured diffuse scattering characteristic of chemical and/or displacive disorder. Figure 5-3 shows typical (a) <1,-1,0>, (b) <-2,2,1>, (c) <-3,6,-1> and (d) <5,1,-2> zone axis electron diffraction patterns (EDPs) of BSN at room temperature while Figure 5-4 shows (a) <-1,-1,10> and (b) <-5,3,2> zone axis EDPs of BSN at close to liquid nitrogen temperature. Essentially identical EDPs were also found for BIN (see [69,77]). Highly structured diffuse streaking is present in each EDP both above and below T_m, always running along a <*h*,-*h*, *l*>* direction of reciprocal space orthogonal to one of the six <110> directions of the underlying average structure *e.g.* in Figure 5-3(b), diffuse streaking running along the [12,8,8]*, [8,12,-8]* and [2,-2,8]* directions of reciprocal space orthogonal to the [0,1,-1], [101] and [110] directions of real space respectively is clearly apparent while, in Figure 5-4(d), diffuse streaking running along the [3,-5,5]*, [1,-7,-1]* and [155]* directions of reciprocal space orthogonal to the [011], [101] and [0,1,-1] directions of real space is likewise clearly apparent *etc.*

Such diffuse streaking collectively takes the form of well-defined {110}* sheets of diffuse intensity orthogonal to the six <110> directions of the underlying average structure. Essentially identical structured diffuse scattering was found to be characteristic of BIN [69,77] as well as the close to *A* site stoichiometric $Bi_2Ru_2O_{7-\delta}$ [78] and $(Bi_{1.89}Fe_{0.11})(Fe_{1.05}Nb_{0.95})O_{6.95}$ (BFN) [25] pyrochlores. (Closely related but subtly different diffuse scattering has also been found in the more *A* site compositionally disordered $(Bi_{1.65}Ni_{0.25}\square_{0.10})(Ni_{0.50}Nb_{1.50})O_7$ (BNN) and

$(Bi_{1.67}Mg_{0.17}\square_{0.16})(Ni_{0.47}Nb_{1.53})O_7$ (BMN) samples (see Chapter 4 above). The transverse polarised [78] nature of this characteristic structured diffuse distribution requires that the displacements responsible are both correlated as well as directed along the <110> directions without any correlation from one such <110> column to the next in the perpendicular direction as shown in Figure 4-7(b). Taken together with the diagnostic characteristic 'extinction condition' whereby the $<hkl>^* \pm\varepsilon<h,-h,l>^*$ sheets of diffuse intensity perpendicular to <110> are observed only when $h+k$ = 4J, J an integer, the observed diffuse scattering can only arise from β-cristobalite-like, correlated rotations and associated translations of chains of corner-connected $O'Bi_4$ tetrahedra, as shown in Figure 4-7 (b). Note that from the diffraction point of view, these polar displacive modes of distortion could be either static or dynamic in nature.

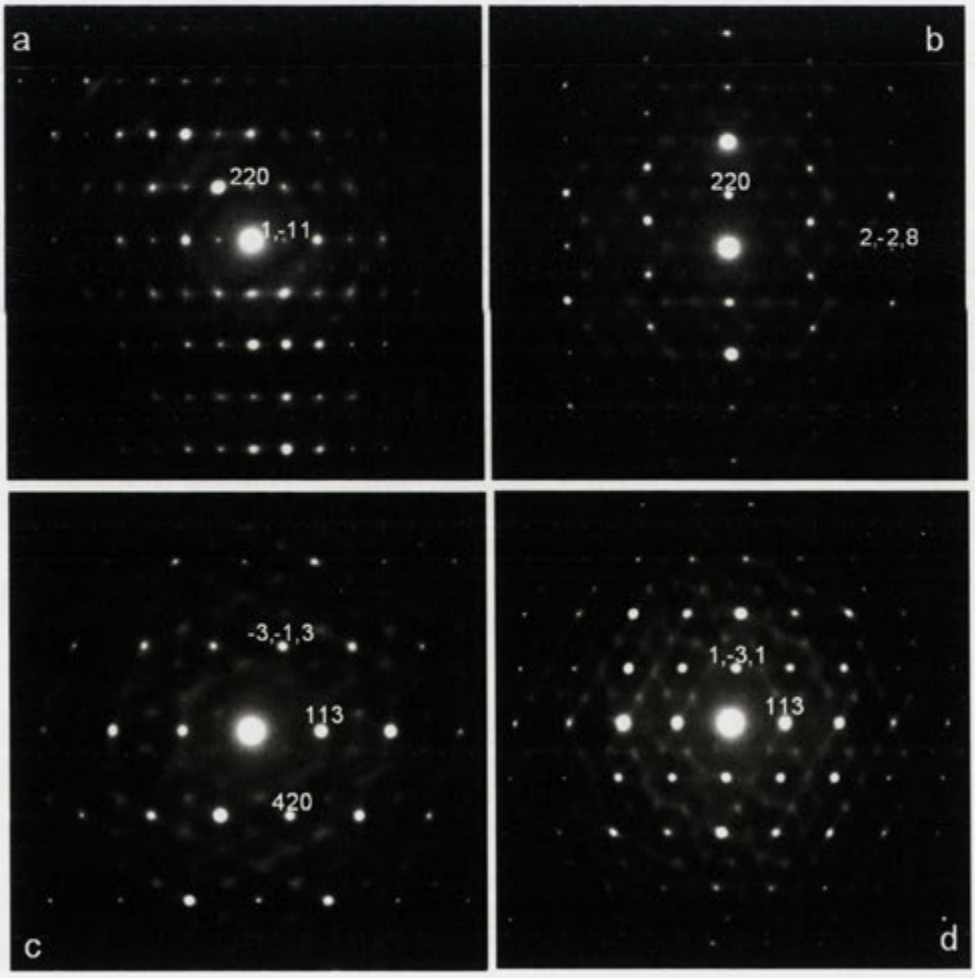

Figure 5-3 Typical (a) <1,-1,0>, (b) <-2,2,1>, (c) <-3,6,-1> and (d) <5,1,-2> zone axis electron diffraction patterns (EDPs) of BSN.

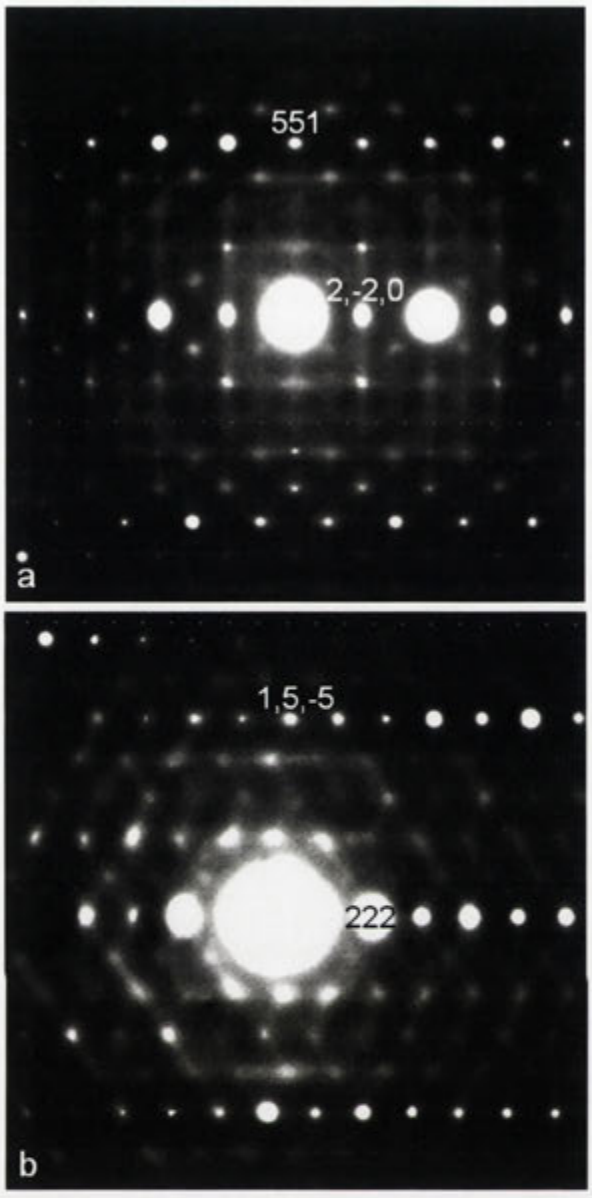

Figure 5-4 Typical (a) <-1,-1,10> and (b) <-5,3,2> zone axis EDPs of BSN at close to liquid nitrogen temperature.

The superposition of all such correlated chain rotation modes gives rise to an instantaneous real space distribution (see *e.g.* [78, Figure 4(b)]) that is consistent not only with the observed structured diffuse intensity but also with the refined 'disordered' average structures of such Bi-pyrochlores (see *e.g.* Figure 4-4(a)). In particular, it gives rise to strongly correlated O' and Bi displacements, to a flat disc-like region of Bi occupancy perpendicular to the local O'-Bi-O' axis as well as individual $O'Bi_4$ tetrahedra that are tightly constrained and rather closer to an ideal tetrahedron than the average structure might imply (see [78]). Note that the latter

result suggests that "... the spin-ice rules found in complex Bi-based pyrochlores, where two-long and two-short bonds are found in each tetrahedron of $O'Bi_4$ ..." [26] and first proposed by Seshadri [79] in the context of ice are unlikely to be applicable in the case of displacively disordered (but non-chemically disordered) Bi-pyrochlores.

Note that the strongly anisotropic Bi distribution implied by correlated chain rotation modes and the observed diffuse distribution (see Figure 5-3 and Figure 5-4; see also [78]) is typically modelled in conventional powder diffraction analyses via split-site models around the ideal pyrochlore *A* site position as have commonly been reported (*e.g.* [17-19,68,69,75,77,80,81]). Usually this is modelled in terms of a single disordered site, typically either the 96*g* or 96*h* site. Various authors (see *e.g.* [18,68,75,81]), however, have pointed out that these two sites are virtually indistinguishable from the refinement point of view. Indeed, the recent DFT based investigation of the displacively disordered $Bi_2Ti_2O_7$ pyrochlore predicted occupancy of 96*g*, 96*h* as well as 192*i* sites [26]. Such results suggest that there may be no discrete disordered sites at all but rather an essentially continuous scattering density around the ideal pyrochlore *A* site position [81]. Such a viewpoint comes very close to the disordered β-cristobalite type model (see [78]).

It is most important to note that the β-cristobalite-like, correlated chain rotation modes required by the observed diffuse distribution involve rotation as well as rigid body translation of a nominally +4 charged $O'Bi_2$ column of tetrahedra along a <110> direction relative to the nominally -4 charged $M^{III}Nb^{V}O_6$ octahedral sub-structure (see Figure 4-7) thus leading to a net dipole moment along the relevant <110> direction. The polyhedral connectivity of the constituent $O'Bi_4$ tetrahedra in conjunction with the fact that the tetrahedral rotation is around a tetrahedral edge and not through the centre of the tetrahedron means that there need be no correlation in the sense of the rotation (and hence in the sign of the corresponding dipole moment) from one <110> chain to a neighbouring chain. The length in real space of these inherently 1-d dipolar chains (in essence 1-d polar nano regions, PNR's) must be reasonably long to be compatible with the sharpness of the {110} sheets of diffuse intensity in reciprocal space (see Figure 5-3 and Figure 5-4).

The fact that the observed structured diffuse distribution takes the same form both above and below the peak in the imaginary part of the dielectric permittivity (see Figure 5-3 and Figure 5-4) does not mean that these 1-d PNR's are unrelated to the observed relaxor dielectric behaviour, in particular to the peak in the imaginary part of the dielectric permittivity at T_m (see Figure 5-5). Essentially identical behaviour, for example, has been observed in the case of the $Ba(Ti_{1-x}Sn_x)O_3$ and $Ba(Ti_{1-x}Zr_x)O_3$, for $x \geq 0.1$, relaxor ferroelectric systems [82] and, more recently, in the case of a PLZT(7.0/60/40) sample close to the morphotropic phase boundary therein [83]. In each of these cases, the observed structured diffuse scattering arises from similar 1-d PNR's that are known to be directly related to the relaxor ferroelectric properties of the materials. The observed diffuse phase transition in these cases can thus only be attributed to a dynamic freezing or glass-like transition involving the slowing down of the dipolar dynamics of the 1-d PNR's [84] implied by the existence of the structured diffuse distribution [82-84].

The observed structured diffuse distribution implies that 1-d PNR's of the type shown in Figure 4-7 exist along all six <110> directions. As shown by the example of SiO_2-cristobalite itself [85,86,87], it is possible for such a system to undergo a coherent structural phase transition on cooling *i.e.* for a particular RUM mode to condense out. Such a transition, however, usually requires the metric symmetry of the structure to be able to change in response. It is proposed that the rigidity of the $M^{III}NbO_6$ framework sub-structure in the case of BIN and BSN prevents strain distortion of the $O'Bi_2$ sub-structure itself and hence transverse correlation from one 1-d PNR to the next thereby giving rise to the glassy dielectric relaxation behaviour at low temperature and preventing the onset of long range ferroelectric ordering, even at the lowest possible temperatures. It is thus suggested that these intrinsically very low energy, correlated, chain rotation modes (analogous to the so-called Rigid Unit Mode (RUM) modes of β-cristobalite [85,86,87]) provide an important key to understanding the structural origin of the dipoles as well as the glassy relaxation behaviour of Bi-based niobate pyrochlores.

5.3.4 Dielectric Properties

While the low temperature dielectric properties of BIN and BSN have previously been reported [21], they have not been reported for BIN and BSN samples that have been explicitly shown to have the ideal Bi_2MNbO_7 stoichiometry. Figure 5-5 shows the measured temperature-dependent real and imaginary parts of the dielectric permittivity of the BIN and BSN samples as a function of applied frequency from 500 Hz up to 1 MHz (a for BIN, b for BSN). The real and imaginary parts of the dielectric permittivity of both BIN and BSN exhibit very similar temperature dependent dielectric relaxation behaviour to other non-stoichiometric Bi-based pyrochlores *e.g.* the temperature (T_m) at which the dielectric loss peaks shifts systematically to higher temperature as the measuring frequency increases while the magnitude of the dielectric loss at this peak, as well as its temperature-dependent width, also increase systematically with increasing frequency [20,21,65,66,68,71].

5.3.5 Raman Spectroscopy Analyses

Temperature-dependent micro-Raman spectra were also collected from 77 K up to room temperature (293 K) looking in particular for any evidence of some sort of structural phase transition in the vicinity of the peak in the imaginary part of the dielectric permittivity (see Figure 5-5). Figure 5-6 shows the measured micro Raman spectra of the BIN sample from 77 K up to 293 K. The mode assignments follow those given in McCauley [88]. Note that the Bi-O stretch band at ~ 350 cm^{-1} as well as the O-Bi-O band at ~ 220 cm^{-1} appear to shift slightly in frequency as well as to gain some oscillator strength on cooling to low temperature. While there are some subtle shifts like this in the frequency and strength of the observed modes on cooling, there is clearly no evidence in the Raman spectra for any well-defined 'phase transition', in agreement with the observed temperature-dependent electron diffraction behaviour described above.

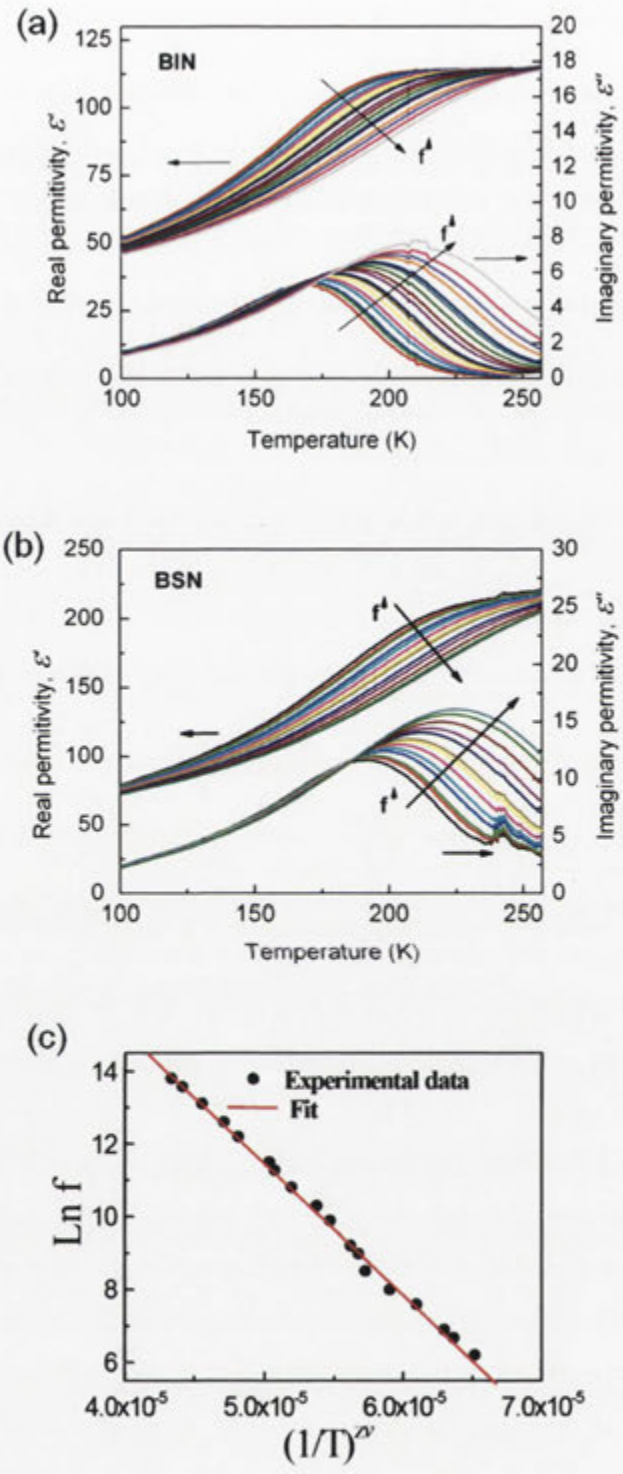

Figure 5-5 The temperature-dependence of the real and imaginary parts of the dielectric permittivity of (a) BIN and (b) BSN at frequencies from 500 Hz to 1 MHz (c) the best fit to the maximum in the dielectric loss as a function of frequency for the BIN sample using the relation $f = f_0 \exp-(\frac{T_{Ea}}{T})^{zv}$, **where** $T_{Ea} = E_a/k$ **and** $zv = 1.9$.

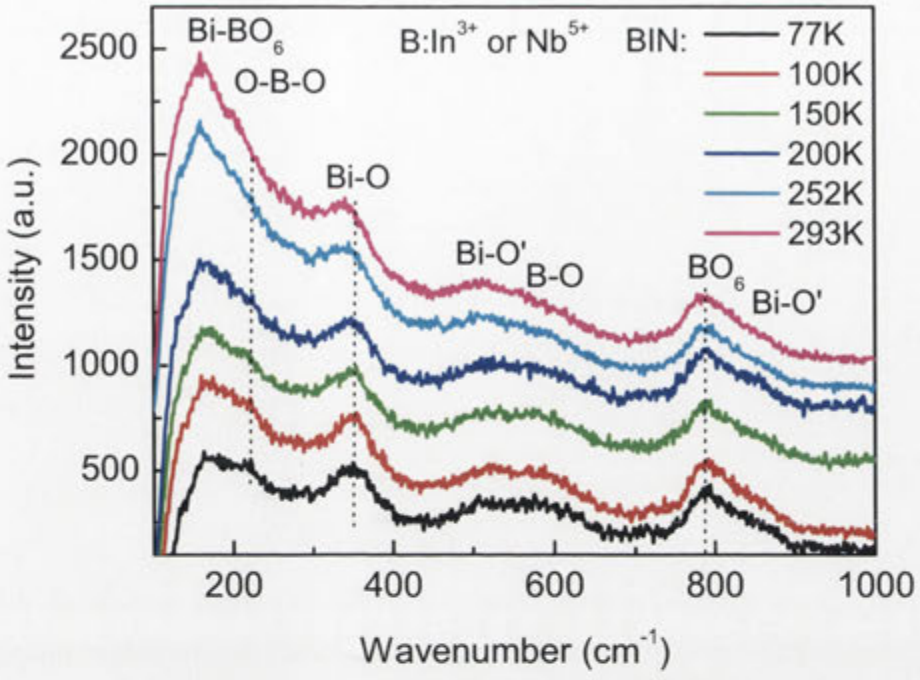

Figure 5-6 The temperature dependent micro-Raman spectra of the BIN sample collected from 77 K to 300 K.

5.4 Discussion

Despite similarities, an important difference in the dielectric relaxation behaviour of the *A* site stoichiometric, BIN and BSN, pyrochlores relative to that of the non-stoichiometric Bi-based pyrochlores is that the peak in the imaginary part of the dielectric permittivity as a function of frequency is shifted to higher temperatures in the cases of BIN and BSN *e.g.* T_m at 1 MHz = 225 K for BSN and 210 K for BIN but only 114 K for BMN, 133 K for BNN (see Chapter 4 above), 125 K for BFN [68], and ~ 110 K for BZN [65]. This is important in the context of the magnitude of the room temperature dielectric loss at RF/MW frequencies.

When the frequency dependence of the peak positions in the dielectric loss curves for BIN and BSN are modelled using the standard Arrhenius equation, completely unrealistic values are obtained *e.g.* an activation energy $E_a \sim 0.559$ eV (corresponding to a temperature of ~ 6481 K) and an attempt jump, or freezing, frequency $f_0 \sim 2.05\times10^{20}$ Hz in the case of BIN, significantly higher than the freezing frequency of both ionic lattice vibrations ($\sim 10^{13}$ Hz) as well as free electron

vibrations ($\sim 10^{16}$ Hz). Fitting using the Vogel-Fulcher equation gave no improvement. Following Cann *et al.* [21], the observed data were finally fitted via the relation:

$$f = f_0 \exp-(\frac{T_{Ea}}{T})^{zv} \qquad (5\text{-}1)$$

where $T_{Ea} = E_a/k$ and zv is a so-called dynamic scaling exponent [73,86] found to be ~2. Rather more reasonable activation energies, E_a, of 0.071 (0.072) eV and attempt jump frequencies of 6.48 (6.34) THz were then obtained for BSN and (BIN) respectively. Whether these particular values have any real physical meaning, however, is not at all clear.

As stated above, it is proposed that the intrinsically very low energy, correlated, chain rotation modes implied by the observed structured diffuse distribution and shown in Figure 4-7 provide an important key to understanding the structural origin of the dipoles as well as the glassy relaxation behaviour of these Bi-based pyrochlores. The near ubiquitous presence of essentially the same highly structured diffuse distribution in so many Bi-pyrochlores [69,77,78] supports this contention. At the very least, it means that the (random) hopping model [65,66,71,72] is quite untenable. It also strongly suggests that there is no direct, or causal, link between the chemical disorder and the existence of the dipole moments. In the case of β-cristobalite itself, it is known that there exist numerous very low frequency RUM modes (see *e.g.* Fig.2 of [85]) which give rise to a very similar structured diffuse distribution as that shown in Figure 5-3 and Figure 5-4 and that the low frequency dynamics of the β-phase are very similar to those found in network glasses [85,86,87]. In the case of the Bi-pyrochlores, it is clear that there also exist numerous very low, if not zero, frequency RUM-type modes.

5.5 Summary

In summary, it has been shown that *A* site stoichiometric, Bi_2InNbO_7 (BIN) and Bi_2ScNbO_7 (BSN), Bi-based niobate pyrochlores can indeed really exist, that the inherent β-cristobalite like structural disorder characteristic of so many Bi-based pyrochlores is also characteristic of BIN and BSN and that BIN and BSN also exhibit low temperature dielectric relaxation properties despite the absence of compositional disorder on the pyrochlore *A* site. It is proposed that the intergrowth of

the octahedral and β-cristobalite-like tetrahedral sub-structures in Bi-pyrochlores (see Figure 1-1) not only differentiates them from β-cristobalite itself, it also constrains the overall metric symmetry to remain cubic and hence prevents the onset of long range ferroelectric order. The "phase transition" represented by the low temperature, frequency-dependent peak in the dielectric loss (see Figure 5-5) is thus not a conventional phase transition (as is clear from the electron diffraction data shown in Figure 5-3 and Figure 5-4 as well as the temperature-dependent micro-Raman data of Figure 5-6) but rather a dynamic freezing or glass-like transition involving the slowing down of the 1-d dipolar dynamics of the PNR's.

Chapter 6: The Non-Bi based Pyrochlore - $Ca_{1.5}NbTi_{1.5}O_7$ (CNT)

In this chapter, the results of a primarily synthesis and dielectric properties investigation of a non-bismuth based, 'misplaced-displacive' cubic pyrochlore, namely $Ca_{1.5}NbTi_{1.5}O_7$ (CNT), are presented. A new metallorganic synthesis route to CNT is developed which significantly lowers the required synthesis temperature and enables a fully dense sample suitable for dielectric properties measurements to be obtained. It is thereby established that the presence of Bi on the pyrochlore A site is not required to obtain the low temperature dielectric relaxation properties characteristic of the inherently disordered Bi-based pyrochlore systems.

6.1 Introduction

The most common misplaced-displacive [20] cubic pyrochlore phases known to date are almost invariably Bi-containing phases with the general formula $(Bi_{1.5-\alpha}M_{0.5-\beta})(Nb_{1.5-\gamma}M_{0.5+\gamma})O_{7-\delta}$ (M = Zn^{2+}, Ni^{2+}, Fe^{3+}, Mg^{2+}, Co^{2+}, Mn^{2+},...) [15-18, 20,21,28,38,62,64,67,69,80]. The structure refinements of BMN, BNN reported in Chapter 4 and the other Bi-based pyrochlores to date [17,18,28,80] have all reported considerable displacive disorder associated with the $O'A_2$ (or $O'Bi_{1.5-\alpha}M_{0.5-\beta}$) sub-structure of the ideal $A_2B_2O_7$ (or $B_2O_6 \bullet O'A_2$) pyrochlore structure type (see Figure 4-3). The remaining B_2O_6, or $Nb_{1.5-\gamma}M_{0.5+\gamma}O_6$, sub-structure [18,28,64], by contrast, is typically found to be fully occupied and to exhibit very little displacive disorder. The apparently inherent compositional and displacive disorder of the $O'Bi_{1.5-\alpha}M_{0.5-\beta}$ sub-structure [18,38,64] is important to understand both from the fundamental point of view but also because it has been linked to the anomalous low temperature, glass-like dielectric relaxation behaviour observed in many of these systems [17,65].

Given that Bi has always been the dominant element on the A-site of these 'misplaced-displacive' pyrochlores, it might seem that the observed low temperature relaxor dielectric behaviour [15-18,28,38,62,64-67,69,80,] of these phases is inextricably linked to the presence of Bi (with its lone electron pair) on the pyrochlore A site. It is therefore important to look for a misplaced-displacive cubic pyrochlore phase that does not contain Bi on the pyrochlore A-site and to investigate its low temperature dielectric behaviour to see whether or not this is the case. This chapter presents the results of a synthesis and dielectric properties investigation of such a candidate phase, namely $Ca_{1.5}NbTi_{1.5}O_7$ (CNT).

6.2 Sample Preparation

The existence of a cubic pyrochlore phase in the ternary CaO-Nb_2O_5-TiO_2 system was first established via a careful phase equilibrium study by Jongjean and Wilkins [89]. They reported a cubic pyrochlore $Ca_{1.5}NbTi_{1.5}O_7$ (CNT) phase with a cubic lattice parameter of 10.15 Å, significantly smaller than the cubic lattice parameters characteristic of the Bi-based cubic pyrochlore phases. They also reported, however, that this CNT phase always melts during conventional solid state synthesis [89] making it difficult to obtain a fully dense sample suitable for dielectric

properties measurements. In addition, the sample needed to be quenched from quite high temperatures (> ~ 1275 °C) making it unsuitable for LTCC applications. The first target of this investigation therefore was to investigate whether or not an alternative wet chemical synthesis route to CNT could be developed which would enable rather lower annealing temperatures and denser resultant ceramic samples. As a result of the above considerations, a metallorganic decomposition (MOD) process to synthesise $Ca_{1.5}NbTi_{1.5}O_7$ was developed rather than the conventional solid state reaction process.

The description of this MOD process has already been presented in Section 2.2.2 of this thesis and will not be repeated again here suffice it to say that a final sintering temperature of only 1000 °C was required in order to achieve a well-crystallised, relatively dense single phase sample. This is much lower than the greater than 1275 °C annealing temperature reported by Jongjean and Wilkins [89]. A 1 mol. % CuO additive was also added to some preparations during the regrinding process to improve the sintering properties, increase the density (and reduce the porosity) of the resultant samples. The pellets with the 1 mol. % CuO additive (CNT1) showed 95 % density (relative to theoretical density), significantly higher than the 87 % density of the pellets without the CuO additive (CNT2).

6.3 Results and Discussion

6.3.1 X-ray Powder Diffraction Analyses

The obtained samples were carefully investigated via X-ray powder diffraction using a Guinier–Hägg camera and high purity Si powder as an internal standard. Both samples were found to be single phase, $Fd\bar{3}m$, cubic pyrochlores using a standard 2 hour exposure. The average structure unit cell dimension for both the CNT1 and CNT2 samples was a = 10.2171(3) Å, larger than the value of 10.15 Å which previously reported by Jongjean and Wilkins [89] (the observed reflections are given in Figure 6-1 and Table 6-1). The slight difference in lattice parameter suggests the existence of a narrow cubic pyrochlore solid solution field centred close to the nominal $Ca_{1.5}NbTi_{1.5}O_7$ composition of the CNT phase. This has recently been confirmed by a more recent phase analysis investigation [74]. Exposing for a much longer period of time (4 hours), a few very weak additional lines appeared in both

samples CNT1 and CNT2 which could not be indexed to the cubic pyrochlore CNT phase (denoted by the asterisks in Table 6-1) - indicating the presence of a trace amount of an unknown impurity phase.

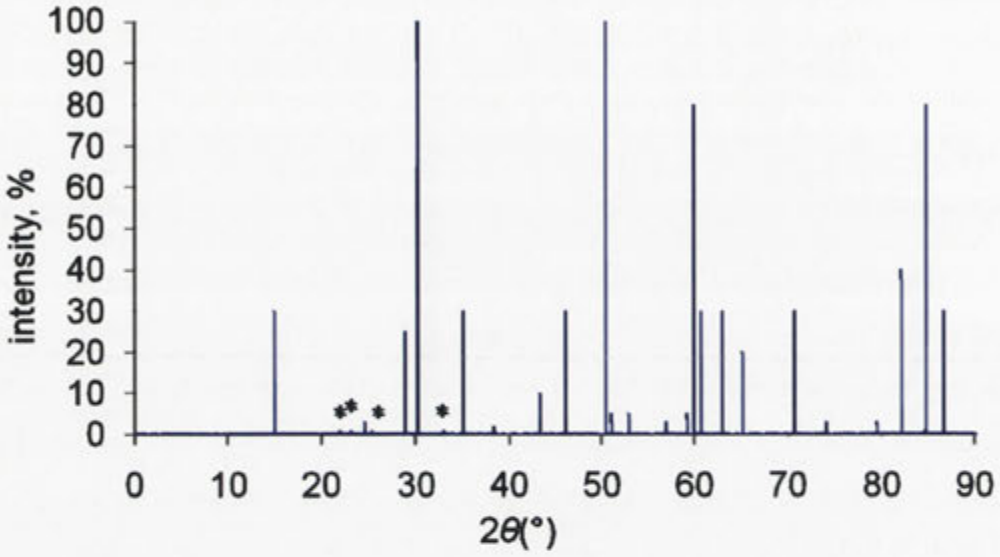

Figure 6-1 X-ray diffraction pattern of the CNT1 sample drawn from measured Guinier films and estimated intensities taken from Table 6-1 (* denotes four very weak lines belonging to an unknown second phase).

6.3.2 Electron Probe Microanalysis

Figure 6-2 shows a typical SEM micrograph of the as-synthesised CNT1 sample with the 1% CuO oxide additive. The sample is clearly quite dense, in agreement with the high resultant density directly measured. No second phase was apparent in the SEM micrographs. The grains are well crystallised and present a consistent grain boundary morphology, suggesting the formation of a single phase. The grain sizes are generally less than 5 μm. Small grains appear near the grain boundary regions, implying the growth mechanism of CNT is probably related to diffusion effects along the grain boundaries. Circular features are observed in the larger grains. This may arise from stress effects created when the small grains grow and come out from the grain boundary regions.

Table 6-1 The average structure of the cubic pyrochlore CNT1 phase was indexed to the ideal cubic pyrochlore $Fd\bar{3}m$ space group and the obtained unit cell is a = 10.2171(3) Å. Examination of heavily exposed Gunier XRD patterns indicated four very weak additional lines which could not be indexed to the CNT1 cubic pyrochlore phase (see the lines labelled with * in note). These lines were not visible on the standard two hour film exposures and only became visible when the *X*-ray film was exposed for more than four hours.

No.	*hkl*	$2\theta_{obs}$	$2\theta_{calc}$	$\Delta\theta$	d_{obs}	I_{obs}	Note
1	111	14.994	15.007	-0.013	5.9039	30	
2	--	21.965			4.0433	3	*
3	--	23.125			3.8431	5	*
4	022	24.635	24.625	0.010	3.6108	3	
5	--	25.348			3.5109	3	*
6	113	28.983	28.961	0.023	3.0782	25	
7	222	30.273	30.279	-0.006	2.9500	100	
8	--	32.996			2.7125	3	*
9	004	35.117	35.104	0.013	2.5534	30	
10	133	38.383	38.371	0.012	2.3433	2	
11	224	43.360	43.351	0.009	2.0851	10	
12	115, 333	46.131	46.127	0.004	1.9661	30	
13	044	50.489	50.489	-0.001	1.8062	100	
14	135	52.979	52.978	0.001	1.7270	5	
15	026	56.950	56.956	-0.006	1.6156	3	
16	335	59.263	59.258	0.005	1.5580	5	
17	226	60.009	60.013	-0.003	1.5404	80	
18	444	62.984	62.978	0.006	1.4746	30	
19	117, 155	65.152	65.151	0.001	1.4307	20	
20	137, 355	70.763	70.775	-0.011	1.3303	30	
21	008	74.193	74.190	0.003	1.2771	3	
22	066, 228	79.549	79.543	0.006	1.2040	3	
23	266	82.174	82.182	-0.008	1.1721	40	
24	048	84.800	84.804	-0.004	1.1424	80	
25	119, 357	86.754	86.764	-0.010	1.1216	30	

Note: * denotes four very weak lines belonging to an unknown second phase.

Given the presence of a trace amount of an unknown impurity phase in XRD, electron probe microanalysis (EPMA) was also performed to confirm the nominal $Ca_{1.5}NbTi_{1.5}O_7$ composition of the CNT, cubic pyrochlore phase. The analyses were carried out at 15 kV and 1nA using Zirconolite ($CaZrTi_2O_7$), TiO_2, NbO_2F as internal calibration standards. Both synthesised samples appeared to be homogenous with experimentally determined compositions of $Ca_{1.50(2)}Ti_{1.48(4)}Nb_{1.02(3)}O_7$, very close to the nominal composition of $Ca_{1.5}Nb_{1.0}Ti_{1.5}O_7$.

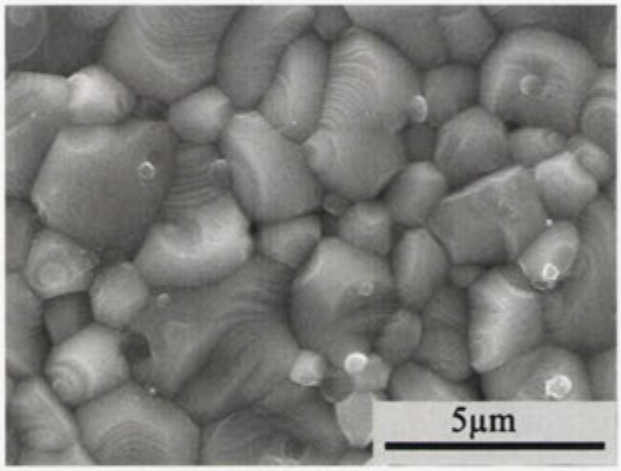

Figure 6-2. SEM morphologies of CNT compounds with and without CuO.

6.3.3 Dielectric Properties

The obtained CNT1 and CNT2 pellets were polished and coated with silver paste on both sides, followed by a heat treatment at 550 °C to ensure good electrical contact. The dielectric properties of the pellets were then measured using a high-precision LCR meter (Agilent 4284A). Figure 6-3 shows the measured room-temperature dielectric properties of both samples as a function of applied frequency. The measured dielectric constant of the CNT1 sample (with the 1 mol. % CuO additive) was slightly increased relative to that of the CNT2 sample while its measured dielectric loss was slightly decreased relative to that of the CNT2 sample. The measured dielectric permittivity of the CNT1 sample at room temperature and 100 kHz applied frequency was 103 and its corresponding dielectric loss 0.009, quite similar to the values found for BMN and BNN (see Chapter 4) as well as the reported dielectric properties of other Bi-based cubic pyrochlores [65,66,69].

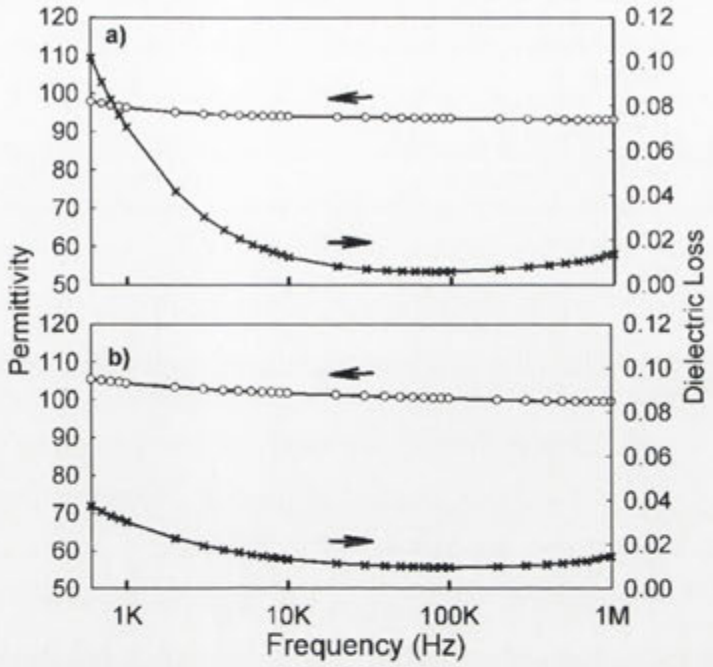

Figure 6-3 Room temperature dielectric constant and dielectric loss of the CNT compounds without (a) and with CuO additive (b) as a function of frequency.

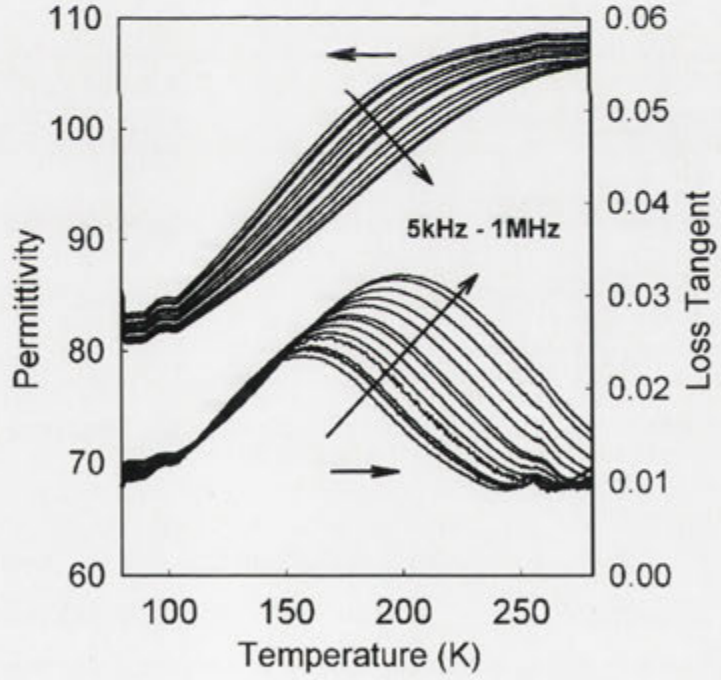

Figure 6-4 The measured dielectric permittivity and dielectric loss of the CNT1 sample as a function of temperature measured at frequencies from 5 kHz up to 1 MHz

Figure 6-4 shows the measured dielectric permittivity and dielectric loss of CNT1 as a function of both temperature and applied frequency. Frequency dispersive behaviour is clearly apparent in both the dielectric constant and dielectric loss spectra at temperatures lower than room temperature showing the relaxor dielectric behaviour of the Bi-based cubic pyrochlores is also characteristic of CNT without any Bi on the pyrochlore *A*-site. Note that the dielectric permittivity is relatively flat at higher temperatures but exhibits a steplike slowing down on lower temperature, as is also characteristic of the Bi-based 'misplaced-displacive' cubic pyrochlores [62,65,66,69,90].

Such behaviour is indicative of displacive motion requiring thermally activated hopping over a potential barrier which then freezes out at a sufficiently low temperature. Following a previous approach [65,66], the frequency dependence of the peak position in the dielectric loss curve (see Figure 6-4) was modelled using the basic Arrhenius type equation:

$$f_r = f_0 \exp(-\frac{Ea}{kT}) \qquad (6\text{-}1)$$

where:

f_r = measuring frequency

f_o = relaxation frequency at infinite temperature

E_a = represents an activation energy

k = Boltzmann constant

T = temperature of the peak position in the dielectric loss curve at the particular measuring frequency

This type of approach should be valid provided that the potential barrier is uniform for all hopping charges and that the charges hop independently of one another. In this case, the model failed leading to an unrealistic value for E_a of ~ 0.33eV (corresponding to a temperature of ~ 3844 K) and a freezing frequency f_0 of ~2.35×10^{14}Hz.

According to Nino *et al.* [66], this suggests that correlated hopping must be taken into account. The fitting to the observed data was therefore carried out using a modification to the above Arrhenius equation, namely the Vogel-Fulcher equation [65,66].

$$f_r = f_0 \exp(-\frac{Ea}{k(T-T_{vf})}) \qquad (6\text{-}2)$$

where:

T_{vf} = non-zero freezing temperature of the relaxation.

In this case, the fitted value for E_a was ~ 0.148 eV (corresponding to a temperature E_a/k ~ 1715 K), that for f_0 was 1.77 E_a and T_{vf} was 58 K (as shown in inset of Figure 6-5). This fitted value for E_a of 0.148 eV in the case of CNT is very close to the fitted value for E_a of 0.136 eV reported for the Bi-based pyrochlore BZN by Nino [66] using data collected over the same frequency range used in this study. Kamba *et al.* [65] reported an E_a of 0.20 eV for BZN obtained from measurements taken over an even broader frequency range. These results suggest a similar polarisation relaxation mechanism exists in both CNT and the Bi-based pyrochlore BZN. Finally, note that the T_{vf} of CNT of ~ 58 K is rather higher than the value of T_{vf} in the case of BZN (~25-30 K [91]). This is consistent with the fact that both the peak in the dielectric loss as well as the steplike variation of the dielectric constant in the case of CNT occur at significantly higher temperatures than they do in the case of BZN.

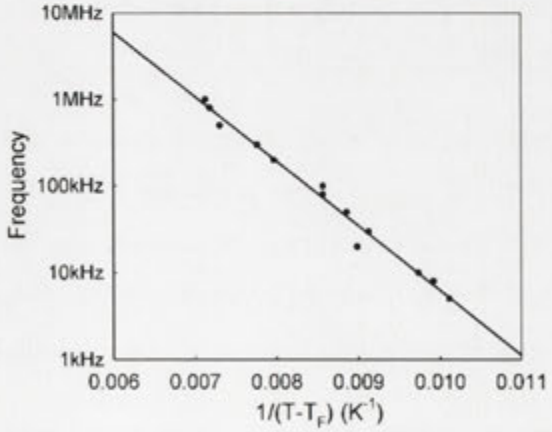

Figure 6-5 The measuring frequency as a function of 1/(T-T_f) obtained via fitting to the Vogel-Fulcher relation. T is the temperature of the peak position in the dielectric loss curve at the particular measuring frequency.

6.3.4 Local Crystal Chemistry

In order to attempt to obtain some insight into the local forces responsible for the relaxor dielectric behaviour shown in Figure 6-5, some understanding of the local crystal chemistry of the underlying $Fd\bar{3}m$ average structure of the $Ca_{1.5}Nb_1Ti_{1.5}O_7$ cubic pyrochlore phase is needed. Bond valence sum calculations [70,92] were thus again carried out based on an ideal $(Ca_{0.75}Ti_{0.25})_2(Ti_{0.50}Nb_{0.50})_2O_7$ cubic pyrochlore structure type with the *A* (or $Ca_{0.75}Ti_{0.25}$) ions on the 16*d* site at $^1/_2$, $^1/_2$, $^1/_2$; the *B* (or $Ti_{0.50}Nb_{0.50}$) ions on the 16*c* sites at 0, 0, 0; the O' ions on the 48*f* sites at x, $^1/_8$, $^1/_8$ and the O ions on the 8*b* sites at $^3/_8$, $^3/_8$, $^3/_8$. Note that all sites are fully occupied according to the EPMA determined composition. The only unknown fractional co-ordinate, the *x* fractional co-ordinate of O', can be readily estimated using the bond valence sum approach and the R_0 parameters listed in [93]. Given the average occupancies of the *B* sites, the expected average *B*–O bond length, R(*B*-O) should be such that:

$$AV(B) = 6 \times 0.5 \times \exp\{^{(1.815-R)}/_{0.37}\} + 6 \times 0.5 \times \exp\{^{(1.911-R)}/_{0.37}\} = 4.5 \quad \text{... (6-3)}$$

in the case of $(Ca_{0.75}Ti_{0.25})_2(Ti_{0.50}Nb_{0.50})_2O_7$. This occurs for R(*B*-O) = 1.9725 Å. Given the relation between R(*B*-O) and *x* as

$$R(B\text{-O}) = \sqrt{\{(x - {}^1/_4)^2 + 2\,({}^1/_8)^2\}} \times 10.2171 \text{ Å} \quad \text{(6-4)}$$

the value of *x* is predicted to be ~ 0.3276. (This is in rather good agreement with a value of 0.3237 reported for a closely related $Ca_{1.46}Nb_{1.11}Ti_{1.38}O_7$ sample reported very recently [74]).

With this choice of *x*, a bond valence sum calculation [89,92] was then carried out. As shown in Table 6-2, the octahedral Nb and Ti ions on the ideal pyrochlore *B*-site positions are then very close to being ideally bonded. The Ca ion on the ideal pyrochlore *A*-site, however, is significantly over-bonded (~ 18 %) and thus would not be expected to move off-centre by contrast with Bi-based pyrochlore phases in which the majority Bi ion on the *A*-site is invariably significantly under-bonded. Similarly to Bi-based pyrochlores, however, the minority (Ti) ion on the *A*-site is very significantly under-bonded (AV of 1.57 instead of 4). While the bond valence sum, or apparent valence (AV), of the O ions belonging to the octahedral

$(Ti_{0.50}Nb_{0.50})_2O_6$ sub-structure will obviously depend on the exact local *A* and *B* site distribution, it is nonetheless clear that they will be pretty happily bonded for most of the possible local configurations.

As for the Bi-based cubic pyrochlores, the disorder must clearly be primarily associated with the O'A_2 tetrahedral sub-structure. Table 6-3 shows the calculated AV of the O' ion depending upon the local stoichiometry of the surrounding A_4 tetrahedra. It is clear that the preferred local tetrahedral stoichiometry should be O'Ca_3Ti_1. Note that the Ca ion is significantly over-bonded in the pyrochlore *A*-site whereas the Ti ion is very significantly under-bonded. This suggests that the centreing O' ion in each O'Ca_3Ti_1 tetrahedron would want to move away from the Ca ions and towards the Ti ion. No evidence for this could be found in the form of structured diffuse scattering in electron diffraction patterns despite looking for it.

Table 6-2: Bond valence sums calculation for the cubic pyrochlore average structure of $(Ca_{0.75}Ti_{0.25})_2(Ti_{0.50}Nb_{0.50})_2O_7$ and apparent valences (AVs) for *O''* dependent upon local [A_4] stoichiometry

A	*B*	AV(*A*)	AV(*B*)	AV(O')	AV(O'')
Ca	Nb	2.367	5.081	2.139	2.063
Ca	Ti	2.367	3.92	1.752	2.063
Ti	Nb	1.570	5.081	1.989	1.368
Ti	Ti	1.570	3.92	1.602	1.368
	Ca_4	Ca_3Ti_1	Ca_2Ti_2	Ca_1Ti_3	Ti_4
AV(*O''*)	2.063	1.889	1.715	1.541	1.368

Table 6-3: Bond valence sums calculation for the cubic pyrochlore average structure of $(Ti_{0.75}Ca_{0.25})_2(Ca_{0.50}Nb_{0.50})_2O_7$.

A	*B*	AV(*A*)	AV(*B*)	AV(O)	AV(O')
Ti	Nb	2.345	3.238	1.633	1.368
Ti	Ca	2.345	3.767	1.810	1.368
Ca	Nb	3.537	3.238	1.915	2.063
Ca	Ca	3.537	3.767	2.091	2.063

6.4 Summary

In conclusion, a 'misplaced-displacive' $(Ca_{0.75}Ti_{0.25})_2(Ti_{0.50}Nb_{0.50})_2O_7$ (CNT) cubic pyrochlore without Bi on the pyrochlore *A* site has been successfully synthesised using a metallorganic (MOD) wet chemical process. This MOD process enables a much lower final annealing temperature to be used as well as resulting in a rather denser resultant ceramic sample. The resultant CNT samples were found to exhibit very similar low temperature relaxor dielectric behaviour to that found in BZN and other Bi-based cubic pyrochlore phases. This implies that the low temperature dielectric relaxation behaviour observed in Bi-based cubic pyrochlores is not solely due to the presence of Bi^{3+} with its lone electron pair. Unlike BZN, BMN or BNN, no evidence for structured diffuse scattering in electron diffraction patterns could be found to give insight into the nature of the local crystal chemistry in the case of CNT.

Chapter 7:

Synthesis and Dielectric Properties of the Non-stoichiometric $Ca_{1-x}Sm_{2x/3}TiO_3$

In this chapter, the synthesis as well as the relationship between local crystal structure, microstructure and dielectric properties of the (1-x)$CaTiO_3$.x$Sm_{2/3}TiO_3$ or $Ca_{1-x}Sm_{2x/3}TiO_3$ (CST, $0 \leq x \leq \sim 0.6$) system, are reported.

7.1 Introduction

For ceramic materials to be useful for microwave (MW) dielectric applications three major requirements need to be satisfied: a reasonably high dielectric constant ε_r (> ~50), a high quality factor ($Q \cdot f$) (~ 10,000 GHz) and a near-zero temperature coefficient of resonant frequency τ_f (< ~ 10-20 ppm /K) [56]. Increasing the dielectric constant, ε_r, enables the size of ceramic dielectric elements to be reduced as well as the overall size of the telecommunications devices containing them. Increasing the quality factor of dielectric resonators and filters improves the signal quality as well as providing more bandwidth on increasingly congested wireless systems. Improving the temperature stability of the dielectric properties of promising electroceramic materials has always been vital for the reliable operation of devices and systems. Ideally, the temperature coefficient of the resonant frequency (τ_f) should be as close as possible to zero. In practice, this is usually extremely difficult to achieve without significant degradation of one or other of the desired properties described above.

Obvious materials systems within which to search for such dielectric ceramics are titanate perovskite systems based on $BaTiO_3$, $SrTiO_3$ and $CaTiO_3$ [94-101]. Whilst $BaTiO_3$ has a very high dielectric constant, it also has a low $Q \cdot f$ value and a rather large τ_f. Given the need for all three desirable dielectric characteristics to co-exist simultaneously, $SrTiO_3$ and $CaTiO_3$-based systems are much better candidate materials systems from this point of view. $CaTiO_3$, for example, has both a high room temperature dielectric constant (~170) as well as a relatively high $Q \cdot f$ value (3,500 GHz) [102]. Its τ_f value (+850 ppm/K), however, is much too large [103-105]. The high initial starting dielectric constant of $CaTiO_3$ provides the possibility to tune its $Q \cdot f$ and τ_f values whilst still maintaining a sufficiently high value of ε_r. Various authors have attempted to tune the dielectric properties of $CaTiO_3$ by forming solid solutions of it with compounds such as the $ReAlO_3$'s (Re: rare earth element e.g. La^{3+}, Sm^{3+} and Nd^{3+}) [106-111] or, more recently, the $Re_{2/3}TiO_3$'s (Re = La^{3+}, Sm^{3+} and Nd^{3+}) [30,112-117]. The former systems tend to have too low a dielectric constant. The latter systems, however, have recently been reported to exhibit rather better dielectric properties that can be systematically varied with composition [118].

Kim *et al.*, for example, recently reported [30] the existence of a wide range non-stoichiometric, perovskite-related solid solution phase in the $Ca_{1-x}Sm_{2x/3}TiO_3$ system over the composition range of x from 0 up to 0.6 with dielectric properties that varied systematically as a function of composition. The dielectric constant, ε_r, was reported to systematically reduce with increasing x while the $Q \bullet f$ factor was reported to increase. In a subsequent follow-up paper [118], it was shown that the temperature coefficient of resonant frequency, ε_r, also reduced with increasing x suggesting that the $Ca_{1-x}Sm_{2x/3}TiO_3$, $0 \leq x \leq 0.6$, system is a promising dielectric system. The increased value of $Q \bullet f$ with increasing x was attributed by Kim et al [118] either to increased concentration of vacancies (labelled with the symbol □ in what follows) on the nominal perovskite A site and/or increased A site ordering associated with Sm^{3+} substitution. No evidence was reported, however, for any such A site and/or O/□ ordering in their paper. Note that the composition of the solid solution can be written in the general form $(Ca_{1-x}Sm_{2x/3}\square_{x/3})TiO_3$ if there are no oxygen vacancies and the Ti valence remains +4 across the solid solution.

The purpose of this chapter is to synthesise $Ca_{1-x}Sm_{2x/3}TiO_3$, $0 \leq x \leq 0.6$, (CST) samples to look for evidence of Ca/Sm/□ ordering via electron diffraction as well as to investigate the dielectric properties of the synthesised CST samples.

7.2 Experimental

Powder oxides of $CaCO_3$ (Hudson Laboratories, 99.999%), Sm_2O_3 (Aldrich, 99.9%) and TiO_2 (Aldrich, 99.9%) were used as starting materials in the solid state reaction route. They were first mixed at the nominal stoichiometry and then homogenized through grinding in an agate mortar under acetone for 30 minutes. The resultant mixture was dried and calcined in air at 850 °C overnight, then at 1200 °C for 24 hours using a Pt-crucible as the reaction vessel. The resultant powder from this process was then ground under acetone, dried and pressed into 12 mm diameter x 1 mm height pellets (for dielectric measurements) and sintered in air at 1300-1500 °C for a further day. The resultant pellets were finally re-ground, re-pelleted and sintered at the same temperature for a further 2 days. It was found that some of the obtained pellets had black and grey dots on the surface, suggesting a trace of Ti^{3+} formation due, presumably, to an insufficient oxygen atmosphere within the muffle

furnace at high temperature. Some samples were therefore also sintered in a 1 m long tube furnace under a (i) O_2 and (ii) 75% N_2+15% H_2 gas flow at 1450 °C for 72 hours to investigate the effect of an oxidising or reducing sintering environment on the resultant product.

7.3 Results and Discussions

7.3.1 Synthesis Conditions, Sintering, Density and Microstructure

All of the $Ca_{1-x}Sm_{2x/3}TiO_3$ (CST, x = 0.1-0.6) samples obtained via the above solid state reaction route had a dark yellow colour and a relative density greater than 92 % of theoretical density provided the final sintering temperature used was in the range 1350 °C to 1500 °C. Not surprisingly, the higher the sintering temperature the higher the density obtained as a result of grain growth and a decrease in the number of pores on increase of sintering temperature (see *e.g.* Figure 7-1). The average grain size was estimated from such SEM images to increase significantly from ~ 7 μm up to ~18 μm when the sintering temperature increased from 1350 °C up to 1450 °C. From 1450 °C to 1500 °C, there was only a slight further increase in average grain size noticeable. No obvious variation in average grain size and density with composition, x, was apparent from SEM micrographs of $Ca_{1-x}Sm_{2x/3}TiO_3$ ceramics prepared under the same synthesis conditions. Thus grain growth does not appear to be influenced by the amount of samarium in the solid solution but rather is primarily determined by the final sintering temperature. Similar behaviour has recently been reported for the $Ca_{1-x}Nd_{2x/3}TiO_3$ solid solution [113,119,120].

Samples sintered at the same temperature (1450 °C) in air and under an O_2 atmosphere (*cf. e.g.* Figure 7-2(a) and (b)) show well-defined crystalline faceting and similar densities and morphologies. The sample annealed at the same temperature under a reducing 75% N_2 + 15% H_2 atmosphere, however, showed a noticeable difference in its morphology (see Figure 7-2(c)) as well as a significant colour change (from yellow to black). The grains apparent in Figure 7-2(c) appear to have partially melted and the sample is clearly much more porous. Later XRD characterisation showed that the sample sintered in the reducing atmosphere had also changed structurally and was now a multi-phase sample.

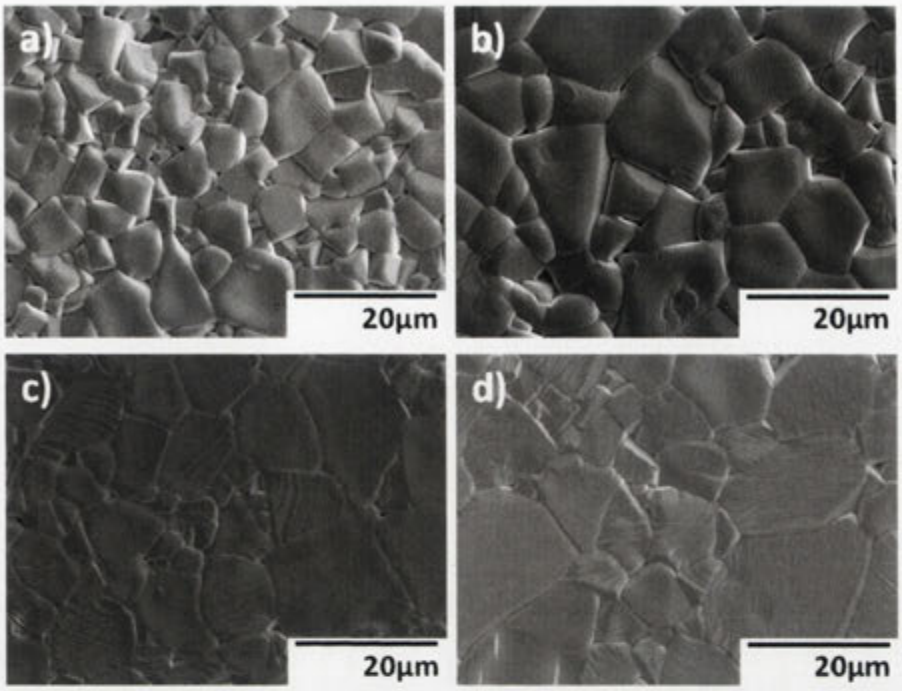

Figure 7-1 Secondary electron SEM images of the microstructures of thermally etched $Ca_{0.7}Sm_{0.2}TiO_3$ samples sintered for 3 hours at a) 1350 °C, b) 1400 °C, c) 1450 °C and d) 1500°C.

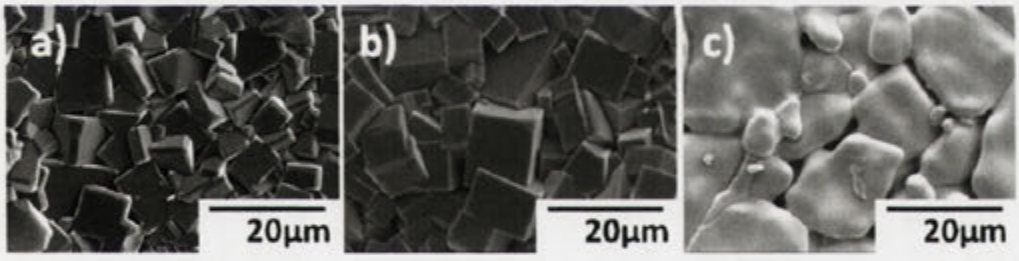

Figure 7-2 SEM images of a $Ca_{0.7}Sm_{0.2}TiO_3$ sample sintered at 1450 °C for 72 hours under (a) air, (b) O_2 and (c) a mixture of 75% N_2 + 15% H_2 environments.

7.3.2 Electron Probe Microanalysis

The nominal compositions of the synthesised samples were also confirmed via quantitative EPMA. Multiple spot analyses were carried out at 15 kV and 1 nA using zirconolite ($CaZrTi_2O_7$), titanium dioxide (TiO_2) and samarium pentaphosphate (SmP_5O_{14}) as internal calibration standards. The synthesised samples (with $x = 0.3$, sintered in air and O_2, see section 7.3.6.2), for example, were found to be homogenous (no visible secondary phases) with experimentally determined

compositions of $Ca_{0.69(0.01)}Sm_{0.21(0.01)}TiO_3$, (arbitrarily normalized to three oxygens), in excellent agreement with the nominal composition $Ca_{0.7}Sm_{0.2}TiO_3$ *i.e.* composition control during the sintering process was not a problem for this particular ceramic system. The quoted error bars represent the standard deviation from 40 separate spot analyses used to obtain the quoted average compositions.

7.3.3 X-ray Powder Diffraction

X-ray powder diffraction patterns of the CST samples sintered at 1450 °C for 3 hours in air and oxygen were all single phase for compositions from $x = 0.1$ to $x = 0.6$ and quite similar to those reported for the end-member compound, $CaTiO_3$ (ICDS card file number #42-0423 [121]. Note that these reported unit cell dimensions are used for the end-member $x = 0$ compound in the plots drawn below). The unit cell dimensions of the samples were all indexed to a $\sqrt{2}a_p$ x $2a_p$ x $\sqrt{2}a_p$ (subscript p for parent perovskite sub-structure) orthorhombic phase with space group symmetry *Pnma* (see Figure 1-3 above). This space group symmetry was confirmed by electron diffraction (see Section 7.3.4 below). Figure 7-3 shows a typical X-ray powder diffraction pattern of the $x = 0.3$, $Ca_{0.7}Sm_{0.2}TiO_3$ (sintered at 1450 °C for 3 hours) sample while Table 7-1 lists the indexation of this particular powder diffraction pattern.

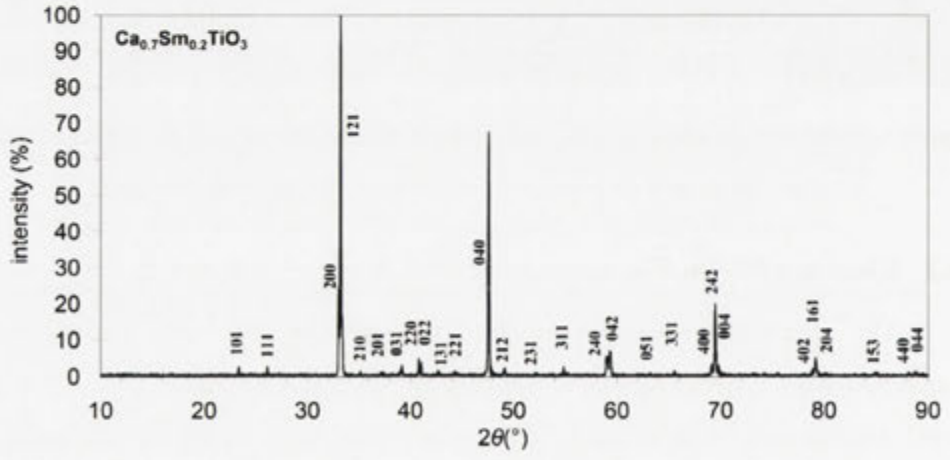

Figure 7-3 X-ray powder diffraction pattern (taken on a Siemens D-5000 diffractometer) of the $x = 0.3$, CST1 sample sintered at 1450 °C for 3 hours.

Table 7-1: X-ray powder diffraction data for $Ca_{0.7}Sm_{0.2}TiO_3$ sample sintered at 1450 °C for 3 hours (space group #62 *Pnma* a=5.426(2) Å,b= 7.644(2) Å,c=5.394(2) Å, V= 223.71(2) Å^3)

No.	h	k	l	$2\theta_{obs}$	$2\theta_{calc}$	$\Delta\theta$	d_{obs}	I_{obs}(%)
1	1	0	1	23.397	23.254	-0.143	3.799	2.3
2	1	1	1	26.131	26.046	-0.085	3.407	2.4
3	2	0	0	33.050	32.982	-0.068	2.708	24.7
4	1	2	1	33.210	33.258	0.048	2.696	100.0
5	2	1	0	35.139	35.063	-0.076	2.552	1.3
6	2	0	1	37.113	37.070	-0.043	2.420	0.9
7	1	0	2	37.312	37.257	-0.054	2.408	1.1
8	2	1	1	39.027	38.961	-0.066	2.306	1.5
9	0	3	1	39.189	39.140	-0.049	2.297	3.0
10	2	2	0	40.801	40.751	-0.050	2.210	4.6
11	0	2	2	41.050	40.982	-0.068	2.197	3.8
12	1	3	1	42.681	42.621	-0.060	2.117	1.5
13	2	2	1	44.261	44.225	-0.036	2.045	1.2
14	1	2	2	44.393	44.387	-0.006	2.039	1.0
15	0	4	0	47.601	47.541	-0.059	1.909	67.5
16	2	3	0	49.073	49.010	-0.063	1.855	1.7
17	2	1	2	49.139	49.100	-0.039	1.853	1.7
18	2	3	1	52.083	52.049	-0.034	1.755	0.7
19	1	0	3	53.893	53.758	-0.135	1.700	0.6
20	3	1	1	54.820	54.821	0.001	1.673	2.5
21	1	1	3	55.222	55.189	-0.033	1.662	0.9
22	3	2	1	58.980	58.992	0.011	1.565	5.4
23	2	4	0	59.100	59.092	-0.008	1.562	4.3
24	0	4	2	59.349	59.343	-0.006	1.556	6.7
25	0	5	1	63.219	63.256	0.037	1.470	0.7
26	3	3	1	65.549	65.572	0.023	1.423	1.3
27	4	0	0	69.158	69.183	0.025	1.357	3.1
28	2	4	2	69.510	69.520	0.010	1.351	19.9
29	0	0	4	69.857	69.827	-0.030	1.345	2.9
30	4	0	1	71.861	71.673	-0.188	1.313	0.5
31	3	1	3	75.548	75.608	0.059	1.258	0.9
32	4	0	2	78.890	78.954	0.064	1.212	1.7
33	1	6	1	79.161	79.215	0.055	1.209	5.0
34	2	0	4	79.445	79.415	-0.030	1.205	1.3
35	3	5	1	85.008	84.930	-0.078	1.140	0.7
36	1	5	3	85.206	85.233	0.027	1.138	0.8
37	4	4	0	88.092	88.269	0.178	1.108	0.8
38	0	4	4	88.829	88.872	0.043	1.101	1.2

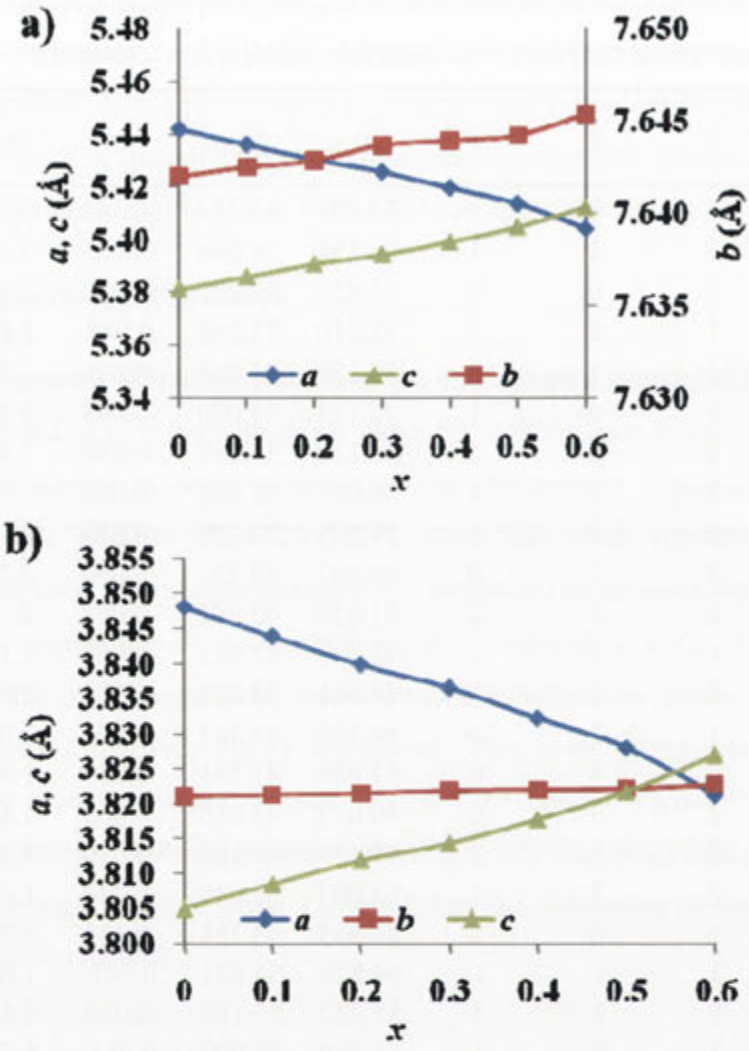

Figure 7-4 The (a) refined, (b) reduced unit cell dimensions of the orthorhombic *Pnma*, $Ca_{1-x}Sm_{2x/3}TiO_3$ (x = 0 - 0.6) samples sintered at 1450 °C for 3 hours as a function of composition x.

The refined unit cell dimensions, as well as the reduced unit cell dimensions $a/\sqrt{2}$, $b/2$ and $c/\sqrt{2}$, of the synthesised $Ca_{1-x}Sm_{2x/3}TiO_3$ (CST, x = 0.1 to 0.6) samples are shown plotted in Figure 7-4a and b as a function of composition x. Note that the refined b and c axis dimensions increase systematically with composition x while the a axis dimension systematically decreases until the a and c axis dimensions cross over close to x = 0.6 (see Figure 7-4a). Note also that there is a clear trend towards tetragonal, if not cubic, metric symmetry as the Sm^{3+} content increases (see Figure 7-4b). There is also a small but systematic gradual decrease of the unit cell volume with x, presumably a result of the slightly smaller ionic radii of Sm^{3+} (1.24 Å, [122]) relative to that of Ca^{2+} (1.34 Å, [122]). This slightly smaller ionic radii of the Sm^{3+}

ion relative to the Ca^{2+} ion suggests that the magnitude of the octahedral rotation around the resultant **a** and **b** axes (see Figure 1-3 above) should if anything increase slightly rather than reduce upon increasing Sm^{3+} content *i.e.* the observed trend towards cubic metric symmetry on increasing Sm^{3+} content cannot be attributed to a reduction in the magnitude of the $a^-b^+a^-$ octahedral rotations around the resultant **a** and **b** axes (see *e.g.* Figure 1-3 above) on increasing Sm^{3+} content.

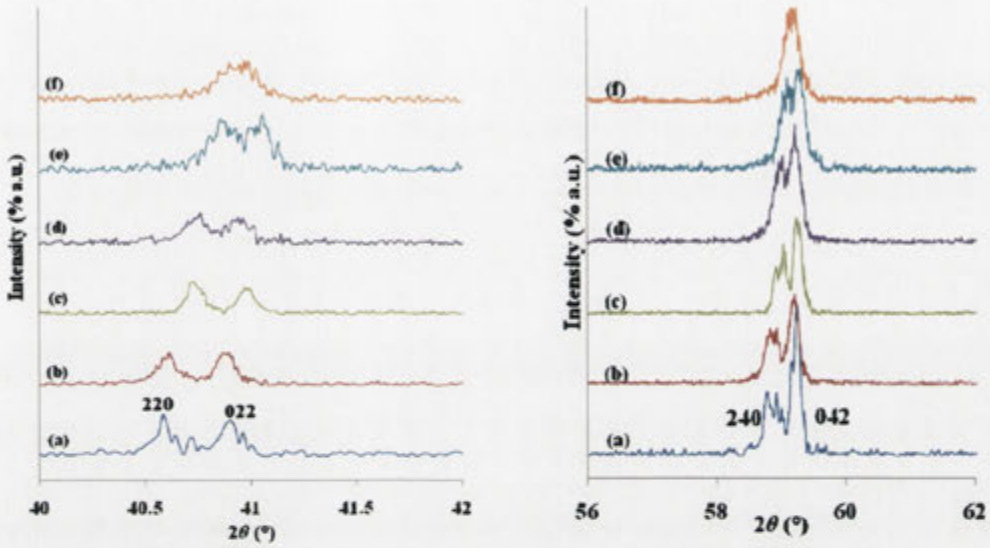

Figure 7-5 Expanded view of the (a) 220/022 and (b) 240/042 doublet regions in XRPD patterns of the CST samples sintered at 1450 °C for 3 hours as a function of composition ((a) x = 0.1, (b) x = 0.2, (c) x = 0.3, (d) x = 0.4, (e) x = 0.5, (f) x = 0.6), showing the clear tendency for merging of the two peaks in the doublets into a single peak as x increases.

Figure 7-5 above shows an expanded view of the profiles of the (220), (022) and (240), (042) peak doublets in the powder XRD patterns of CST samples (x = 0.1 - 0.6) sintered at 1450 °C for 3 hours. The tendency of the two initially split peaks to merge into a single peak as the amount of Sm^{3+} substitution increases is clearly apparent as is the systematic shift toward higher 2θ angle of the diffraction peaks, and hence the systematic reduction in unit cell volume, with increasing Sm^{3+} content. The merging of the initially split diffraction peaks indicates that the metric symmetry of the underlying perovskite parent structure tends towards cubic as x increases.

7.3.4 Electron Diffraction

Single domain electron diffraction patterns (EDP's) of the CST samples (see *e.g.* Figure 7-6 and Figure 7-7 below) were as expected and entirely consistent with a *Pnma*, $\sqrt{2}a_p$ x $2a_p$ x $\sqrt{2}a_p$ ($\mathbf{a} = \mathbf{a}_p - \mathbf{c}_p$, $\mathbf{b} = 2\mathbf{b}_p$, $\mathbf{c} = \mathbf{a}_p + \mathbf{c}_p$; $\mathbf{a}^* = {}^1/_2\,[1,0,-1]_p^*$, $\mathbf{b}^* = {}^1/_2\,[010]_p^*$, $\mathbf{c}^* = {}^1/_2\,[101]_p^*$, subscript p for parent perovskite sub-structure) average crystal structure except for the presence of weak diffuse blobs of intensity (diffuse 'satellite reflections') at the $G \pm {}^1/_2\,[100]_p^*$ and $G \pm {}^1/_2\,[001]_p^*$ regions of reciprocal space (arrowed in Figure 7-6c, d, e and f) which became more and more apparent as the Sm^{3+} content increases (*cf. e.g.* Figure 7-6 with Figure 7-7). Note that the *n* and *a* glide extinction conditions characteristic of *Pnma* space group symmetry, $F(0kl) = 0$ unless $k+l$ even and $F(hk0) = 0$ unless $h+k$ even, are clearly obeyed (see *e.g.* Figure 7-6a and b).

Figure 7-6, for example, shows typical (a) [100], (b) [001], (c) [010], (d) <-1,0,1>, (e) <1,1,-1> and (f) <0,-1,6> zone axis EDP's of the $x = 0.6$, $Ca_{0.4}Sm_{0.4}TiO_3$, sample indexed both with respect to the parent perovskite sub-structure (labelled with the subscript p) as well as with respect to the resultant *Pnma*, $\sqrt{2}a_p$ x $2a_p$ x $\sqrt{2}a_p$ crystal structure. Figure 7-7 shows (a) [-1,0,1] and (b) [010] zone axis EDP's of the $x = 0.2$, $Ca_{0.8}Sm_{0.133}TiO_3$, sample again indexed both with respect to the parent perovskite sub-structure (labelled with the subscript p) as well as with respect to the resultant *Pnma*, $\sqrt{2}a_p$ x $2a_p$ x $\sqrt{2}a_p$ crystal structure.

Note that the $\mathbf{G} \pm {}^1/_2 \langle 111 \rangle_p^*$ superlattice reflections associated with octahedral rotation around **a** (see *e.g.* the reflection labelled 011 in Figure 7-6a; see also Figure 1-3a above), the $\mathbf{G} \pm {}^1/_2\,[101]_p^*$ superlattice reflections associated with octahedral rotation around **b** (see *e.g.* the reflection labelled 001 in Figure 7-6a and

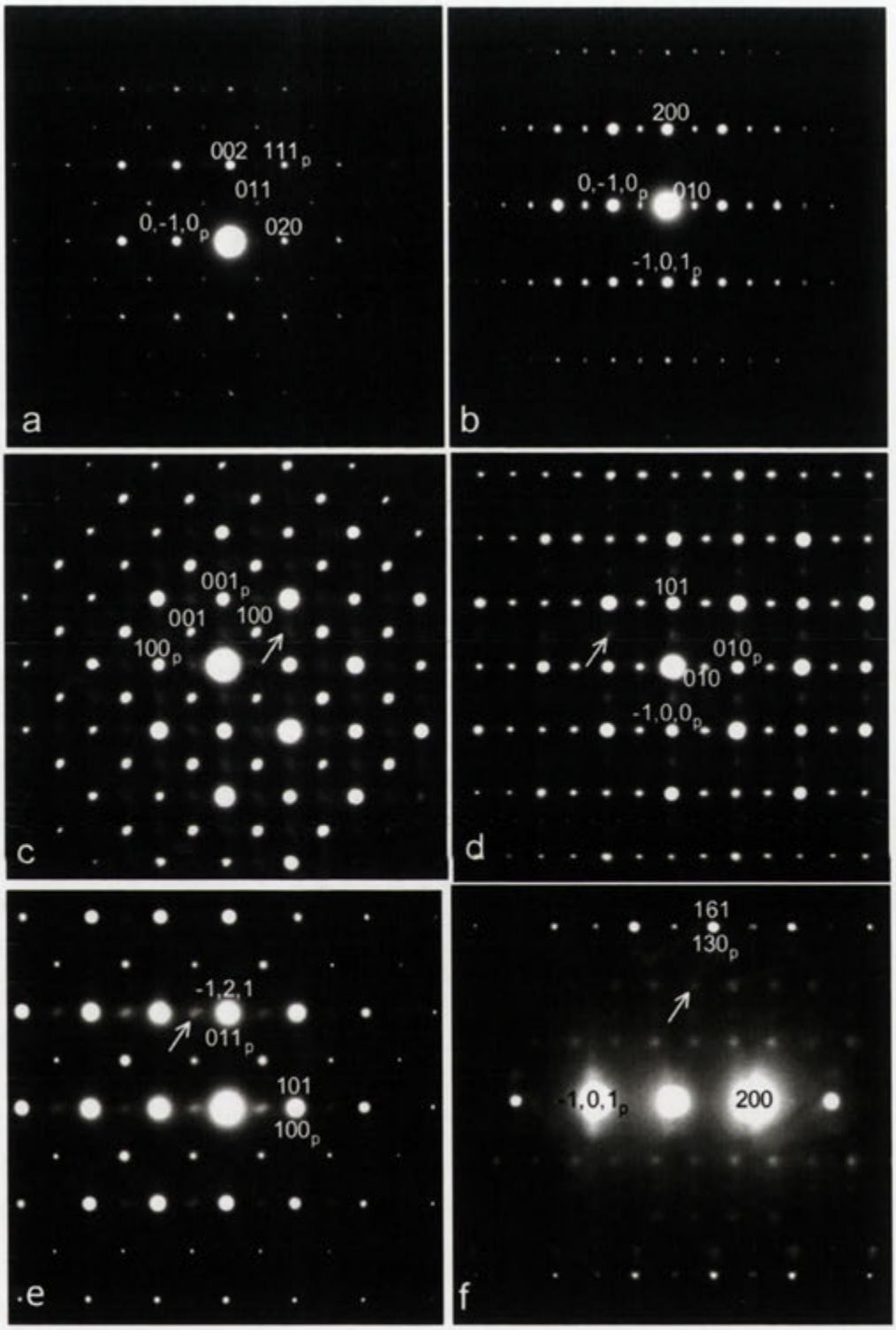

Figure 7-6 Typical (a) [100], (b) [001], (c) [010], (d) <-1,0,1>, (e) <1,1,-1> and (f) <0,-1,6> zone axis EDP's of the x = 0.6, $Ca_{0.4}Sm_{0.4}TiO_3$, sample indexed both with respect to the parent perovskite sub-structure (labelled with the subscript p) as well as with respect to the resultant *Pnma*, $\sqrt{2}a_p \times 2a_p \times \sqrt{2}a_p$ crystal structure.

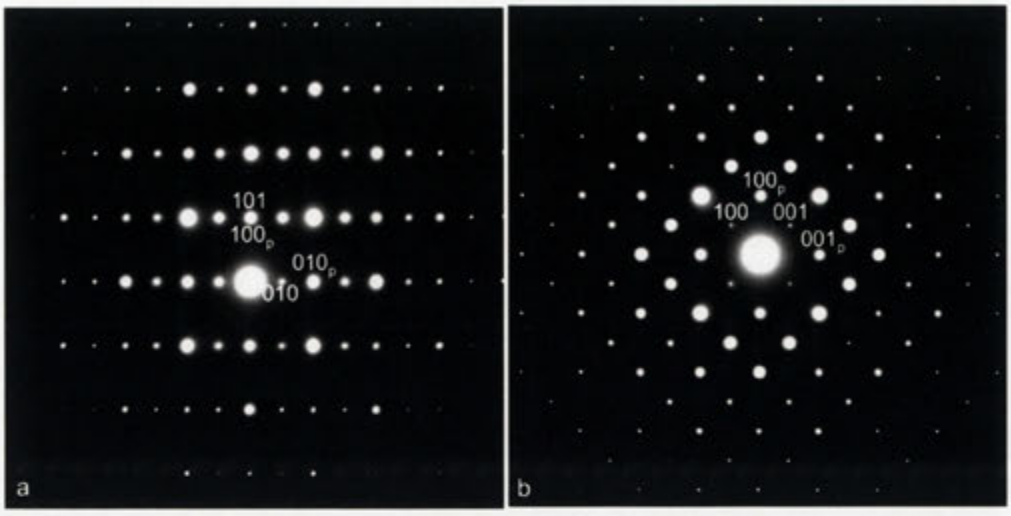

Figure 7-7 shows typical (a) [-1,0,1] and (b) [010] zone axis EDP's characteristic of the $Ca_{0.80}Sm_{0.133}TiO_3$ (x = 0.2) sample.

Figure 7-7b; see also Figure 1-3b above) as well as the $\mathbf{G} \pm {}^1/_2\,[010]_p^*$ superlattice reflections associated with correlated Ca, and Sm, displacements along **a** (see *e.g.* the reflection labelled 010 in Figure 7-6d and Figure 7-7a; see also Figure 1-3b above) remain quite sharp right across the solid solution field by contrast with the diffuse 'satellite reflections' at the $\mathbf{G} \pm {}^1/_2\,[100]_p^*$ and $\mathbf{G} \pm {}^1/_2\,[001]_p^*$ positions of reciprocal space (arrowed in Figure 7-6). This would seem to rule out the possibility of superlattice twinning being responsible for the existence of these weak diffuse "satellite reflections" and suggests that the real space modulation/s responsible for these weak diffuse satellite reflections must have some other structural origin such as, for example, $Ca^{2+}/Sm^{3+}/\square$ ordering in the average perovskite *A* site and associated structural relaxation.

The diffuse character of these $\mathbf{G} \pm {}^1/_2\,[100]_p^*$ and $\mathbf{G} \pm {}^1/_2\,[001]_p^*$ 'satellite reflections' furthermore suggests that any such ordering can only be short range ordered, on something like a 5-10 nm or so scale (note that this is only an estimate) and considerably shorter than the scale associated with the essentially long range ordered *Pnma* average structure (see *e.g.* Figure 1-3 above). High-resolution transmission electron microscopy (HRTEM) lattice images were therefore sought and obtained (courtesy of Dr. John Barry and the Electron Microscope Unit of the University of Queensland) in order to see if any further information could be obtained as to the structural origin of the weak diffuse "satellite reflections" (see *e.g.*

the [-1,1,1] zone axis HRTEM image of the $Ca_{0.4}Sm_{0.4}TiO_3$ sample shown in Figure 7-8 below).

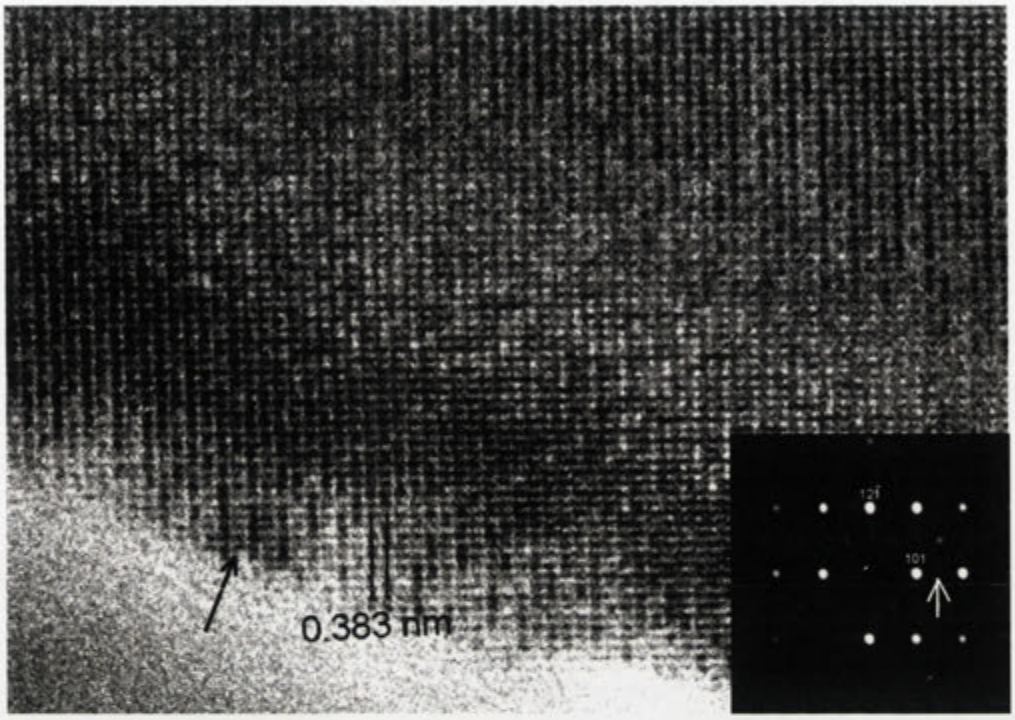

Figure 7-8 HRTEM image down the [-1,1,1] zone axis of a $Ca_{0.4}Sm_{0.4}TiO_3$ (x = 0.6, sintered at 1450 °C for 3 hours) crystal (HRTEM image courtesy of Dr. John C Barry). The corresponding EDP is inset.

Figure 7-8 shows a HRTEM image taken down the [-1,1,1] zone axis of a $Ca_{0.4}Sm_{0.4}TiO_3$ (x = 0.6, sintered at 1450 °C for 3 hours) sample. The corresponding EDP (from a rather larger area) is shown inset (*cf. e.g.* with Figure 7-6e). Note that $[101]^* = [100]_p^*$ and that there are rather weak diffuse blobs at the $\mathbf{G} \pm {}^1/_2[100]_p^*$ positions of reciprocal space (one of which is arrowed in the inset EDP). The real space reason for this can be seen on the very thin crystal edge in the HREM image *i.e.* a locally doubled periodicity with alternating dark and light fringes (arrowed) tentatively associated with $Sm^{3+}/\square$ vacancy rich A-type $(100)_p$ layers alternating with Ca^{2+} rich A type layers. Such layered ordering is characteristic of other A-site deficient and/or doped perovskites (see *e.g.* Zhou *et al.*, 2008 [123] and references contained therein). It is difficult to go further, however, without much more detailed HRTEM work including image matching, well beyond the scope of this thesis. Why this layered ordering should only have short range order, however, is not immediately apparent.

7.3.5 Local Crystal Chemistry

In order to attempt to obtain additional insight into the local crystal chemistry and hence the structural origin of the diffuse "satellite reflections", the bond valence sum based program *SpuDS* [124] was used in order to predict (give a reasonable idea of) the crystal structure of the $Ca_{1-x}Sm_{2x/3}TiO_3$ samples as a function of composition, x. *SpuDS* [124] was developed to predict the crystal structures of perovskites such as CST. It calculates the optimal structure in ten different Glazer tilt systems [124] (including the relevant $a^-b^+a^-$ tilt system operable in CST, see *e.g.* Figure 1-3) by minimization of the so-called Global instability Index. For further details on how the program works and the assumptions it makes, see [125].

Table 7-2 *SPuDS* [124] predicted orthorhombic *Pnma* unit cell dimensions and corresponding octahedral tilt angles of $Ca_{1-x}Sm_{2x/3}TiO_3$ at x = 0, 0.1, 0.3 and 0.6.

x	0	0.1	0.3	0.6
Composition	$CaTiO_3$	$Ca_{0.9}Sm_{0.067}TiO_3$	$Ca_{0.7}Sm_{0.2}TiO_3$	$Ca_{0.4}Sm_{0.4}TiO_3$
Tilt angle	14.60°	14.77°	15.13°	15.59°
Lattice parameters				
a (Å)	5.4987	5.4974	5.4944	5.4906
b (Å)	7.6881	7.6840	7.6753	7.6637
c (Å)	5.3784	5.3743	5.3653	5.3534

Table 7-2 above shows the *SpuDS* [124] predicted octahedral tilt angles, fractional co-ordinates and unit cell dimensions for the x = 0, 0.1, 0.3 and 0.6 samples while Table 7-3 shows the corresponding predicted fractional co-ordinates and Table 7-4 shows the bond valence sums, or Apparent Valences (AV's), calculated by *SPuDS* for each of the constituent cations and anions for comparison with the nominally ideal valences. Note that the tilt angle listed in Table 7-2 refers to the magnitude of the octahedral tilt around the resultant b direction (see Figure 1-3b) while the predicted tilt angle around the resultant a (or $[1,-1,0]_p$) direction (see Figure 1-3a) is $\sqrt{2}$ times this angle. As expected, note that the octahedral tilt angles are predicted to slightly increase, rather than decrease, with increasing Sm^{3+} content.

Figure 7-9 shows the SpuDS predicted variation in the *Pnma* unit cell dimensions as a function of composition, x, for comparison with the experimentally refined values shown in Figure 7-4a.

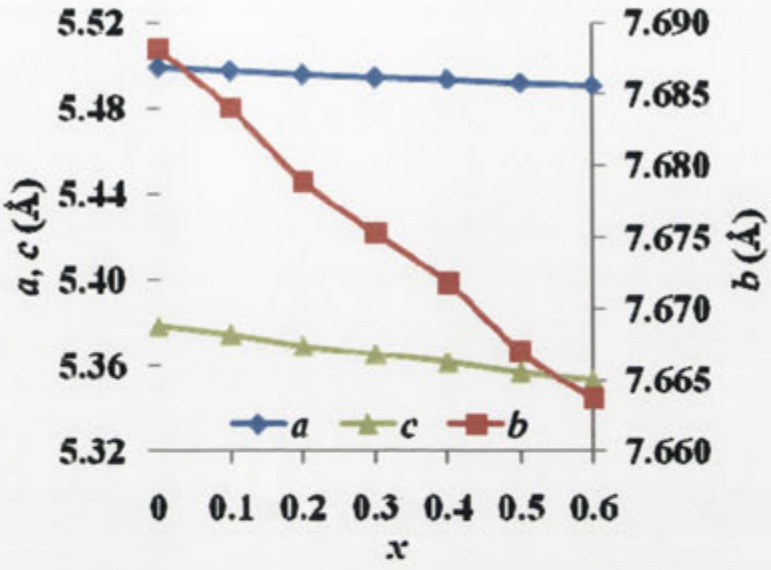

Figure 7-9 The SPUDS [124] predicted of the orthorhombic Pnma, $Ca_{1-x}Sm_{2x/3}TiO_3$ (x = 0 - 0.6) samples sintered at 1450 °C for 3 hours as a function of composition x.

While the AV's in Table 7-4 below are quite reliable for the cations (assuming the *SPuDS* predicted structures), the AV's calculated for the oxygen anions are somewhat misleading in that they are calculated under the assumption that each oxygen anion is surrounded by 2 Ti cations and 4 times the average number of *A* site cations *i.e.* (4-4x) Ca ions, $^{8x}/_{3}$ Sm cations and $^{4x}/_{3}$ vacancies. (Each oxygen anion has 4 nearest neighbour *A* sites lying on a particular $\{001\}_p$ plane, see *e.g.* Figure 1-3). *SPuDS* averages the bond valence parameters [125] used to calculate the AV's accordingly. On a local scale, however, each *A* site ion can only be either a Ca ion, a Sm ion or a vacancy. It is thus necessary to re-calculate the oxygen AV's as a function of the local *A* site co-ordination. When this is done for the x = 0.3 sample, for example, (see Table 7-5 and Table 7-6 below) it becomes apparent that both oxygen ions are quite happily bonded if co-ordinated by 2 Ti ions and 4 Ca ions but significantly over-bonded (by ~ 0.3 valence units, vu's) if surrounded by 2 Ti ions and 4 Sm ions.

Table 7-3 The *SPuDS* predicted fractional coordinates of the orthorhombic *Pnma*, structures of $Ca_{1-x}Sm_{2x/3}TiO_3$ at x = 0, 0.1, 0.3 and 0.6.

Atom	Site	x	Occupancy	x	y	z
Ca	4c	0.0	1	0.5344	0.25	0.5108
		0.1	0.90	0.5354	0.25	0.5112
		0.3	0.7	0.5373	0.25	0.5119
		0.6	0.4	0.5399	0.25	0.5129
Sm	4c	0.0	0			
		0.1	0.07	0.5354	0.25	0.5112
		0.3	0.2	0.5373	0.25	0.5119
		0.6	0.4	0.5399	0.25	0.5129
Ti	4b	0.0	1	0.5	0	0
		0.1	1	0.5	0	0
		0.3	1	0.5	0	0
		0.6	1	0.5	0	0
O1	4c	0.0		-0.0108	0.25	0.4248
		0.1		-0.0111	0.25	0.4239
		0.3		-0.0116	0.25	0.4219
		0.6		-0.0123	0.25	0.4195
O2	8d	0.0		0.286	0.0376	0.7124
		0.1		0.2864	0.0381	0.7119
		0.3		0.2872	0.039	0.711
		0.6		0.2883	0.0403	0.7097

Table 7-4 The *SPuDS* calculated bond valence sums (*AV*'s) of CST's at x = 0, 0.1, 0.3 and 0.6.

x		0	0.1	0.3	0.6
Formula		$CaTiO_3$	$Ca_{0.90}Sm_{0.067}TiO_3$	$Ca_{0.70}Sm_{0.20}TiO_3$	$Ca_{0.40}Sm_{0.40}TiO_3$
Atom (site)	AV_{ideal}	AV_{cal}	AV_{cal}	AV_{cal}	AV_{cal}
Ca(4c)	2	1.9998	2.0172	2.055	2.1051
Sm(4c)	3		2.7976	2.85	2.9195
Ti(4b)	4	4	4	4	4
O(4c)	2	2.0038	2.0082	2.0084	2.0089
O(8d)	2	1.998	2.0016	2.0001	2.0005

Table 7-5 AV contributions to the O[4c] oxygen anion from the 4 surrounding *A* cations using the *SpuDS* predicted $Ca_{0.7}Sm_{0.2}TiO_3$ structure.

d(O[4c]-A)	AV (if Ca^{2+})	AV (if Sm^{3+})
2.343 Å	0.362	0.502
2.5251	0.221	0.307
3.050	0.054	0.074
3.054	0.053	0.073
AV{O(4c)[A_4Ti_2]}	2.023	2.290

The quickest way to reduce this significant over-bonding is to remove the contribution of one or other of the locally closest Sm^{3+} ions by the introduction of a vacancy *i.e.* the local crystal chemistry suggests that the Sm^{3+} ions and the vacancies will tend to cluster together into $\{001\}_p$ type layers *i.e.* oxygen ions that are bonded to Sm^{3+} ions will tend to be over-bonded and hence also prefer one or more oxygen vacancies whereas the Ca^{2+} ions will prefer their own company and thus cluster together into alternate $\{001\}_p$ layers. The easiest way to achieve this is to attempt to order the Ca's and Sm/vacancies into Ca-rich and Sm/vacancy rich $\{001\}_p$ layers. The above discussion is by no means conclusive but it is felt does provide some crystal chemical justification for the short range ordering observed experimentally. The effect of such short compositional ordering on the measured dielectric properties is now discussed.

Table 7-6 AV contributions to the O[8*d*] oxygen anion from the 4 surrounding *A* cations using the *SpuDS* predicted $Ca_{0.7}Sm_{0.2}TiO_3$ structure.

d(O[8*d*]-*A*)	AV (if Ca^{2+})	AV (if Sm^{3+})
2.3774 Å	0.330	0.457
2.5920	0.185	0.256
2.6982	0.139	0.192
3.2719	0.029	0.041
AV{O(4*c*)[A_4Ti_2]}	1.987	2.280

7.3.6 Dielectric Properties

7.3.6.1 Effect of Sm^{3+} Substitution

Figure 7-10 below shows a plot of the frequency dependence (from 1 kHz up to 1 MHz, on a logarithmic horizontal scale) of the measured dielectric constants and dielectric losses of the CST (x = 0.1-0.6) samples sintered at 1450 °C for 3 hours. Both were largely frequency independent over the measured frequency range. The dielectric constants, however, vary significantly with composition at all frequencies. Figure 7-11, for example, shows a plot of the room temperature variation in dielectric constant and dielectric loss at an applied frequency of 1 MHz as a function

of composition, x. Given that the relative densities of the CST samples were all quite high and very similar, it is clear that the measured behaviour shown in Figure 7-11 is not strongly affected by the relative densities of the samples but rather reflects the intrinsic composition dependence of the dielectric properties of CST.

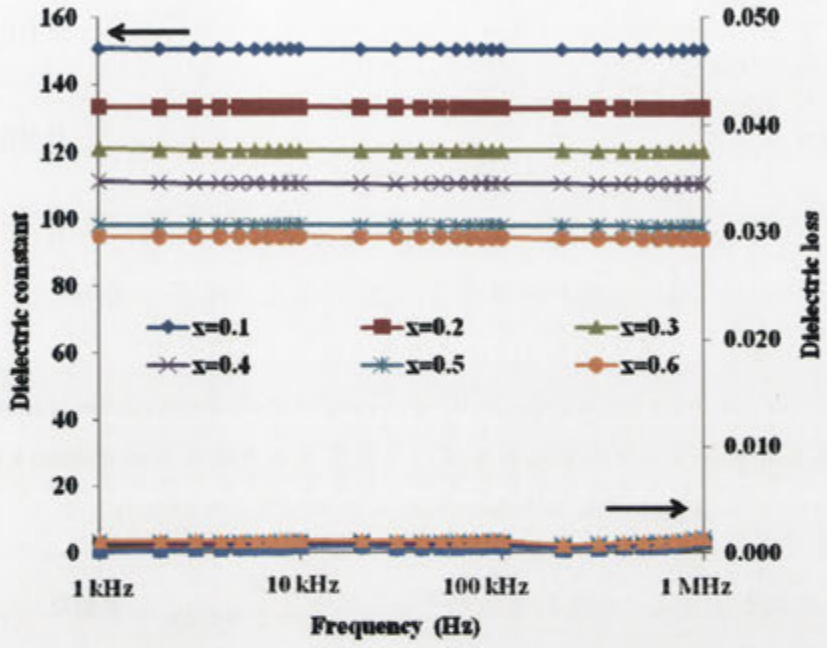

Figure 7-10 Frequency dependence of the room temperature dielectric properties of the $Ca_{1-x}Sm_{2x/3}TiO_3$ (x = 0.1 - 0.6) samples (sintered at 1450 °C for 3 hours).

Figure 7-12 shows the temperature dependence of the dielectric constant and dielectric loss of the x = 0.3, $Ca_{0.7}Sm_{0.2}TiO_3$, sample sintered at 1450 °C for 3 hours. CST samples of different compositions behaved similarly to this sample. Note that the dielectric constant decreases significantly, systematically and essentially linearly with increasing temperature. The temperature coefficient of the dielectric constant (τ_ε) is thus pretty similar over the entire measured temperature range.

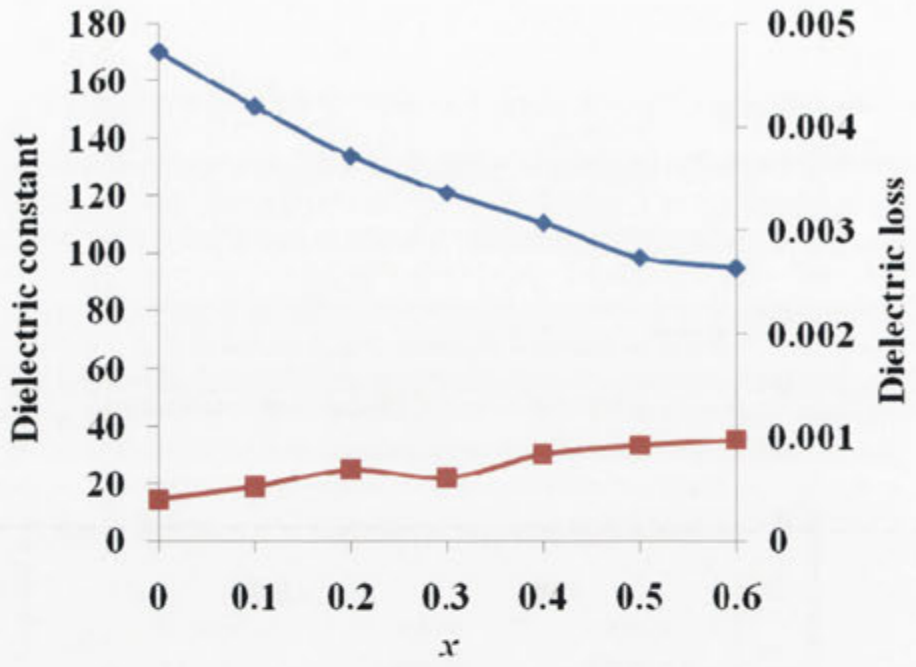

Figure 7-11 Variation in the measured room temperature dielectric constant and dielectric loss at an applied frequency of 1 MHz as a function of composition *x* in the $Ca_{1-x}Sm_{2x/3}TiO_3$ samples sintered at 1450 °C for 3 hours.

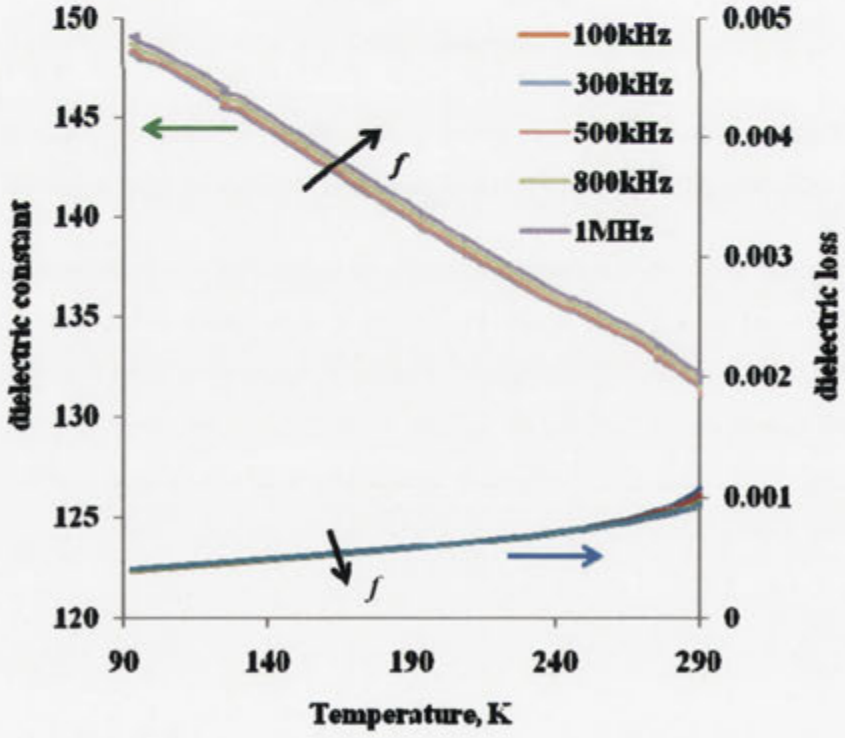

Figure 7-12 Temperature dependence of the dielectric constant and dielectric loss of the $Ca_{0.7}Sm_{0.2}TiO_3$ sample sintered at 1450°C for 3 hours.

Figure 7-13 below shows a plot of τ_ε extracted from plots such as that shown in Figure 7-12 as a function of composition x in the $Ca_{1-x}Sm_{2x/3}TiO_3$ samples sintered at 1450 °C for 3 hours. Note that the initially unacceptably high magnitude of magnitude for τ_ε (of 1850 ppm/K) reduces very significantly and systematically with increasing Sm^{3+} content. The initial increase of Sm^{3+} composition to $x = 0.1$ lead to a reduction in magnitude of τ_ε from 1850 ppm/K to 1010 ppm/K and it decreased further down to 234 ppm/K with the additional increase in x from 0.1 to 0.6. The initial substitution of Sm^{3+} into $CaTiO_3$ thus has a very strong initial effect on τ_ε which reduces as more Sm^{3+} is added. Similar behaviour manner has also been reported for other solid-solution systems involving *e.g.* $CaTiO_3$, $SrTiO_3$, $LaAlO_3$, $NdAlO_3$ [106,183,184,185].

Reaney et al [175] have reported a close empirical relationship between the measured τ_ε of complex ABO_3 perovskite structures and the so-called Goldschmidt tolerance factor (t) [194]:

$$t = \frac{R_A + R_B}{\sqrt{2}(R_B + R_O)} \qquad (7\text{-}1)$$

where R_A, R_B, and R_O are the respective ionic radii of the A-site ions, the B-site ions and the oxygen ions. In order to test this relationship in the case of the CST system, the composition dependent R_A was estimated by taking the average ionic radii to be given by $(1\text{-}x)R_{Ca} + {}^{2x}/_{3}\, R_{Sm}$. Using the ionic radii listed in Shannon [122], Figure 7-14 shows a plot of the measured τ_ε versus the calculated tolerance factor. Clearly the lower the tolerance factor the smaller the magnitude of τ_ε, in agreement with Reaney *et al.* [175]. As the tolerance factor is usually directly related to the magnitude of octahedral tilting, the magnitude of τ_ε also reduces with an increasing degree of oxygen octahedral tilting.

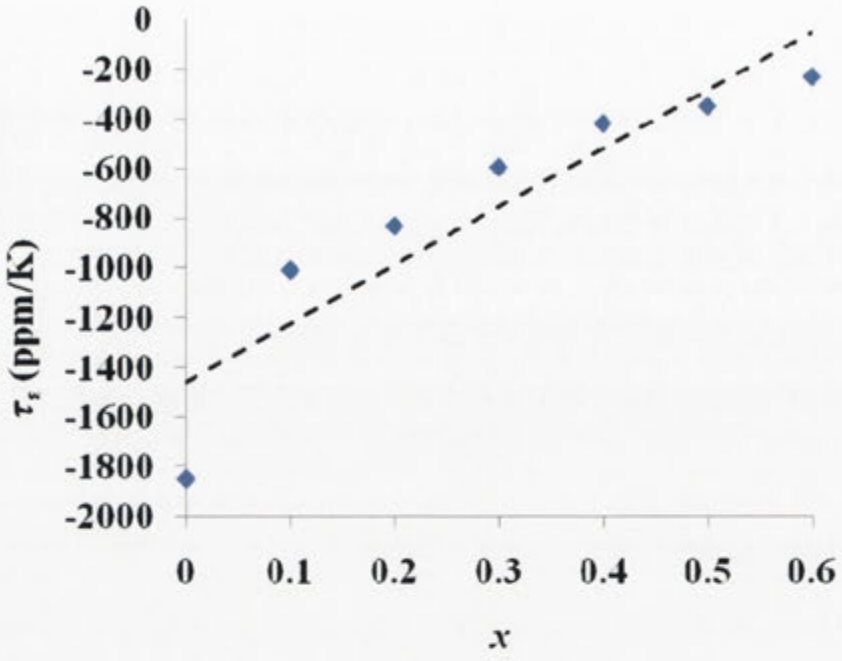

Figure 7-13 Shows the variation of the measured τ_ε as function of composition, *x*, for $Ca_{1-x}Sm_{2x/3}TiO_3$ samples sintered at 1450°C for 3 hours (the dashed line shows a linear fit to the data).

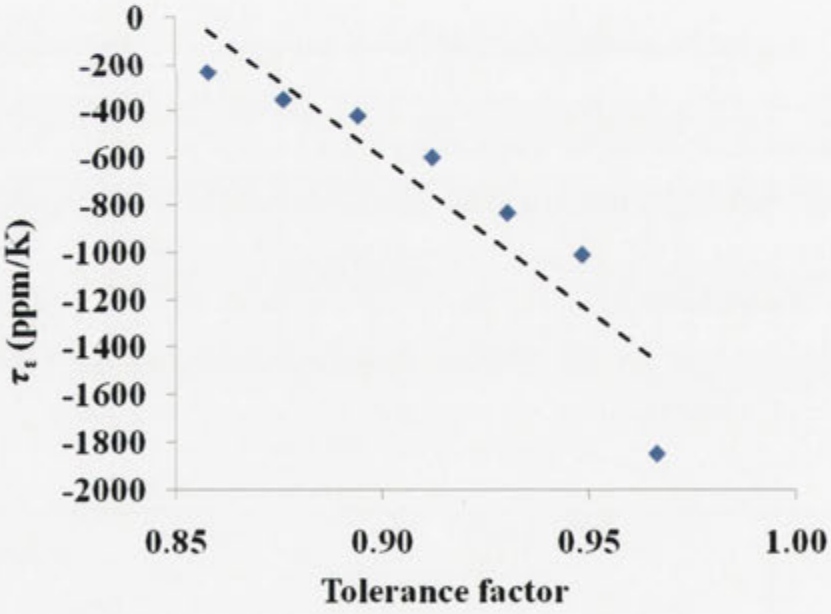

Figure 7-14 Variation of τ_ε as function of tolerance factor of $Ca_{1-x}Sm_{2x/3}TiO_3$ samples sintered at 1450°C for 3 hours (dashed line denotes a linear fit).

7.3.6.2 Effect of Final Sintering Temperature on Dielectric Properties

This final section briefly discusses the effect of the final sintering temperature on the relative densities and measured dielectric properties of the CST ceramics. Table 7-7, for example, lists the relative densities and dielectric properties of the $x = 0.3$, $Ca_{0.7}Sm_{0.2}TiO_3$, ceramics sintered for 3 hours as a function of the final resultant sintering temperature. Similar behaviour occurred for all compositions. The dielectric constant increased slightly from 110 to 121 while the dielectric loss dropped slightly as the final resultant sintering temperature rose from 1350 to 1450 °C, presumably a result of the increase in relative density from 92 to 95 %. It is important therefore to sinter at as high a temperature as possible in order to obtain as dense a resultant ceramic pellet as possible. On further increase in sintering temperature above 1450°C, however, the dielectric constant decreased while the dielectric loss increased. This worsening of the dielectric properties is most likely due to the onset of the partial reduction of Ti^{4+} to Ti^{3+} and associated oxygen vacancy formation. Such behaviour during high temperature sintering is known to lead to increased dielectric loss and reduced dielectric constants [187-189]. Similar behaviour was also caused by sintering in a reducing atmosphere and also leads to worse dielectric behaviour. In the case of the CST system, it seems that a final sintering temperature of 1450 °C is as high a final sintering temperature as is realistically possible.

Table 7-7 Dielectric properties and densities of $Ca_{0.7}Sm_{0.2}TiO_3$ ceramics sintered at different final sintering temperatures for 3 hours.

Sintering temperature (°C)	Relative density (%)	Dielectric properties (1 MHz)		
		ε	D	τ_ε
1350	92	110	0.00087	-557
1400	94	116	0.00083	-572
1450	95	121	0.00068	-598
1500	95	108	0.001	-555

Chapter 8: Summary and Conclusions

Conclusions

In this thesis, the synthesis, structural characterisation and dielectric properties of several 'misplaced displacive', Bi-based pyrochlore systems, one analogous, non-Bi-based pyrochlore system and one perovskite related electroceramic system have been carefully investigated along with the relationship between chemical bonding, local crystal structure, and dielectric properties (permittivity, dielectric loss, temperature coefficient of resonant frequency, electric field tunability *etc.*).

Two 'misplaced displacive', Bi-based cubic pyrochlore phases found in the Bi_2O_3-$M^{II}O$-Nb_2O_5 (M = Mg^{2+} and Ni^{2+}) systems, namely $(Bi_{1.667}Mg_{0.22}\square_{0.11})(Mg_{0.48}Nb_{1.52})O_7$ (BMN) and $(Bi_{1.667}Ni_{0.25}\square_{0.08})(Ni_{0.50}Nb_{1.5})O_7$ (BNN), were successfully synthesised and their average and local crystal structures as well as their dielectric properties carefully investigated. Rietveld average structure analyses of both samples show that the B_2O_6 octahedral sub-structure is fully occupied and essentially well-ordered. The $O'A_2$ tetrahedral sub-structure, on the other hand, was shown to be heavily displacively disordered with the A 'site' only partially occupied. Electron diffraction evidence in the form of transverse polarised, $\mathbf{G} \pm \{110\}^*$ 'sheets' of structured diffuse intensity suggests that the displacive disorder arises from essentially independent β-cristobalite like tetrahedral edge rotation and associated (inherently polar) rigid body translation of the $O'A_2$ sub-structure relative to the essentially rigid B_2O_6 octahedral sub-structure. Displacive disorder of this type provides a mechanism for understanding the structural origin of dipoles in such materials. Bond valence sum calculations provide a crystal chemical justification for the observed behaviour although the presence of vacancies on the A site considerably complicates such considerations. The measured room temperature dielectric constants of both samples were quite high while the associated dielectric losses were low. Anomalous low temperature dielectric relaxation behaviour was observed in both cases.

In the case of the Bi_2O_3-$M^{III}{}_2O_3$-Nb_2O_5 (M = In and Sc) systems (see Chapter 5), stoichiometric Bi-based cubic pyrochlores Bi_2InNbO_7 (BIN) and Bi_2ScNbO_7 (BSN) were successfully synthesised and their ideal composition confirmed.

Electron diffraction again provided clear evidence for β-cristobalite like tetrahedral edge rotation and associated (inherently polar) rigid body translation of the O'A_2 sub-structure. Essentially identical structured diffuse scattering has also been reported in the close to A site stoichiometric $Bi_2Ru_2O_{7-\delta}$ [74] and $(Bi_{1.89}Fe_{0.11})(Fe_{1.05}Nb_{0.95})O_{6.95}$ (BFN) [25] pyrochlores. The measured room temperature dielectric constants of both samples were again quite high (~ 120 for BIN and > 200 for BSN). The room temperature dielectric losses (or imaginary permittivities), however, were not as low as for BNN and BMN at the same frequency as a result of the higher temperature of the low temperature dielectric relaxation again observed in the BIN and BSN samples. This shows that compositional disorder on the pyrochlore A site is not essential for the low temperature dielectric relaxation characteristic of most Bi-based pyrochlores. Low temperature electron diffraction well below the peak in the imaginary permittivities showed the same structured diffuse scattering as at room temperature suggesting that the "diffuse phase transition" is not a paraelectric to ferroelectric transition but rather some sort of dynamic to static glass-like transition.

In Chapter 6, an analogous non-Bi-based, cubic pyrochlore of composition $(Ca_{1.5}Nb_{0.50})(Nb_{0.52}Ti_{1.48})O_7$ (CNT) was synthesised and its dielectric properties and crystal chemistry investigated. The same low temperature dielectric relaxation behaviour was again observed showing that the presence of presence of Bi^{3+} with its lone electron pair on the pyrochlore A site is not necessary for such behaviour to be observed. Bond valence sum calculations show that Ca on the pyrochlore A site is significantly over-bonded and thus would not be expected to move off-centre by contrast with Bi-based pyrochlore phases. The minority Ti ion on the pyrochlore A site, however, is massively under-bonded. This suggests that the O' ions in the local O'Ca_3Ti tetrahedra would want to move away from the Ca ions and towards the Ti ions. No evidence for this, however, could be found in the form of structured diffuse scattering.

In Chapter 7, as an extension of this study and in partnership with an industry collaborator, the synthesis as well as the relationship between local crystal structure, microstructure and dielectric properties of a promising dielectric ceramic system, namely $Ca_{1-x}Sm_{2x/3}TiO_3$ (CST, $0 \leq x \leq \sim 0.6$) was investigated. CST samples sintered

at 1450 °C for 3 hours in air and oxygen were all found to be single phase for compositions from $x = 0.1$ to $x = 0.6$ and quite similar to those reported for the end-member compound, $CaTiO_3$. Powder XRD as well as electron diffraction patterns (EDPs) of CST samples were entirely consistent with a *Pnma*, $\sqrt{2}a_p$ x $2a_p$ x $\sqrt{2}a_p$ (subscript p for parent perovskite sub-structure) average crystal structure. The refined *b* and *c* axis dimensions increased systematically with composition *x* while the *a* axis dimension systematically decreased until the *a* and *c* axis dimensions crossed over close to $x = 0.6$. EDPs and HRTEM image analyses suggest short range Ca and Sm ordering in the CST samples which became more and more obvious on increasing Sm content. The dielectric properties of the CST samples varied significantly with Sm content, in particular the temperature coefficient of the dielectric constant, τ_ε, is tuneable by Sm-doping.

In conclusion, local structural 'disorder', of both compositional and/or coupled displacive origin, plays a significant role in tuning or modifying the dielectric properties of the dielectric materials investigated in this thesis.

REFERENCES

1. W. Wersing, High frequency ceramic dielectrics and their application for microwave components, in: *Electronic Ceramics*, B.C.H. Steele (Ed.), Elsevier Applied Science, London, p. 67–119 (1991).

2. W. Wersing, *Curr. Opin. Solid State Mater. Sci.* **1**, p. 715-731 (1996).

3. R.J. Cava, *J. Mat. Chem.* **11**, p. 54-62 (2001).

4. T.A. Vanderah, *Science* **298**, p. 1182-1183 (2002).

5. D.M. Zogbi, *2008 Global Market Presentation Series: Capacitors, Resistors & Inductors*, Paumanok Publications Inc. Morrisville, NC 27560 USA (2008).

6. Global Industry Analysts, *Ceramic Capacitors - A Global Strategic Business Report*, Global Industry Analysts Inc. (2009).

7. R.J. Cava, J.J. Krajewski and R.S. Roth, *Mat. Res. Bull.* **34**, p. 355-362 (1999).

8. W. Lan, M. Liang, C. Hu, K. Liu and I. Lin, *Mater. Chem. Phys.* **79**, p. 266-270 (2003).

9. H. Hughes, D.M. Iddles, I.M. Reaney, *Appl. Phys. Letts.* **79**, p. 2952-2954 (2001).

10. I. Molodetsky and P.K. Davies, *J. Eur. Ceram. Soc.* **21,** p. 2587-2591 (2001).

11. C. Huang, R. Lin and J. Wang, *Jpn. J. Appl. Phys.* **41**, p. 758-762 (2002).

12. H. Kim, S. Kim, S. Nahm, J. Byun and Y. Kim, *J. Am. Ceram. Soc.* **82**, p. 3043-3048 (1999).

13. H. Kagata, T. Inoue, J. Kato, I. Kameyama, *Jpn. J. Appl. Phys.* **31**, p. 3152-55 (1992).

14. N. Wang, M. Zhao, Z. Yin and W. Li, *Mat. Res. Bull.* **39**, p. 439-448 (2004).

15. W. Ren, S. Trolier-McKinstry, C.A. Randall and T.R. Shrout, *J. Appl. Phys.* **89**, p. 767-774 (2001).

16. J. Lu and S. Stemmer, *Appl. Phys. Lett.* **83**, p. 2411-2413 (2003).

17. I. Levin, T.G. Amos, J.C. Nino, T.A. Vanderah, C.A. Randall and M.T. Lanagan, *J. Solid. State Chem.* **168**, p. 69–75 (2002).

18. R.L. Withers, T.R. Welberry, A.K. Larsson, Y. Liu, L. Norén, H. Rundlöf and F.J. Brink, *J. Solid State Chem.* **177**, p. 231–244 (2004).

19. B. Melot, E. Rodriguez, Th. Proffen, M.A. Hayward and R. Seshadri, *Mat. Res. Bull.* **41**, p. 961-966 (2006).

20. T.A. Vanderah, I. Levin and M.W. Lufaso, *Eur. J. Inorg. Chem.* **14**, p. 2895–2901 (2005).

21. D.P. Cann, C.A. Randall and T.R. Shrout, *Solid State Commun.* **100**, p. 9529–9534 (1996).

22. G.I. Golovshchikova, V.A. Isupov, A.G. Tutov, I.E. Mylnikova, P.A. Nikitina and O.I. Tulinova, *Sov. Phys. Solid State* **14**, p. 2539-2542 (1973).

23. M. A. Subramanian et al., Oxide pyrochlores-A review, *Prog. Solid. State. Chem.* **15**, p. 55-143 (1983).

24. M.A. Subramanian, A.W. Sleight, Rare earth pyrochlores. In: *Handbook on the Physics and Chemistry of the Rare Earths*. (Ed. Gschneidner, K.A. Jr. and Eyring, L.) **16,** Chapter 107, 225-248 (1993).

25. International Union of Crystallography, *International Tables for Crystallography. Vol. A. Space-group symmetry*, edited by Th. Hahn, 5th ed., corrected reprint. Heidelberg: Springer (2005).

26. B.B. Hinojosa, J.C. Nino and A. Asthgari, *Phys. Rev. B* **77**, p. 104123 (2008).

27. B. Kennedy, *Mater. Res. Bull.* **32**, p. 479-483 (1997).

28. T.A. Vanderah, T. Siegrist, M.W. Lufaso, M.C. Yeager, R.S. Roth, J.C. Nino and S. Yates, *Eur. J. Inorg. Chem.* **23**, p. 4908–4914 (2006).

29. I.R. Evans, J.A.K. Howard, J.S.O. Evans, *J. Mater. Chem.* **13**, p. 2098-2103 (2003).

30. W.S. Kim, E.S. Kim, and K.H. Yoon., *J. Am. Ceram. Soc.* **82**, p. 2111–2115 (1999).

31. T. Birchal, A.W. Sleight, *J. Solid State Chem.* **13**, p. 118-130 (1975).

32. R.H. Jones and K.S. Knight, *J. Chem. Soc., Dalton Trans.*, p. 2551-2555 (1997).

33. I. Radosavljevic, J.S. O. Evans, and A.W. Sleight, *J. Solid State Chem.* **136**, p. 63-66 (1998).

34. Sietronics Pty Ltd., P.O. Box 3066, Belconnen, ACT 2617, Australia.

35. B. Noläng, *Inst. Materialkemi, Ångströmlaboratoriet*, Box 538, S-751 21, Uppsala, Sweden (1996).

36. R. Wuhrer, K. Moran and L. Moran, *Mater. Forum* **30**, p. 63-70 (2006).

37. D. Newbury, R. Marinenko, Microscopy and Microanalysis 9 (Suppl.2), *J.Armstrong, J.Small and E.Steel* **528** (2003).

38. Y. Liu, R.L. Withers, T.R. Welberry, Hong Wang and Huiling Du, *J. Solid State Chem.* **179**, p. 2141–2149 (2006).

39. Y. Liu, R.L. Withers, T.R. Welberry, H. Wang, H.L. Du and X. Yao, *J. Electroceram.* **21**, p. 401-404 (2007).

40. C. Giacovazzo , H.L. Monaco , G. Artioli, D. Viterbo , G. Ferraris, G. Gilli, G. Zanotti , M. Catti, *Fundamentals of Crystallography* **2nd ed.**, Oxford University Press, USA (2002).

41. C.J. Howard, S.J. Kennedy, *Mater. Forum.* **18**, p. 155-176 (1994).

42. A.J. Dianoux, G. Lander, *Neutron Data Booklet*, 2nd edition, OCP Science (2003).

43. B.A. Hunter, Rietica - A Visual Rietveld Program, *Commission on Powder Diffraction Newsletter* **20**, p. 21 (1998).

44. Archimedes of Syracuse, *On Floating Bodies Vol. I, Proposition 7* (ca 265 BC).

45. M. Takata, and K. Kageyama. *J. Am. Ceram. Soc.* **72**, p. 1955-1959 (1989).

46. G.M. Sessler, *Electrets.*, Springer, Berlin (1980).

47. A.J. Moulson and J.M. Herbert, *Electroceramics: materials, properties, applications,* **2 ed.**, John Wiley and Sons (2003).

48. M. Faraday, *Phil. Trans.*, **128**(1) (1837).

49. I.M. Reaney and R. Ubic. *Int. Ceram.* **1**, p. 48-52 (2000).

50. S. Nomura. *Ferroelectrics* **49**,p. 61-70 (1983).

51. S.J. Penn, NM. Alford, A. Templeton, X. Wang, M. Xu, M. Reece and K. Scrapel, *J. Am. Ceram. Soc.* **80**, p. 1885-1888 (1997).

52. H.S. Park, K.Y.H. Yoon and E.S. Kim, *J. Am. Ceram. Soc.* **84**, p. 99-103 (2001).

53. T. Nagai, T. Inuzuka, and M. Sugiyama, *Jpn J. Appl. Phys.* **31**, p. 3132-3135 (1992).

54. G. Huang, D. Zhou, J. Xu, Z. Zheng, S. Gong, *Mater. Res. Bull.* **40**, p. 13-19 (2005).

55. D.L. Cairnsa, I.M. Reaneya, N. Ottena, D. Iddlesb and T. Priceb, *J. Eur. Ceram. Soc.* **26** (6), p. 875-882 (2006).

56. J.C. Nino, H.J. Youn, M.T. Lanagan, C.A. Randall, *J. Mater. Res.* **17** (5), p. 1178-1182 (2002).

57. BSRIA Instrument Solutions Ltd (2005).

58. V.P. Sirotinkin and A.A. Bush, *Inorg. Mater.* **39**, p. 974–977 (2003).

59. X. Wang, H. Wang and X. Yao, *J. Am. Ceram. Soc.* **80**, p. 2745–2748 (1997).

60. W. Ren, S. Trolier-McKinstry, C.A. Randall and T.R. Shrout, *J. Appl. Phys.* **89**, p. 767–774 (2001).

61. D. Liu, Y. Liu, S.Q. Huang and X. Yao, *J. Am. Ceram. Soc.* **76**, p. 2129-2132 (1993).

62. M. Valant and P.K. Davies, *J. Am. Ceram. Soc.* **83**, p. 147-153 (2000).

63. K.B. Tan, C.K.Lee, Z. Zainal, G.C. Miles and A.R. West, *J. of Materials Chem.* **15**, p. 3501–3506 (2005).

64. V. Krayzman, I. Levin, and J. C. Woicik, *Chem. Mater.* **19**, p. 932 (2007).

65. S. Kamba, V. Porokhonskyy, A. Pashkin, V. Bovtun, J. Petzelt, J.C. Nino, S. Trolier-McKinstry, M.T. Lanagan and C.A. Randall, *Phys. Rev. B* **66**, p. 054106 (2002).

66. J.C. Nino, M.T. Lanagan, and C.A. Randall, *J. Appl. Phys.* **89,** p. 4512-4516 (2001).

67. M. Valant and D. Suvorov, *J. Am. Ceram. Soc.* **88**, p. 2540–2543 (2005).

68. M.W. Lufaso, T.A. Vanderah, I.M. Pazos, I. Levin, R.S. Roth, J.C. Nino, V. Provenzano and P.K. Schenk, *J. Solid State Chem.*, **179,** p. 3900-3910 (2006).

69. W. Somphon, V. Ting, Y. Liu, R.L. Withers, Q. Zhou and B.J. Kennedy, *J. Solid State Chem.* **179**, p. 2495–2505 (2006).

70. N.E. Brese and M. O'Keeffe, *Acta Crystallogr. B* **47**, p. 192–197 (1991).

71. J.C. Nino, M.T. Lanagan, C.A. Randall and S.Kamba, *Appl. Phys. Letts.* **81**, p. 4404 (2002).

72. C. Ahn, Z. Yu, H.J. Youn, C.A. Randall, A.S. Bhalla, L.E. Cross, J. Nino and M. Lanagan, *Appl. Phys. Letts.* **80**, p. 4807 (2002).

73. J.A. Mydosh, *Spin Glasses: An experimental Introduction*, Taylor & Francis, London (1993).

74. R.S. Roth, T.A. Vanderah, P. Bordet et al., *J. Solid State Chem.* **181**, p. 406 (2008).

75. A.L. Hector and S.B. Wiggin, *J. Solid State Chem.* **179**, p. 2495 (2006).

76. F. Jona, G. Shirane, and R. Pepinsky, *Phys. Rev.* **98**, p. 903 (1955).

77. Q. Zhou, B.J. Kennedy, V. Ting et al., *J. Solid State Chem.* **178**, p. 1575 (2005).

78. A.L. Goodwin, R.L. Withers and B.H. Nguyen, *J. Phys. :Condens. Matter.* **19**, p. 335216 (2007).

79. R. Seshadri, *Solid State Sci.* **8**, p. 259 (2006).

80. T.A. Vanderah, M.W. Lufaso, A.U. Adler, I. Levin, J.C. Nino, V. Provenzano and P.K. Schenk, *J. Solid State Chem.* **179**, p. 3467-3477 (2006).

81. M. Avdeev, M.K. Haas, J.D. Jorgensen and R.J. Cava, *J. Solid State Chem.* **169**, p. 24 (2002).

82. Y. Liu, R.L. Withers, X. Wei and J.D. Fitz Gerald, *J. Solid State Chem.* **180**, p. 858 (2007).

83. R.L. Withers, Y. Liu and T.R. Welberry, *J. Solid State Chem.* **182**, p. 348 (2009).

84. V. Bovtun, J. Petzelt, V. Porokhonsky et al, *J. Eur. Ceram. Soc.* **21**, p. 1307 (2001).

85. I.P. Swainson and M.T. Dove, *Phys. Rev. Lett.* **71**, p. 193 (1993).

86. S.A. Wells, M.T. Dove, M.G. Tucker, and K. Trachenko, *J. Phys.:Condens. Matter.* **14**, p. 4645 (2002).

87. I.P. Swainson and M.T. Dove, *J. Phys.: Condens. Matter* **7**, p. 1771 (1995).

88. R.A. McCauley, *J. Opt. Soc. Am.* **63**, p. 721 (1973).

89. A. Jongejan and A.L. Wilkins, *J. less-common Metals* **19** (1970).

90. M. Valant and P.K. Davies, *J. Mat. Sci.* **34,** p. 5437-5442 (1999).

91. C.A. Randall, J. C. Nino, A. Baker, et al., *Am. Ceram. Soc. Bull.* **82**, p. 9101 (2003).

92. I.D. Brown and D. Altermatt, *Acta. Cryst. B* **41**, p. 244-247 (1985).

93. Y. Pyo Hong, S. Ha, H. Yong Lee et al., *Thin Solid Films* **419**, p. 183 (2002).

94. M.T. Sebastian, *Dielectric materials for wireless communication*, Elsevier, Oxford, UK (2008).

95. A.K. Tagantsev, V.O. Sherman, K.F. Astafiev, J. Venkatesh and N. Setter, *J. Electroceram.* **11**(1), p. 5 (2003).

96. X.M. Chen, T. Wang and J. Li, *Mater. Sci. Eng. B* **113**, p. 117 (2004).

97. X. Chou, J. Zhai and X. Yao, *Mater. Chem. Phys.* **109**, p. 125 (2008).

98. J.H. Jeon, *J. Eur. Ceram. Soc.* **24** (6), p. 1045. (2004).

99. R.K. Zheng, J. Wang, X.G. Tang, Y. Wang, H.L.W. Chan, C.L. Choy and X.G. Li, *J. Appl. Phys.* **98** (8), p. 084108 (2005).

100. X. Wang, H. Yamada and C.N. Xu, *Appl. Phys. Lett.* **86** (2), p. 022905 (2005).

101. X. Wang, L. Zhang, H. Liu, J. Zhai, X. Yao, *Mater. Chem. Phys.* **112**(2), p. 675-678 (2008) .

102. R.C. Kell, A.C. Greenham, and G.C. Olds, *J. Am. Ceram. Soc.* **56**(7), 352–354 (1973).

103. H. Zheng, G.D.C. de Gyorgyfalva, and I.M. Reaney., *J. Mater. Sci.* **40**, p. 5207–5214. (2005).

104. P.L. Wise, I.M. Reaney, W.E. Lee, T.J. Price, D.M. Iddles, and D.S. Cannell, *J. Eur. Ceram. Soc.* **21**, p. 1723–1726. (2001).

105. Y. Konishi, *Proc. IEEE* **79**, p. 726–740. (1991).

106. B. Jancar, D. Suvorov, M. Valant, G. Drazic, *J. Eur. Ceram. Soc.* **23**(9), p. 1391-1400 (2003).

107. J. Zheng, C. Zhang, Z. Xiong, F. Xiao, G. Yang, H. Xue, *J. Phys. Conf. Ser.* **152**, p. 012062 (2009).

108. G. Huang, J. Xu, Y. Tang, J. Huang, P. Tang, D. Zhou, *Key Eng. Mater.* **368-372**(1), p. 147-149 (2008).

109. G.A. Ravi, F. Azough, R. Freer, *J. Eur. Ceram. Soc.* **27**(8-9), p. 2855-2859 (2007).

110. D.D. Khalyavin, A.N. Salak, A.M.R. Senos, P.Q. Mantas, V.M. Ferreira, *J. Am. Ceram. Soc.* **89**(5), p. 1721-1723 (2006).

111. B. Jancar, D. Suvorov, M. Valant, *Ceram. Trans.* **150**, pp. 171-183 (2004).

112. E.S. Kim and K.H. Yoon., *J. Eur. Ceram. Soc.* **23**, p. 2397–2401 (2003).

113. H.L. Chen and C.L. Huang., *Jpn. J. Appl. Phys.* **41**, p. 5650–5653 (2002).

114. N. Ichinose and N. Chida., *Proc. IEEE Int. Symp.*, p. 513–514 (1998).

115. N. Ichinose and K. Mutoh., *J. Eur. Ceram. Soc.* **23**, p. 2455–2459(2003)

116. D. Suvorov, M. Valant, B. Jancar, and S.D. Skapin, *Acta Chimi. Slov.* **48**, p. 87–99 (2001).

117. C.H. Wei and J.H. Jean., *J. Am. Ceram. Soc.* **86**(1), p. 93–98 (2003).

118. K.H. Yoon, W.S. Kim, E.S. Kim, *Mater. Sci. Eng., B* **99**(1-3), p. 112-115 (2003).

119. C.H. Shen, C.L. Huang, C.F. Shih, C.M. Huang, *J. Alloys Compd.* **475**(1-2), p. 391-395 (2009).

120. M.S. Fu, X.Q. Liu, X.M. Chen, *J. Eur. Ceram. Soc.* **28**, p. 585–590 (2008).

121. *ICDD PDF-2 Release 2004*, International Centre for Diffraction Data, 12 Campus Boulevard Newtown Square, PA 19073-3273 U.S.A (2004).

122. R.D. Shannon, *Acta Crystallogr., Sect. A: Cryst. Phys. Diffr., Theor. Gen. Crystallogr.* **A32**, p. 751–67 (1976).

123. W. Zhou, R. Ran, Z. Shao, W. Jin and N. Xu, Journal of Power Sources 182(1), p. 24-31 (2008).

124. M.W. Lufaso and P.M. Woodward, *Acta Cryst.* **B57**, p. 725-738 (2001).

125. M.W. Lufaso and P.M. Woodward, *SPuDS Users Guide,* (http://www.unf.edu/~michael.lufaso/spuds/manual.pdf) (2009).

126. Y. Lee, C.S. Park, *IEEE Microwave Wireless Compon. Lett.* **13** (12), p. 499-501 (2003).

127. H.P. Klug, L. E. Alexander. *X-ray Diffraction Procedures for Polycrystalline and Amorphous Materials*. New York: Wiley-Interscience (1974).

128. H.P. Rooksby, *Rep. Prog. Phys.* **10**, p. 83-119 (1944).

129. W. Paszkowicz, *Synchrotron Radiation in Natural Science* **5**(1-2), p. 115-126 (2006).

130. B.D. Cullity, *Elements of X-Ray Diffraction*, Addison-Wesley Publishing Company, Inc. (1996).

131. R.A. Young, *The Rietveld Method,* (International Union Of Crystallography Monographs On Crystallography **5**), Oxford University Press (1995).

132. E. Aleshin and R. Roy, *J. Am. Ceram. Soc.* **45(1),** p. 18-25 (1962)

133. H. Du, X. Yao and L. Zhang, *Ceram. Int.* **28**, p. 231–234 (2002).

134. J.Y. Kim, D.W. Kim, H.S. Jung and K.S. Jung, *Jpn. J. of Appl. Phys.* **44A** p. 6648-6653 (2005).

135. H. Du and X. Yao, *J. Mat. Sci: Mat. Elec.* **15,** p. 613-616 (2004).

136. E. Jansen, W. Schäfer and G. Will, *J. Appl. Cryst.* **27,** p. 492-496 (1994).

137. Paumanok Publications, *Ceramic Dielectric Materials: World Markets, Technologies & Opportunities: 2008-2013*, Paumanok Publications, Inc (2008).

138. USGS, a Laboratory Manual for X-Ray Powder Diffraction, *U.S. Geological Survey*, U.S. Department of the Interior (2001).

139. A. Rack, *Electron Microscopy*, University of Tennessee, Dept. of Materials Science and Engineering (2004).

140. K.C.A. Smitha et al, The fiftieth anniversary of the first applications of the scanning electron microscope in materials research, *Physics Procedia* **1,** p. 3-12 (2008).

141. I. Levin, T.G. Amos, J.C. Nino, T.A. Vanderah, I.M. Reaney, C.A. Randall ad M.T. Lanagan, *J. Mater. Res.* **17**, p. 1406 (2002).

142. E. Courtens, *Phys. Rev. Lett.* **52**, p. 69 (1984) .

143. K. Binder and A.P. Young, *Rev. Mod. Phys.* **58**, p. 801 (1986).

144. P.J.W. Debye, *Polar Molecules*, The Chemical Catalog Co., New York, NY (1929).

145. B.K.P. Scaife, Monographs on the physics and chemistry of materials: *Principles of Dielectrics*, Oxford Science Publications, Oxford, England (1998).

146. Hewlett Packard, *Basics of measuring the dielectric properties of materials*, Hewlett Packard literature number 5091-3300E, (1992).

147. R.D. Richtmyer, *J. Appllied. Physics.* **10**, 391 (1939).

148. R. Nawrodt, A. Zimmer, T. Koettig, S. Nietzsche, M. Thürk, W. Vodel and P. Seidel , *Eur. Phys. J. Appl. Phys.* **38**, p. 53-59 (2007).

149. I.M. Reaney, P. Wise, R. Ubic, J. Breeze, MCN. Alford, D. Iddles, D. Cannell and T. Price. *Philos. Mag.* **A81**(2), p. 501-510 (2001).

150. L.F. Chen, C.K. Ong, C.P. Neo, V.V. Varadan, V.K. Varadan, *Microwave Electronics: Measurement and Materials Characterization*, Wiley (2004).

151. D. Kajfez, *Q factor measurements, analog and digital*, University of Mississippi (1999).

152. D. Kajfez and E. J. Hwan, *IEEE Trans. Microwave Theory Tech.* **32**, p. 666-670 (1984).

153. A. Asija and A. Gundavajhala, *RF Design* **10**, p. 48-52 (1994).

154. V. Kolmarov, S. Wang, J. Tang, *Permittivity and Measurement*, Washington State University (2004).

155. Agilent, *Basics of Measuring the Dielectric Properties of Materials*, Agilent Technologies, Inc. (2006).

156. L. Chen, C.K. Ong, and B.T. Tan, *IEEE Trans. Instrum. Meas.* **48**, p. 1031–1037 (1999).

157. K. Chang, *Encyclopedia of RF and Microwave Engineering*, John Wiley & Sons, Inc., Hoboken, New Jersey (2005).

158. V.V. Romanov and V.V. Yakovlev, *Microwave Opt. Technol. Lett.* **39N**(6), p. 443–446 (2003).

159. J. Krupka, D. Cros, M. Auburg, and P. Guillon, *IEEE Trans. Microwave Theory Tech.* **42**, p. 56–61 (1994).

160. X.C. Fan, X.M. Chen, *J. Am. Ceram. Soc.* **92**(2), p. 433-438 (2009).

161. I.N. Jawahar, I.S. Narayana, T.S. Mailadil, M. Pezholil. *J. Mater. Res.* **17** (12), p. 3084-3089 (2002).

162. Y.C. Chen, P.S. Cheng, C.F. Yang, W.C. Tzou. *J. Mater. Sci. Lett.* **20**(9), p. 863-865 (2001).

163. E.L. Ginzton, *Microwave Measurements*, McGraw-Hill, New York, Chap. 9 (1957).

164. I. Bahl and P. Bhartia, *Microwave Solid State Circuit Design*, Wiley, New York, Chap. 3 (1988).

165. J.S. Kim, C.I. Cheon, H.J.Kang, C.H. Lee, K. Y. Kim, S. Nahm, and J.D. Byun., *Jpn. J. Appl. Phys.* **38**, p. 5633–5637 (1999).

166. Y. Higuchi and H. Tamura, *J. Eur. Ceram. Soc.* **23**(14), p. 2683-2688 (2003).

167. C.L. Huang, Y.B. Chen and C.W. Lo, *Jpn. J. Appl. Phys.* **44**, p. 3147-3150 (2005).

168. N. Santha, I. N. Jawahar, P. Mohanan and M. T. Sebastian, *Mater. Lett.* **54**(4), p. 318-322 (2002).

169. Y.B. Chen, C.L. Huang and S.T. Tasi, *Mater. Lett.* **62**(16), p. 2454-2457 (2008).

170. C.L. Huang, J.T. 170 and Y.B. Chen, *Mater. Res. Bull.* **36**, p. 547-556 (2001).

171. P. Jha, A.K. Ganguli, *Solid State Sci.* **6**, p. 663–671 (2004).

172. F.S. Galasso, *Perovskites and High-Tc Superconductors*, Gordon and Breach, New York (1990).

173. M. Yoshida, N. Hara, T. Takada, and A. Seki, *Jpn. J. Appl. Phys.*, **36** (11) 6818–23 (1997).

174. K.H. Yoon, Y.H. Chang, W.S. Kim, J.B. Kim, and E.S. Kim, *Jpn. J. Appl. Phys.* **35, p.** 5145–5149 (1996).

175. I.M. Reaney, E.L. Colla and N. Setter. *Jpn. Appl. Phys.* **33**, p. 3984 (1994).

176. I.S. Kim, W.H. Jung, Y. Inaguma, T. Nakamura and M. Itoh, *Mater. Res. Bull.* **30**, p. 307 (1995).

177. J. Petzelt, S. Pacesova, J. Fousek, S. Kamba, V. Zelezny, V. Koukal, J. Schwarzbach, B.P. Gorshunov, G.V. Kozolov and A.A. Volkov, *Ferroelectric* **93**, p. 77 (1989).

178. D.M. Iddles, A.J. Bell and A.J. Moulson, *J. Mater. Sci.* **27**, p. 6303 (1992).

179. S. Hirano, T. Hayashi and A. Hattori, *J. Am. Ceram. Soc.* **74**, p. 1320 (1991).

180. E.S. Kim, B.S. Chun, D.H. Kang, *J. Eur. Ceram. Soc.* **27**, p. 3005–3010 (2007).

181. E.S. Kim, W. Choi, K.H. Yoon and Y.T. Kim, *Ferroelectrics* **257**, p. 169 (2001).

182. K. Sudheendran, K.C. RaJu, *Indian J. Eng. Mater. Sci.* **15**(2), p. 133-136 (2008).

183. S. Kucheiko, J.W. Choi, H.J. Kim and H.J. Jung, *J. Am. Ceram. Soc.* **79**(10), p. 2739–2743 (1996).

184. S.Y. Cho, H.J. Youn, H.J. Lee and K.S. Hong, *J. Am. Ceram. Soc.* **84**(4), p. 753–758 (2001).

185. P.H. Sun, T. Nakamura, Y.J. Shan, Y. Inaguma, M. Itoh and T. Kitamura, *Jpn. J. Appl. Phys.* **37**(10), p. 5625–5629 (1998).

186. V.V.A. Lemanov, V. Sotnikov, E.P. Smirnova, M. Weihnacht and R. Kunze,. *Solid State Commun.* **110**, p. 611–614 (1999).

187. T. Takada, S. F. Wang, S. Yoshikawa, S.J. Jang, and R.F. Newnham, *J. Am. Ceram. Soc.* **77**(7), p. 1909–1916 (1994).

188. D.W. Kim, K.H. Ko, D.K. Kwon, and K.S. Hong, *J. Am. Ceram. Soc.* **85**(5), p. 1169-1172 (2002).

189. A. Templeton, X. Wang, S.J. Penn, S.J. Webb, L.F. Cohen and N.M. Alford, *J. Am. Ceram. Soc.* **83**(1), p. 95–100 (2000).

190. Y. Gua, J. Huang, Q. Li, D. Sun and H. Xu, *J. Eur. Ceram. Soc.* **28**(16), p. 3149-3153 (2008).

191. K.H. Yoon, M.S. Park, J.Y. Cho, and E.S. Kim, *J. Eur. Ceram. Soc.* **23**, p. 2423-2427 (2003).

192. D.A. Sagala and S. Nambu, *J. Am. Ceram. Soc.* **75**, p. 2573 (1962).

193. R.D. Shannon, *J. Appl. Phys.* **73**(1), p. 348-366 (1993).

194. V.M. Goldschmidt, Skrifer Norske Videnskaps-Akad. Oslo, *I. Mat.-Nat. Kl.* **8** (1926).

195. M. Viviani, M. Bassoli, V. Buscaglia, M.T. Buscaglia and P. Nanni, *J. Phys. D: Appl. Phys.* **42**, p. 175407 (2009).

196. G.L. Fisher, *J. Phys. D: Appl. Phys.* **4**, p. 1439-1447 (1971).

Publications Related to this Thesis

B. Nguyen, Y. Liu and R.L. Withers, The local crystal chemistry and dielectric properties of the cubic pyrochlore phase in the Bi_2O_3-M^{2+}O-Nb_2O_5 (M^{2+} = Ni^{2+} and Mg^{2+}) systems., *J. Solid State Chem.* **180**(2), p. 549 (2007).

B.H. Nguyen, L. Norén, Y. Liu, R.L. Withers, X. Wei and M.M. Elcombe, The disordered structures and low temperature dielectric relaxation properties of two misplaced-displacive cubic pyrochlores found in the Bi_2O_3-M^{II}O-Nb_2O_5 (M = Mg, Ni) systems, *J. Solid State Chem.* **180**(8), p. 2558 (2007).

Y. Liu, R.L. Withers, B. Nguyen and K. Elliott, Structurally frustrated polar nanoregions in $BaTiO_3$-based relaxor ferroelectric systems, *Appl. Phys. Lett.* **91**(15), p. 152907/1-3 (2007).

A.L. Goodwin, R.L. Withers and B.H. Nguyen, Real-space refinement of single-crystal electron diffuse scattering and its application to $Bi_2Ru_2O_{7-\delta}$, *J. Phys.: Condens. Matter* **19**(33), p. 335216/1-15 (2007).

Y. Liu, R.L. Withers, B. Nguyen and X.Y. Wei, Towards the development of high performance, frequency agile, RF/microwave ceramics based on nanoscale structural analysis, *J. Aust. Ceram. Soc.* **43**(2), p. 75-78(2007).

B. Nguyen, Y. Liu and R.L. Withers, Relaxor dielectric properties of a $(Ca_{1.5}Ti_{0.5})(NbTi)O_7$ 'misplaced-displacive' cubic pyrochlore synthesised via metallorganic decomposition, *Solid State Communications* **145**(1-2), p. 72-76 (2008).

Y. Liu, R.L. Withers, B.H. Nguyen, K. Elliott, Q. Ren and Z. Chen, Displacive disorder and dielectric relaxation in the stoichiometric bismuth-containing pyrochlores, $Bi_2M^{III}NbO_7$ (M = In and Sc), *J. Solid State Chem.* **182**(10), p. 2748-2755 (2009).

Provisional Patent: Y. Liu, R.L. Withers, B.H. Nguyen, K.J.C. Elliot, *Bi-based pyrochlore ceramics*. Australian Provisional Patent Application Number 2007903107.